



פלנטות במערכת השמש- אטמוספרות וקשרי גומלין עם שאר מערכות הפלנטה



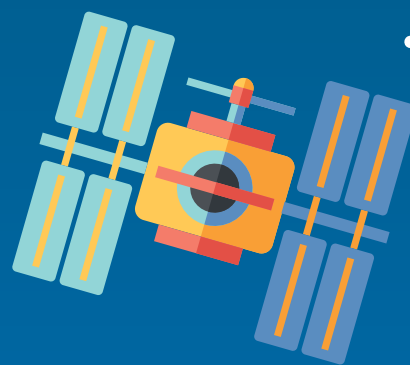
האטמוספירה של כדור הארץ מהחלל

היכרות עם האוויין ונוס וניתוח תצלומיו



.....
גיל התלמידים: חט"ב
מספר תלמידים מומלץ: עד 25
משך השיעור: 90 דקות
כותבות המסר: ד"ר שמרית ממון וד"ר סיון איזיקסון
מהמעבדה לחישה מרחוק והדמאה פלנטרית
באוניברסיטת בן גוריון בנגב.

.....
יש להדפיס את דפי העבודה והתמונות המצורפות בצבע
ובאיכות גבוהה ככל האפשר. לחלופין מומלץ לקיים את
השיעור בכיתת מחשבים. בדפי העבודה יש שאלות בונוס
המצריכות שימוש בתוכנה החינמית Google earth.
מומלץ מאוד להתקינה.



רציונל אחר

- שיעור זה עוסק בתרומתו הייחודית של הלוויין ונוס ובתכונותיו של לוויין זה ותכונותיהם של לווייני חישה מרחוק בכלל.

מטרות (ידע ואיומנויות)

- התלמידים יכירו ויבינו את המושג החישה מרחוק ואת חקר כדה"א באמצעות הדמאות לוויין.
- התלמידים ילמדו על עקרונות בסיסיים במחקר סביבתי בניתוח הדמאות לוויין (ארבע הרזולוציות).
- התלמידים יכירו את תכונותיו ויתרונותיו של הלוויין ונוס.
- התלמידים יתנסו בניתוח הדמאות שהתקבלו מהלוויין ונוס, בחילוץ מידע ובהשוואה ללוויינים אחרים.

מושגים עיקריים

- חישה מרחוק, רזולוציה, רזולוציה מרחבית, רזולוציה רדיומטרית, רזולוציה ספקטראלית, רזולוציה עיתית, ניטור שינויים בזמן, מולטי-ספקטראליות, צילום אינפרא-אדום

מקורות מידע ותוכנות

- מידע על הלוויין ונוס באתר [סוכנות החלל הישראלית](#)
- Google Earth (מומלץ)





רקע אורה וחופים

חישה מרחוק

חקר כדה"א מהחלל הוא תחום טכנולוגי-גאוגרפי שהחל להתפתח לפני כחמישים שנה עם שליחת לווייני הריגול הראשונים (לווייני תצפית, חישה מרחוק). כיום קיימים עשרות לווייני צילום, הן מחקריות והן מסחריות, ולכל לוויין תכונות משלו, בהתאם למשימה שלשמה שוגר. כבר שנים רבות יש למדינת ישראל נציגות מכובדת של לווייני תקשורת ולווייני חישה מרחוק בחלל. **בשנת 2017 בלטה בהישגיה הלוויינות הישראלית בתחום החישה מרחוק**. בשנה זו שוגרו בהצלחה שני לווייני תצפית ישראליים. הראשון - ננרלוויין BGUSAT, לוויין של אוניברסיטת בן-גוריון בנגב בשיתוף עם התעשייה האווירית וסוכנות החלל הישראלית. השני - הלוויין ונוס VENμS, פרי שיתוף פעולה של סוכנות החלל הישראלית וזו הצרפתית. הלוויינים הללו עדיין שוהים בחלל, מצלמים אתרים נבחרים על פני כדה"א ומשדרים את התמונות אל תחנות הקרקע.

הראאות לוויין

לתיאור צילומי לוויין אנו משתמשים במונח הדמאה (Image), ולא הדמיה (Simulation).

הלוויין ונוס

ונוס, ששמו נכתב בלועזית VENμS (ראשי תיבות של Vegetation and Environment on a New Micro Satellite), הוא לוויין חישה מרחוק שנבנה ומופעל בשיתוף פעולה של סוכנות החלל הישראלית והצרפתית. הלוויין שוגר באוגוסט 2017 והדמאות שלו כבר משמשות חוקרים ברחבי העולם במגוון נושאי סביבה וחקלאות.

כאן בלינק אפשר לעקוב ולראות היכן נמצא הלוויין ונוס בכל רגע.

רכולציה

משמעות המילה רזולוציה היא כושר הפרדה או כושר הבחנה. בהקשר של הדמאות לוויין ושל תמונות בכלל, המושג רזולוציה מציין את היכולת שלנו להפריד ולהבחין בין עצמים בתמונה. יכולת זו תלויה במאפיינים שונים של התמונה, וכל מאפיין הוא כשלעצמו סוג של רזולוציה, כפי שיפורט להלן.

רכולציה מרחבית

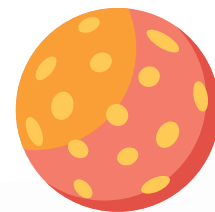
רזולוציה מרחבית עניינה **גודלו של העצם** הקטן ביותר שניתן לזהות בתמונה. היא מתבטאת בגודל הפיקסל בתמונה - כמה שטח במציאות מייצג כל פיקסל. גודל הפיקסל תלוי ביכולות החישה (סנסור) ובמרחק שלו מהאובייקט המצולם. בצילומים של אובייקטים על פני הקרקע במצלמה רגילה, ייתכן גודל פיקסל של 1 מ"מ עד 1 ס"מ. בהדמאות לוויין גודל הפיקסל יהיה לרוב בין מטרים אחדים לאלף מטרים.

הרזולוציה המרחבית של ונוס: גודל הפיקסל של ונוס הוא ~5 מטר לפיקסל. זוהי רזולוציה מרחבית הנחשבת גבוהה לחישה לוויינית (HSR - High Spatial Resolution). לשם ההשוואה, לווייני מזג אוויר מצלמים ברזולוציה של כ-1,000 מטר לפיקסל, ולעומת זאת יש היום לוויינים המצלמים ברזולוציה של 1 מטר לפיקסל ואף פחות, ונחשבים בעלי רזולוציה מרחבית גבוהה מאוד (VHSR - Very High Spatial Resolution). בעתיד מתוכנן הלוויין ונוס לשנות מסלול קרוב יותר אל כדה"א ולשפר את הרזולוציה המרחבית שלו: להגיע ל-2.7 מטר לפיקסל.

רכולציה רדיומטרית

רזולוציה רדיומטרית עניינה **כמות הגוונים** שכל פיקסל יכול לייצג (מספר גוני אפור). ככל שמתועדים בתמונה יותר גוונים, כך גדלה יכולת ההבחנה בין אובייקטים שהגוונים שלהם כמעט זהים. הרזולוציה הרדיומטרית מבוטאת בשיטה הבינארית לביטוי מספרים ועל כן נמדדת בביט, וכמות הגוונים מחושבות בחזקות על בסיס 2.

הרזולוציה הרדיומטרית של ונוס: הרזולוציה הרדיומטרית של הלוויין ונוס היא 10 ביט, כלומר 1024 גוני צבע אפשריים בכל אחד מהערוצים.

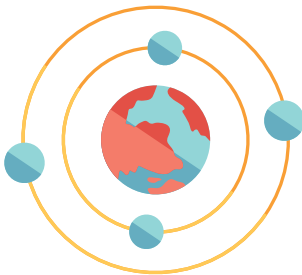




צילום מולטי-ספקטראלי (רב-ערוצי)

מצלמות רגילות מצלמות בתחום הנראה לעין בשלושה ערוצים: כחול, ירוק ואדום. התמונה המתקבלת ממצלמות צבעוניות היא השילוב של הצבעים הללו בעוצמות שונות של בהירות. מצלמות מולטי-ספקטראליות המשמשות במחקר יכולות לצלם בתחומים נוספים של הספקטרום האלקטרומגנטי. למעשה הן "רואות" קרינה במגוון אורכי גל. מצלמות מולטי-ספקטראליות מותקנות על לוויינים רבים ועל מטוסים ורחפנים. תמונות הלוויין ותצלומי האוויר משמשים לשלל מטרות: מחקרים אקולוגיים, מיפוי גאולוגי, שימושים חקלאיים ועוד.

רכולציה ספקטראלית



רזולוציה ספקטראלית היא מידת יכולתו של החיישן להבחין בין אורכי הגל השונים, הן בתחום הנראה והן בתחומים נוספים כמו אולטרה-סגול, אינפרא-אדום, תרמי וכד'. ככל שהתמונה כוללת יותר תחומים בספקטרום האלקטרומגנטי וככל שיכולת ההבחנה בין אורכי הגל גדלה, כך מתקבל יותר מידע על האובייקטים המצולמים בהדמאה.

רזולוציה ספקטראלית של ונוס: המצלמה המותקנת על הלוויין מורכבת מ-12 ערוצים בתחום האור הנראה והאינפרא-אדום הקרוב. ריבוי הערוצים בתחום זה (ערוצים יחסית צרים) ותכונותיהם מקנים ללוויין רזולוציה ספקטראלית גבוהה בתחום הרגיש לניטור ומחקר צומח.

צילום באינפרא-אדום קרוב של מחקר חקאי ואקולוגי

שילוב התחום הנראה והאינפרא-אדום בהדמאות לוויין מספק מידע חשוב על מצב הצמח והקרקע. בעזרת עיבוד התמונות ניתן לאתר מחלות או יובש בצמחים (עקת יובש), להעריך את טיב היבול בשלב מוקדם ובכך לסייע בתכנון יעיל וניהול נכון של השדות החקלאיים.

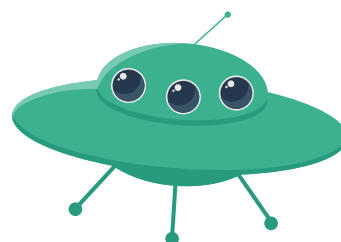
רכולציה עיתית

רזולוציה עיתית בלוויין עניינה הזמן שחלף בין תיעוד אחד של נקודה על פני כדה"א למשנהו. התיעוד של כדה"א לאורך זמן בצילומי לוויין מאפשר השוואה של תופעות בקנה מידה נרחב.

רזולוציה עיתית של ונוס: זמן החזרה של ונוס הוא יומיים בלבד. זהו זמן חזרה הנחשב גבוה והוא מאפשר מעקב אחר שינויים מהירים למדי, כמו תגובה לשרפות, פגעים בחקלאות, תגובת צמחים לזיהום ממוקד ועוד. לצורך השוואה, זמן החזרה של לוויני התצפית האמריקאים מסדרת LANDSAT, סדרה גדולה ומוצלחת, הוא 16-18 יום! בטווח זמן זה אנו עשויים להחמיץ אירועים קריטיים כמו שרפות או שיטפונות בזק, ואין אפשרות לעקוב כראוי אחר גידולים חקלאיים מהירי צימוח כגון תירס.

סיכום נושא רכולציות הרמאות הלוויין ונוס:

אף על פי שיש כיום לוויינים בעלי רזולוציה מרחבית, רדיומטרית, ספקטראלית או עיתית גבוהה מזו של הלוויין ונוס, יש לבחון כל לוויין על פי מכלול הרזולוציות שלו. לרוב רזולוציה אחת באה על חשבון אחרת. ונוס נחשב לוויין ייחודי ומוביל ביכולות המחקר שהוא מאפשר, בשל שילוב כלל התכונות שלו ובעיקר בזכות ריבוי ערוצים יחסי בתחום האור הנראה והאינפרא-אדום הקרוב ובזכות תדירות הצילום הגבוהה. ריבוי הערוצים מספק מידע רב על מצב הצמחייה והקרקע, ותדירות הצילום הגבוהה מאפשרת ניטור של שינויים מהירים בסביבת המחקר.



מהלך השיעור

תקציר השיעור:

מבוא המסביר על לוויינים וחישה מרחוק בכלל ועל הלוויין ונוס בפרט > פרק מבוא: מהי רזולוציה > פרק על רזולוציה מרחבית > פרק על רזולוציה רדיומטרית > פרק על רזולוציה ספקטראלית > פרק על רזולוציה עיתית. עבור כל אחד מן הפרקים על הרזולוציות מצורף דף עבודה לתלמידים בליווי הדמאות לוויין. מומלץ לפנות לדף העבודה בתום כל פרק במצגת, אך ניתן גם לרכז את דפי העבודה לסיום המצגת כולה.

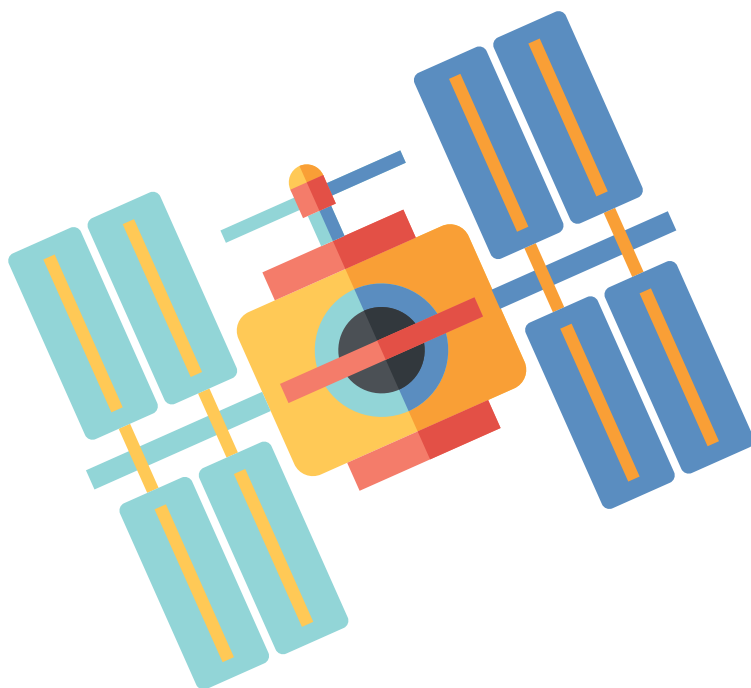
רצף מומלץ לשיעור

הנושא	מס' שקופית	הנחיות למורה
שימו לב: בחלק מהשקופיות יש הערות הבהרה ודגשים למורה בתוך המצגת.		
מבוא	9-2	<ul style="list-style-type: none"> שקפים אלה נועדו ליצור עניין בתלמידים ולהציג להם את נושא הלוויינות והחישה מרחוק בהקשר של הלוויין הישראלי-צרפתי החדש, ונוס. כדאי להתעכב ולהגדיר על הלוח, עם התלמידים, מהי חישה מרחוק. *בחי היום-יום אנו כבר רגילים לראות על מסך הטלוויזיה שלנו ובאתרי אינטרנט את השימוש הרחב בהדמאות לוויין. בפעם הבאה שתצפו בחדשות, למשל, שימו לב שהמפות המוצגות הן למעשה הדמאות לוויין.
מהי רזולוציה	16-10	<ul style="list-style-type: none"> הסבר על רזולוציה, מושג שהתלמידים ודאי שמעו בעבר אך יתקשו להגדיר. נסו לתת לתלמידים להגדיר את המושג בעצמם בתחילה, או לומר מה הם יודעים עליו, באיזה הקשר שמעו את המושג וכו'.
רזולוציה מרחבית	24-17	<ul style="list-style-type: none"> הסבר והדגמה על רזולוציה מרחבית. שימת דגש על כך שרזולוציות שונות מתאימות למשימות מחקר שונות. אם מתפתח דיון ניתן לציין גם את החסרונות של רזולוציות גבוהות, לדוגמה גודל הקובץ. ככל שיש יותר פיקסלים בתמונה נתונה, כל פיקסל מייצג שטח קטן יותר במציאות. זוהי רזולוציה מרחבית גבוהה יותר, ופירושו של דבר קובץ כבד יותר (והדבר נכון לעוד סוגי רזולוציות). למשימות רבות יש צורך ברזולוציה מרחבית גבוהה, למשל למחקרים העוסקים באוכלוסייה ובמבנים בשטח עירוני, או למשימות ריגול וליישומים צבאיים.
רזולוציה רדיומטרית	26-25	<ul style="list-style-type: none"> פרק קצר על רזולוציה רדיומטרית. גם דוגמת החתול בתחילת המצגת היא רזולוציה רדיומטרית. לפרק זה אין תרגיל התנסות. מטרת הפרק להמחיש שוב שכל פיקסל בתמונה מקבל ערך, כלומר צבע, וכך נבנית התמונה.





הנושא	מס' שקופית	הנחיות למורה
רזולוציה ספקטראלית	39-27	<ul style="list-style-type: none"> חשובה לפרק זה ההבנה שתמונה דיגיטלית (ממצלמת סמארטפון או ממצלמה לוויינית) היא למעשה שילוב של שלוש תמונות בצבעים שונים. נדרש הסבר קצר על הספקטרום האלקטרומגנטי ועל הקרינה באורכי גל שונים. כאשר אנו מסתכלים "מעבר לחושינו", כלומר מעבר לתחום הנראה, אנו מקבלים מידע חדש על שטח המחקר. למשל, אם נסתכל על אצטדיון בתחום הנראה בלבד, לא נוכל לדעת אם הדשא אמיתי או סינתטי: לשניהם צבע ירוק. אולם אם נצלם את האצטדיון בתחום האינפרא-אדום הקרוב, ההבדל יהיה מובהק. * כדי שנוכל לראות מעבר לחושינו (מעבר לתחום הנראה בעין האנושית) אנו משתמשים בחיישנים מיוחדים כגון מצלמות תרמיות ומצלמות חישה מרחוק המותקנות על לוויינים. יש בעלי חיים המסוגלים לראות בתחומים אלו ללא חיישנים. דבורים, למשל, רואות בתחום האולטרה-סגול וכמה מסוגי הנחשים רואים בתחום האינפרא-אדום, כלומר ראייה תרמית.
רזולוציה עיתית	43-40	<ul style="list-style-type: none"> התמקדות באחת התכונות החשובות של הלוויין - זמן חזרה. כדאי להגדיר עם התלמידים מהו זמן חזרה, ולדון בחשיבותו של זמן חזרה קצר כמו של ונוס (יומיים) ובסוגיות מחקר סביבתיות שהלוויין יאפשר לחקור (דוגמאות בהערות לשקופיות במצגת). * זמן חזרה, כפי שהוזכר לעיל, הוא קריטי בחקר תופעות פתאומיות כגון אסונות טבע (הוריקנים, התפרצות הרי געש, שיטפונות וכד'). בחקר תהליכים הדרגתיים יותר, זמן חזרה קצר משפר את מידת הדיוק ואת איכותם של הנתונים המתקבלים (לדוגמה, השפעת התפשטות מחלה בשדה חקלאי).
סיכום	44	<ul style="list-style-type: none"> תרומתו האפשרית של הלוויין ונוס למחקר סביבתי. לאחר שהתלמידים הבינו את יכולות הלוויין יתקיים דיון ובו הם יתבקשו להעלות רעיונות: מה יאפשר הלוויין לחקור ולמצוא ובאילו תחומים.





הפעילות אחרית

רזולוציה מרחבית

מטרת המטלה היא להמחיש לתלמידים את המשמעות של גודל הפיקסל הנחוץ לזיהוי העצמים בתמונה.

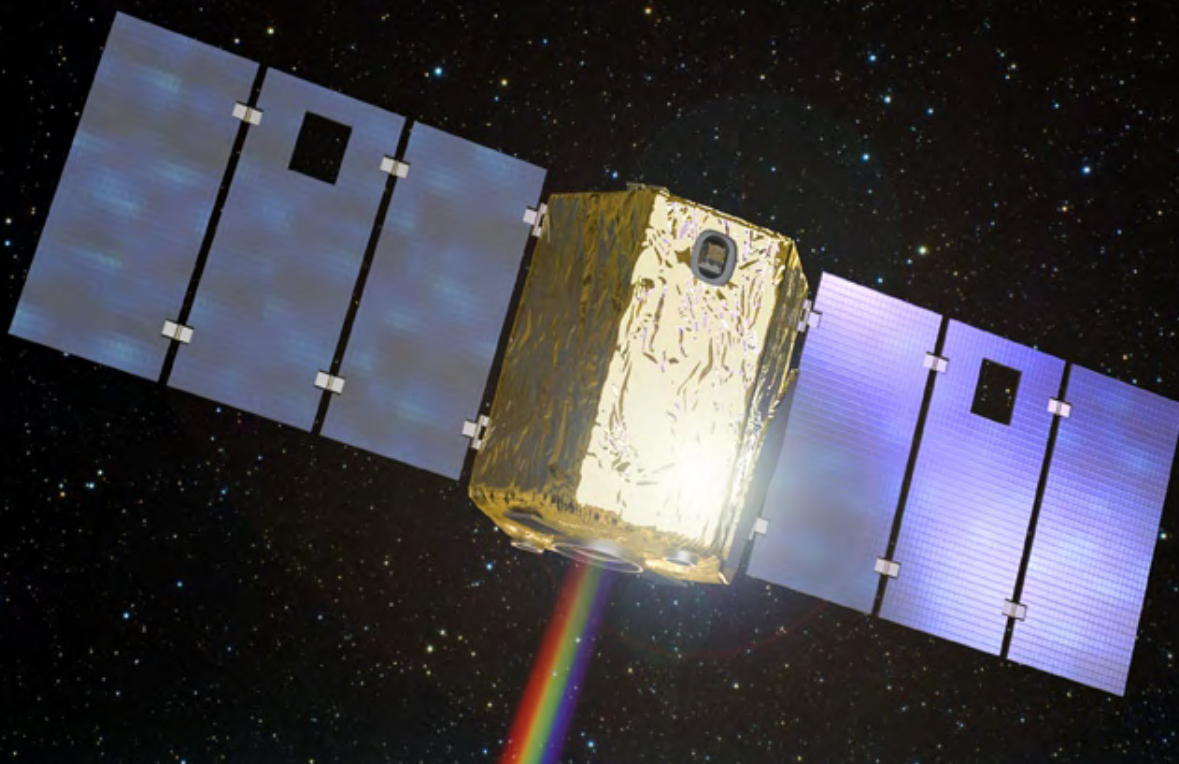
1. פרטים שלא ניתן להבחין בהם ברזולוציה של 30 מטר: שבילים קטנים, מבנים, שדות קטנים, פרטים בקו החוף וכד'. הנחו את התלמידים למצוא פרטים רבים ככל האפשר ולסמנם על ההדמאה המודפסת, או הקרינו על לוח מחיק וסמנו עם התלמידים את הפרטים.
2. מובן שיש אינסוף פריטים שאיננו יכולים לראות ברזולוציה של 5 מטרים: מכוניות, אנשים, עצים וכד'.
3. שאלת בונוס: יש לשים לב להבדל בין הדמאות לווין של Google earth לבין תצוגת רחוב (Street view) הרזולוציה המרחבית בתצוגת הרחוב היא אומנם גבוהה מאוד וניתן לראות פרטים שאי אפשר לראות מהלווין, אבל החיסרון של תצוגת הרחוב הוא הרזולוציה העיתית והכיסוי המרחבי. תצוגת רחוב מצולמת אחת לכמה שנים ולכן אינה עדכנית.

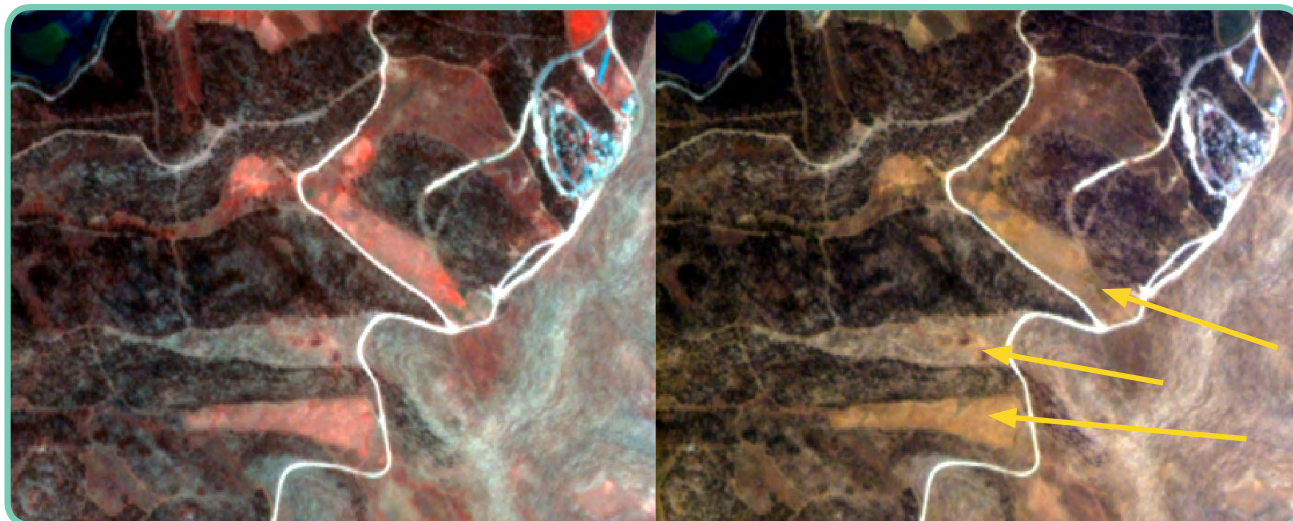
רזולוציה ספקטראלית

מטרת המטלה היא להמחיש לתלמידים ששימוש בתחום שמעבר לאור הנראה (מעבר לחושני), מאפשר קבלת מידע חדש.

1. מה רואים כאשר בוחנים את יער יתיר באור אינפרא-אדום קרוב (מיוצג בהדמאה בצבע אדום):

- **השדות החקלאיים** בולטים לעין לעומת היער, בשל צפיפות הצומח בשדות החקלאיים (ניתן לראות ב-Google earth שהיער דליל מאוד ולכן כל פיקסל ביער מכיל גם צמחייה אך גם הרבה קרקע).
- **ערוצי הנחלים** בסביבה המדברית מסביב ליער, שבתמונת הצבע הרגיל לא ברור אם יש בהם צמחייה, נראים אדומים בתמונת האינפרא-אדום הקרוב, ודבר זה מלמד על נוכחות צמחייה.
- 2. דוגמה לאזורים שנראים דומים זה לזה בתמונת האור הנראה: שימו לב לשלושת הוואדיות ממזרח ליער (בצורת משולשים; מסומנים בחיצים צהובים בתמונה מימין). הגוון שלהם נראה דומה, אך כשבוחנים את השטח באור באינפרא-אדום קרוב הוואדי האמצעי נראה אדום פחות. מתברר אפוא שיש בו פחות צמחייה.





איור 1: מימין הדמאה של יער יתיר באור הנראה. משמאל אותו אזור בצילום אינפרא-אדום קרוב (צבוע באדום).

רזולוציה עיתית

מטרת המטלה היא להמחיש לתלמידים את השינויים הרבים המתרחשים באזור חקלאי ואת ניטורם באמצעות הלוויין.

1. אסונות טבע וכן גידולים חקלאיים הם דברים שחל בהם שינוי בטווח זמן של יומיים, ולכן הלוויין ונוס רלוונטי מאוד למחקרים שעוסקים בהם. לעומתם, בתהליכים ארוכי טווח הקשורים באקלים העולמי, כמו התחממות גלובלית, המסת קרחונים, מדבור, הם תהליכים שאי אפשר להבחין בשינוי בהם בטווח של יומיים.

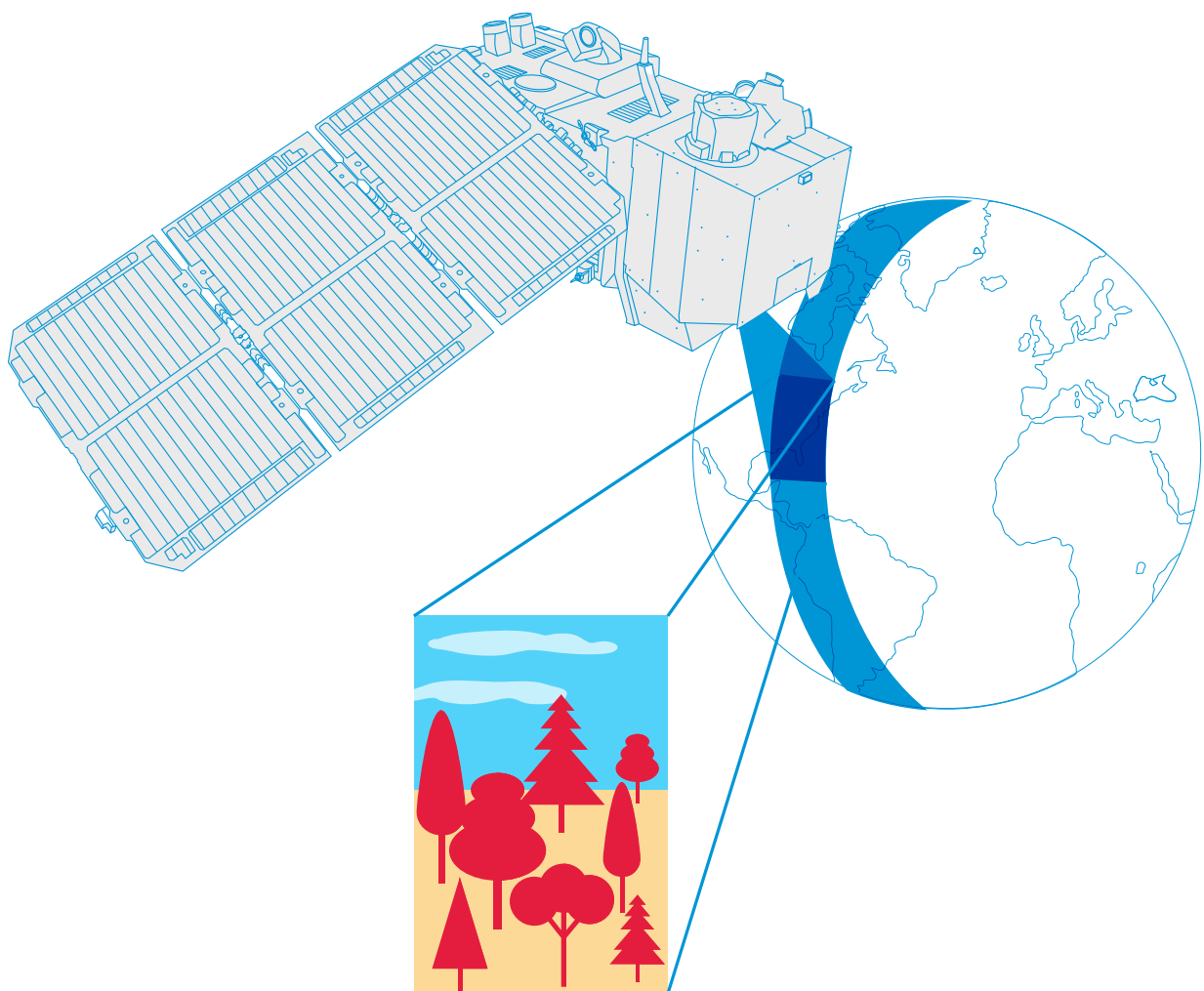
2. השינויים שקל להבחין בהם יהיו בשטחים החקלאיים. אזורים שלא השתנו הם לרוב האזורים הטבעיים, כמו הר תבור עצמו, וכן האזורים הבנויים.

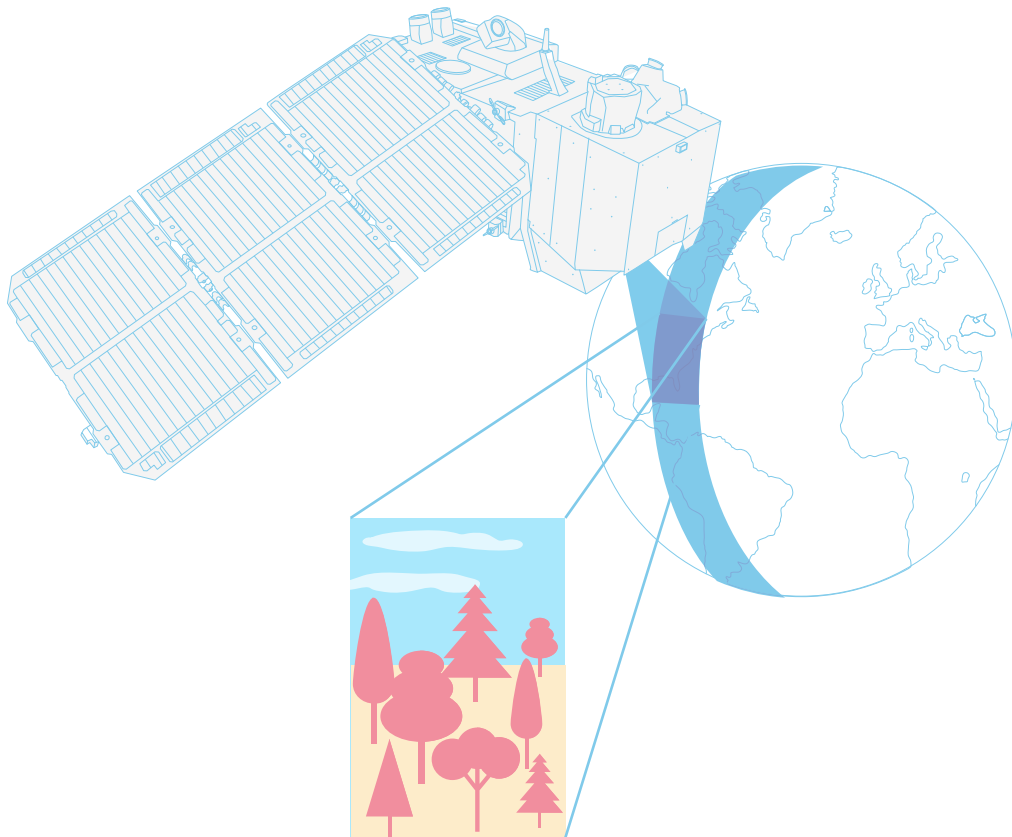


teach with space

→ INFRARED WEBCAM HACK

Using infrared light to observe the world in a new way





Teacher guide

Fast facts	page 3
Summary of activities	page 4
Introduction	page 5
Background	page 6
Activity 1: Hacking the webcam	page 8
Activity 2: Looking at objects in infrared light	page 9
Activity 3: Looking at the Earth in infrared light	page 11

Student worksheets	page 13
--------------------	---------

Links	page 20
-------	---------

teach with space – infrared webcam hack | P15a
www.esa.int/education

The ESA Education Office welcomes feedback and comments
teachers@esa.int

Activity concept developed for ESA by the National Space Academy (NSA), UK

An ESA Education production
Copyright 2018 © European Space Agency

→ INFRARED WEBCAM HACK

Using infrared light to observe the world in a new way

Fast facts

Subject: Physics, Geography

Age range: 12-16 years old

Complexity: medium

Lesson time required: 30 minutes per activity

Cost: medium (10-30 euros per group)

Location: any indoor space with daylight

Includes the use of: webcam and computer

Keywords: Earth observation, Infrared light, Satellite imagery, Physics, Geography.

Brief description

This set of three activities will enable students to understand the electromagnetic spectrum and observe infrared radiation through the modification of a cheap webcam. It will enable discussion of how infrared radiation can be used to obtain information that is not available using visible light. Students will also analyse satellite images providing them with a context to understand why it is useful to “see” in infrared.

Learning objectives

- Identify the different types of electromagnetic radiation.
- Describe different applications of infrared light.
- Use tools available on the internet to collect and analyse satellite data.
- Understand how infrared light can be used to monitor the health of vegetation.
- Identify false colour and true colour satellite images.

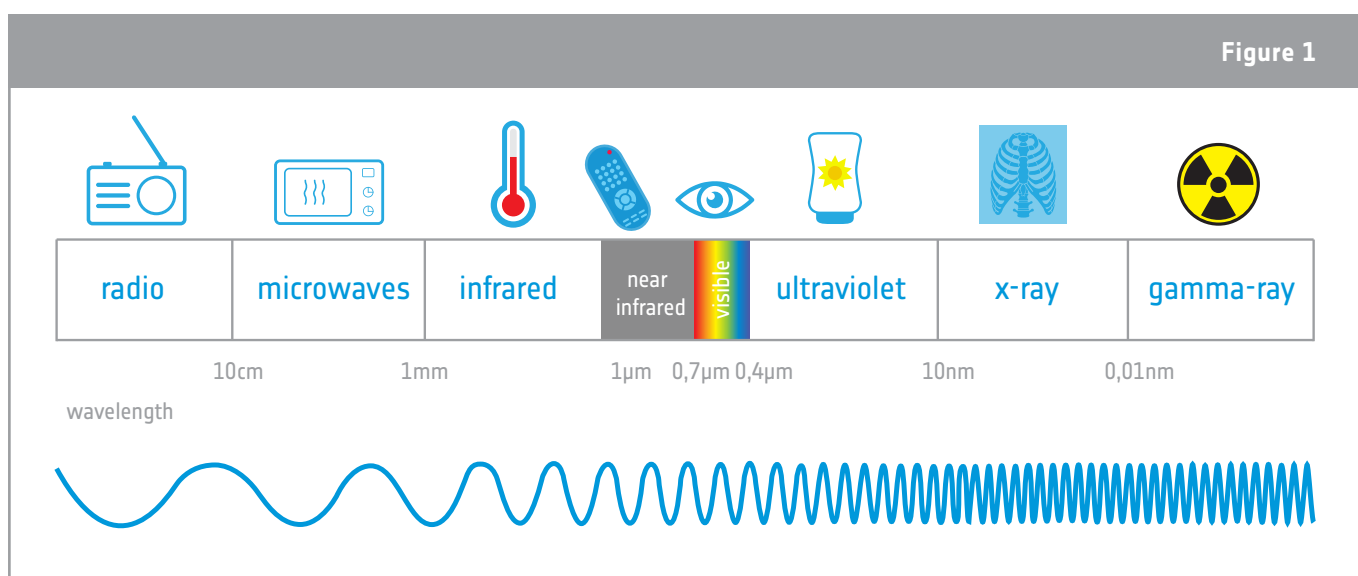
→ Summary of activities

Summary of activities					
	Title	Description	Outcome	Requirements	Time
1	Hacking the webcam	To modify a webcam so that it sees in near-infrared light rather than in visible light.	An Infrared webcam	None	30 minutes
2	Looking at objects with an infrared camera	To look at different types of objects, observing each in both visible and near-infrared light.	To identify different applications of infrared light and understand how infrared light can be used to find out information that is not available using visible light.	Completion of Activity 1	30 minutes
3	Looking at the Earth in infrared light	To analyse true colour satellite images and compare them to false colour images that visualise near-infrared light.	To understand how infrared light can be used to monitor the health of vegetation and why it is useful to “see” in infrared.	None	30 minutes

→ Introduction

The electromagnetic spectrum categorises the electromagnetic radiation that exists, including infrared radiation (Figure 1). Most electromagnetic radiation emitted by the Sun is reflected or absorbed by Earth's atmosphere. However, some radiation like visible radiation, radio waves, and part of infrared can pass through the atmosphere.

Objects with different surface features reflect and absorb the Sun's radiation in different ways. The reflected radiation contains information about the surface of the object, and enables us to see the colour and form of the object. The human eye can only see a very limited range of the spectrum, the visible light. However we can use different instruments to see what is invisible to us. Earth observation satellites, for example, carry scientific instruments that can see in the visible and the infrared range, as well as other ranges of the electromagnetic spectrum.



↑ The electromagnetic spectrum categorises different types of radiation, from the longest (radio) to the shortest (gamma ray) wavelengths.

In this resource, we will focus on the near-infrared and visible parts of the spectrum. Infrared radiation is divided into different parts, just like visible light is divided into different colours. Near-infrared radiation, with its slightly longer wavelengths than visible light, is reflected by vegetation, delivering detailed information about plants on Earth. That is why this part of the electromagnetic spectrum is used in Earth observation satellites to monitor Earth's vegetation.



↑ The European Sentinel-2 satellite carries an high-resolution multispectral imager with 13 spectral bands for a new perspective of our land and vegetation.

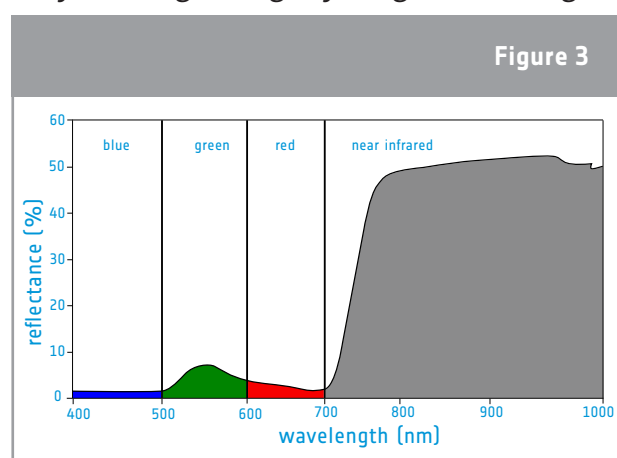
→ Background

Vegetation monitoring

Plants have a particular way of reflecting electromagnetic radiation. The chlorophyll in the plants absorbs light to get energy for the photosynthesis process. But only the red and blue part of the visible light are needed. The green light is reflected, which explains why leaves appear green to us. The near-infrared light is not needed for the photosynthesis, therefore most of the light is reflected by the cell structure of the leaf.

Figure 3 shows the percentage of reflected radiation, also called reflectance, for a healthy plant. The blue light is absorbed almost completely by the chlorophyll, about 10% of the green light is reflected, and the red light is absorbed almost completely. Moving to slightly longer wavelengths, about 50% of the near-infrared light is reflected. The combination of low visible reflectance and high near-infrared reflectance is a characteristic of most plant types.

When a plant becomes less healthy, for example due to water scarcity, it reflects more of the visible red light and less of the near-infrared light. This can also be seen in autumn when leaves turn yellow and red, due to phenology. The bigger the difference between the reflected red and near-infrared light, the healthier a plant is. This fact is used in Earth observation to calculate indices which help us obtain information about the health of plants on a large scale.



↑ Percentage of radiation reflected by a healthy plant for the wavelengths of visible light and near-infrared light.

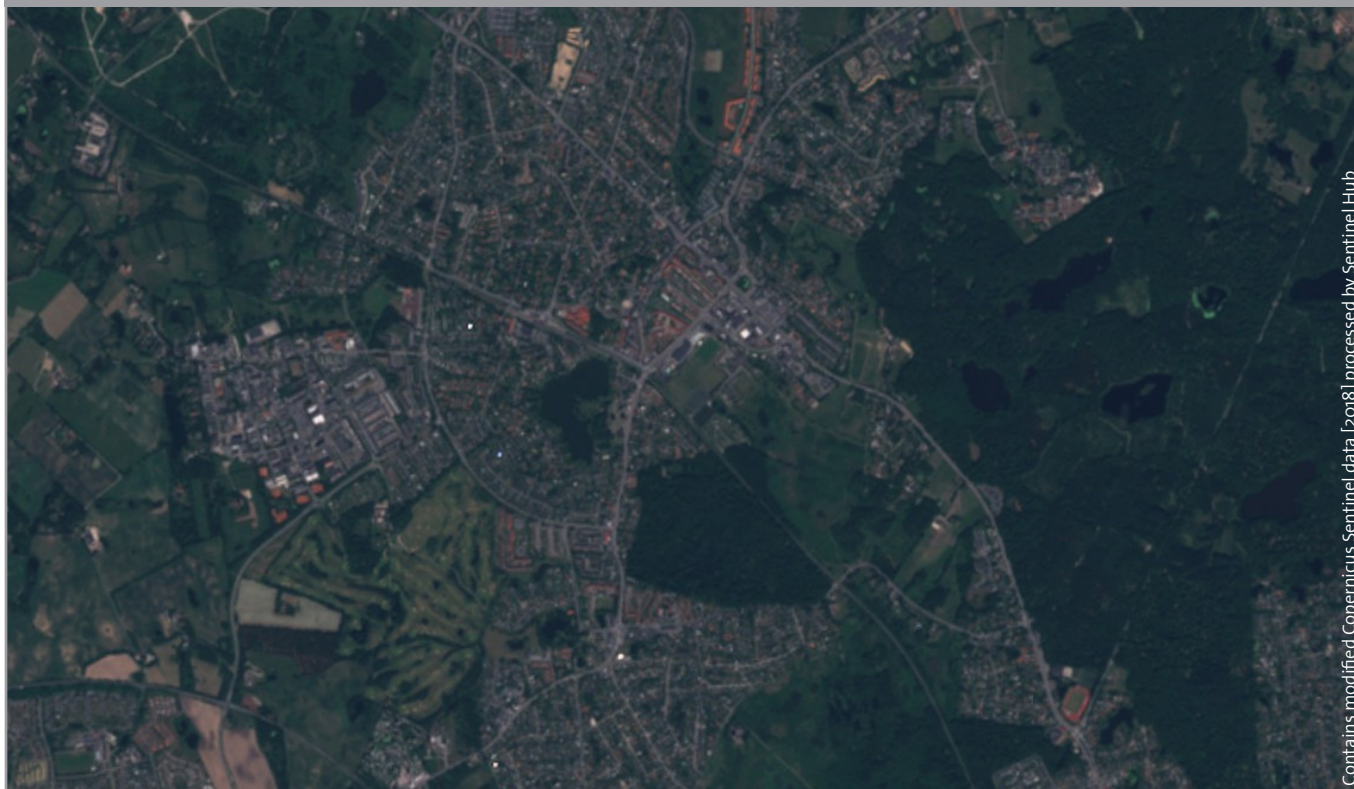
True colour and false colour images

A way to visualise reflected near-infrared light is to create false colour images, making use of the fact that cameras carried by satellites can 'see' more than just the visible part of light. A false colour image uses at least one wavelength outside the visible range, and as a result the colours in the final image may not be what we expect them to be. For example, grass is not always green! A true colour image combines actual measurements of reflected red, green, and blue light. The result looks like the world as we are used to seeing it.

In the figures below, we can see a true colour image (Figure 4) and a false colour image (Figure 5) of the town of Birkerød in Denmark. The false colour image shows reflected near-infrared light as red, red light as green, and green light as blue. Since plants reflect more near-infrared than green, vegetation areas will appear red. The brighter and richer red indicates a higher reflectance in the near-infrared, therefore indicating more and healthier vegetation. In the true colour image, the vegetation appears green, like we are used to seeing it.

Overall, the reflectance in the visible light is much lower than the one in the near-infrared, and the image is darker. This makes it harder to identify water bodies in the real colour image, because the reflectance is also very low. In the false colour image, the water bodies can be clearly identified due to the high difference in reflectance for water and the surrounding vegetation (high reflectance). Water absorbs most of the incoming light—near-infrared, red, and green—and therefore has a very low reflectance.

Figure 4



↑ True colour image of the town of Birkerød in Denmark.

Figure 5



↑ False colour image of the town of Birkerød in Denmark.

→ Activity 1 – Hacking the webcam

In this activity, students will modify a webcam so that it sees in near-infrared light rather than in visible light.

Equipment (for each infrared camera)

- 1 webcam with manual focus ring on the front
- 1 drawing pin or a similar pin
- Two pieces of exposed photographic film or a polarising filter large enough to cover the lens
- Clear tape
- Scissors
- Computer

Exercise

Instructions for hacking the webcam are provided in the student activity sheet. Cheap webcams are usually easier to disassemble than more expensive models. The example used in the student activity sheet is a Trust 17405. Refer to the Infrared Webcam Hack video for a video guide of how to set up and carry out the experiment. Students can work in small groups. Alternatively, the webcams can be modified in advance, and students can run Activities 2 and 3. The principal modification to be performed is to remove the infrared filter. Depending on the conditions of light it may be necessary to add a visible light filter.

Filters work by blocking light within a specific wavelength range. Two polarised filters are required to block visible light. This is because the wave may be moving up and down, or side to side (this single-plane oscillation is called polarisation). Two filters ensure that all the visible radiation is blocked.

Most webcams are “plug and play” – the software required to run them is already on the camera. However, depending on the webcam you use, there is a small chance that it may be necessary to install the operating software before the webcam is plugged into a computer.

Teachers should make sure that students understand that the hacked camera is a near-infrared camera, not a thermal imaging camera!

The sensors used in digital cameras are sensitive to light with wavelengths up to around $1\ \mu\text{m}$ (near-infrared). Thermal imaging cameras use infrared at longer wavelengths. These cameras are sensitive to the infrared radiation which is emitted by all objects with a temperature above absolute zero and not visible to our eyes. The higher the temperature of an object, the shorter the wavelength of the emitted radiation will be. When the temperature of an object is high enough, the radiation emitted can be imaged using near-infrared cameras or our very own eyes. We can see this in our kitchen: when a toaster reaches very high temperatures, it turns red!



↑ Infrared webcam hack video. See links section.

→ Activity 2: Looking at objects with an infrared camera

In this activity, students will look at different types of objects, observing each in both visible with their eyes and near-infrared light with the modify webcam.

Equipment

- Infrared camera (from activity 1)
- Remote control
- Led light
- Candle
- Healthy plant and fake plastic plant

Exercise

Daylight is necessary for the experiment with the plants. The experiment should always be tested in the classroom before doing it with the students. Depending on the light conditions in the room it may be necessary to block the visible light and to put the polarising filter/exposed film in front of the lens.

Students should observe the different objects and fill the table in the student activity sheet, where they describe how they see each object in both types of light, and then give an interpretation for their observations.



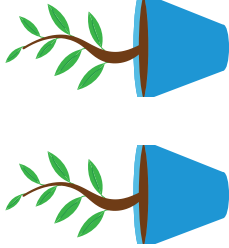
Results

See the table on the next page.

Discussion

The remote control, the candle and the LED light send out (emit) infrared radiation. With the help of the hacked webcam, students can 'see' infrared light, e.g. emitted from the remote control. Looking at light sources from daily life, like the LED light and the candle, the infrared camera allows us to investigate which one emits less infrared light and is therefore more energy-efficient.

Looking at the plants with the hacked webcam, what we see is reflected daylight. As the real plant reflects a lot of near infrared light and this is related to a healthy plant structure, we can understand how healthy a plant is when looking at it in infrared light.

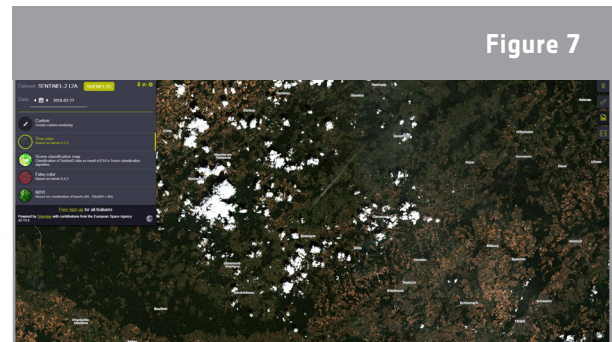
Objects	Describe your observations		Explain your observations
	Visible light	Infrared light	
Remote control 	<p>When pressing a button and looking at the infrared sender, nothing can be seen, (except sometimes a faint light when the wavelength used by the remote control is very close to the visible wavelengths).</p>	<p>Looking at the remote control through the webcam and pressing the buttons, a bright light signal from the infrared sender can be seen.</p> <p>Tip: This is also visible with the camera of some smartphones!</p>	<p>Remote controls are used to control from a distance some devices like televisions. How does the receiver (e.g. the television) know which button on the remote control has been pressed? Each button sends out on-off signals at a certain wavelengths of the infrared light. The pattern of the signal is related to one button on the remote. For this reason, we can see the signal emitted by the remote with the infrared camera.</p>
LED vs. candle 	<p>The LED light and the candle both emit light. The colours look different. The candle has a warmer light, whereas the LED light is whiter.</p>	<p>Looking through the webcam, the candle appears much brighter than the LED light.</p>	<p>The candle not only emits visible light but also heat which can be visible in the infrared, and for this reason the candle appears brighter with the infrared camera. The LED light does not emit a lot of light in the infrared like the candle, but it appears brighter in the visible.</p>
Living vs. fake plants 	<p>Both plants are green when looking at them.</p> <p>Tip: If there are any yellow or brown leaves, they can be compared to the healthy, green leaves.</p>	<p>Looking at both plants with the infrared webcam, the green leaves of the living plant appear much brighter than those of the fake plant.</p> <p>Yellow or brown leaves are much darker than the green leaves.</p>	<p>In visible light both plants look green and real. In the infrared camera the living plant looks much brighter than the fake one. The living plant reflects a lot of radiation in the infrared, as this part of the light is not needed for photosynthesis. High reflectance of infrared light is caused by the spongy mesophyll. This can be related to a healthy plant structure.</p> <p>The plant structure of the yellow or brown leaves is already destroyed, so the reflectance of the infrared light is much lower.</p>

→ Activity 3: Looking at the Earth in infrared light

In this activity students will analyse satellite images. The activity introduces true colour images and compares them to false colour images that visualise near-infrared radiation. It provides students with a context so that they understand why it is useful to “see” in near-infrared.

Exercise

The satellite images were downloaded from the EO Browser, an online application where you can access ready-to-use satellite images in true colour, false colour showing near-infrared, and many more products! You can explore this tool and start by showing the students their hometown in the summer and the winter with true and false colour images. Students can also research their own examples.



↑ Screenshot of the EO Browser online tool (08.08.2018).

1. **Observe the true colour image below taken by the Sentinel-2 satellite (Northern Germany, 28.11.2016). Which of the following features can you identify?**
 - ☐ Agriculture fields
 - ☐ Snow
 - ☐ Forest
 - ☐ Clouds
 - ☐ River
 - ☐ Lakes
 - ☐ Streets
 - ☐ Cars
 - ☐ Buildings
 - ☐ People

Teachers can ask students why there are no cars or people visible in the image. The reason is the spatial resolution of the satellite image. The spatial resolution is the area on Earth that is represented by one pixel of the satellite image. The satellite image in this exercise has a spatial resolution of 10m, therefore a pixel represents 10m x 10m on Earth. At this resolution, people and cars cannot be identified.

2. **Observe the false colour image.**
 - a. **Try to find the features you previously observed. Can you also identify new features?**

All features can be identified. Water bodies, especially the ones in the forest, can now be distinguished much more easily.

- b. **What surface type/feature appears red in the false colour image? Distinguish between bright red and dark red.**

Vegetation/plants appear red. The fields are bright red and the forest is dark red. The structure of the forest can be identified due to the shadow of the treetops.

3. Describe the differences and similarities between the true colour image in Exercise 1 and the false colour image in Exercise 2.

In the true colour image, the vegetation (grass and forest) appears in very dark green, and the bare soil in brown. Buildings and roads are grey. In the false colour images, the grass and forest appear in red.

Water bodies (lakes and rivers) are very dark in both images, and large buildings that could represent industrial areas are very bright/white in the true and false colour images.

4. Discuss the advantages and disadvantages of the true colour and false colour images showing near-infrared light.

Overall the reflectance displayed in the true colour image is much lower than the one in the false colour image, and the image is darker. This makes it harder to identify water bodies in the real colour image, because the reflectance is also very low. In the false colour image, the water bodies can be clearly identified due to the difference in reflectance values for water (very low reflectance) and the surrounding vegetation (high reflectance).

In the false colour images, more details of the vegetation can be identified. The reason is the high reflectance in combination with the shadows that occur due to the structure of the treetops. The angle of incidence of the Sun has to be taken into account when discussing shadows: the image was taken in November, meaning that the angle of incidence is lower than in the summer, therefore the shadows are bigger and rough surfaces appear darker.

→ General discussion

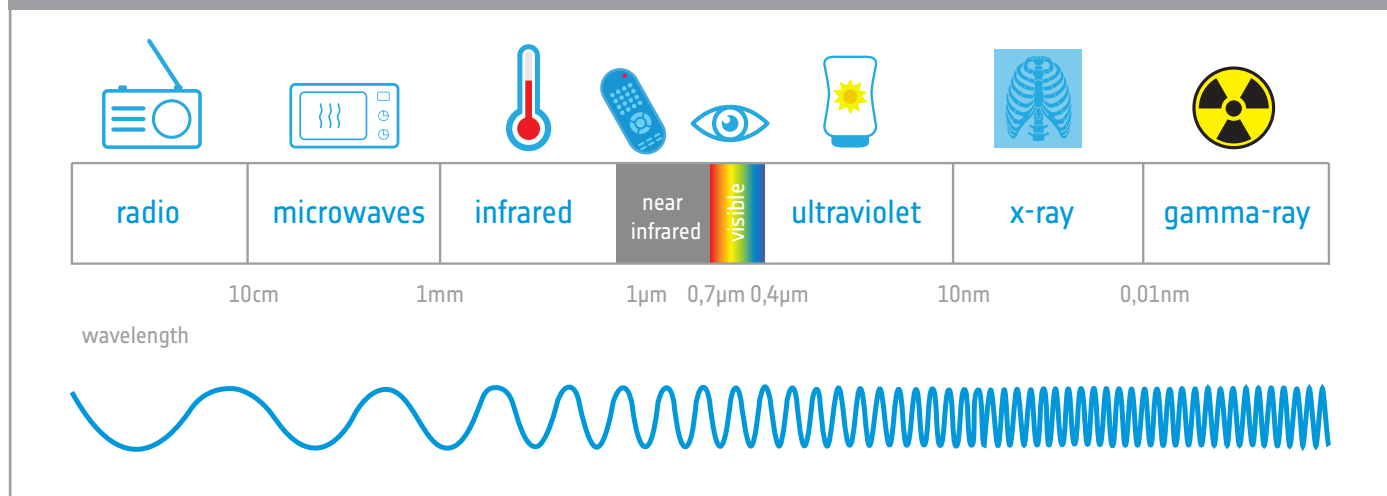
These practical activities can be used to discuss the electromagnetic spectrum, Earth observation applications, and the monitoring of vegetation on our planet. The activities also provide a setting for the discussion of the impact of space technology on our future and on our everyday lives.

→ INFRARED WEBCAM HACK

Using infrared light to observe the world in a new way

Our eyes can't see infrared light, but we can use an infrared camera to see this 'invisible' light. The light we can see – visible light – is only a very small part of the electromagnetic spectrum. Figure A1 shows the different types of radiation and their wavelengths on the electromagnetic spectrum and gives examples of what certain wavelengths are used for.

Figure A1

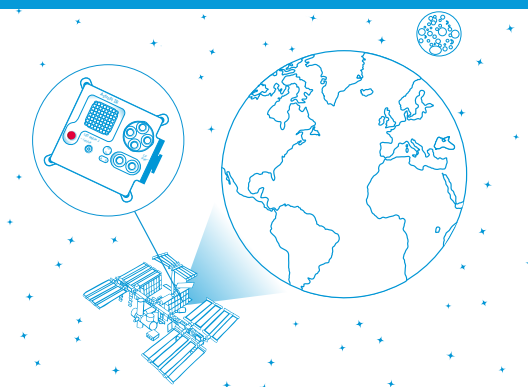


↑The electromagnetic spectrum categorises different types of radiation in order of wavelength, from the longest (radio) to the shortest (gamma-ray)

Infrared light is divided into different parts, just like visible light is divided into different colours. Near-infrared light, the part closest to red light, can be easily detected by the sensors used in digital cameras. Also Earth observation satellites carry scientific instruments designed to detect electromagnetic emissions from constituents of the Earth's surface and atmosphere allowing us to observe our planet in a new way.

Did you know?

Onboard the International Space Station (ISS) there is a very special infrared camera that can be used to take great pictures of Earth! The infrared camera is part of Astro Pi, a small computer with a set of sensors and gadgets that can be used to run great scientific experiments. Teams of students can program this small computer by participating in the European Astro Pi Challenge and use the Astro Pi's near-infrared camera to measure, for example, the health and density of vegetation on Earth.



→ Activity 1: Hacking the webcam

In this activity you are going to make an infrared camera by hacking a normal webcam. Usually, in all digital cameras and webcams there is an infrared filter behind the lens that filters out all infrared light in order to mostly capture visible light. This filter needs to be removed. Here you find simple instructions on how to hack your webcam to be able to see in near-infrared.

Equipment

- 1 webcam with a manual focus ring on the front
- 1 pin or scalpel
- 2 pieces of exposed photographic film or polarising filter
- Clear tape
- Scissors

Exercise

1. Disassemble the camera

Unscrew the focus ring in an anticlockwise direction until the whole lens can be pulled out.

2. Remove the infrared filter

On the inside of the lens there is a small piece of plastic with a red/green tint (see the left lens in Figure A2). This is the infrared filter. Using a pin or a scalpel, remove the filter. Be careful: this should be done very gently, as the filter can break if too much pressure is used.

3. Assemble the camera

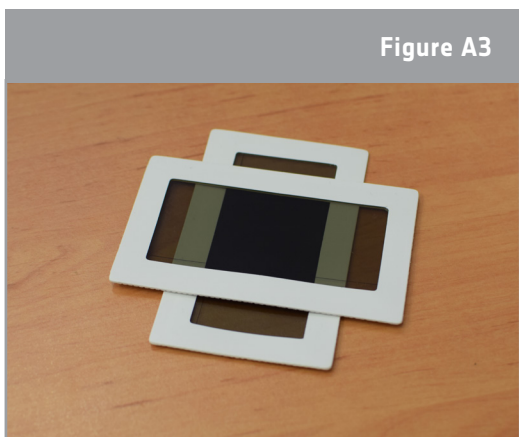
Screw the lens back onto the webcam and plug the webcam into a computer. It may be necessary to open video software to view an image through the webcam. Use the focus ring to adjust the focus until you have a clear image of the object that you wish to look at.

Figure A2



↑ How to make an infrared camera.

Figure A3



↑ Polarising filters.

The infrared webcam is now ready to be used!

Tip: If your image appears very bright on the screen, there is too much visible light which needs to be filtered out. For this, two pieces of polarising filter or exposed photographic film have to be put in front of the lens. Make sure the two pieces are put on one another perpendicularly. The filters can also be fixed with clear tape.

→ Activity 2: Looking at objects with an infrared camera

In this activity, you will use the hacked infrared webcam to make your own experiment about how objects look like when seen with visible and infrared light.

Equipment

- Infrared camera (from activity 1)
- Remote control
- Led light
- Candle
- Healthy plant and fake plastic plant

Exercise

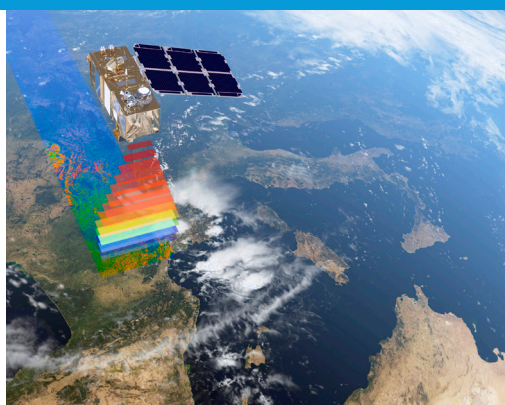
1. Look at the different objects firstly with your eyes (visible light) and then through the webcam (infrared light).
2. Fill in the table on the next page with your observations.



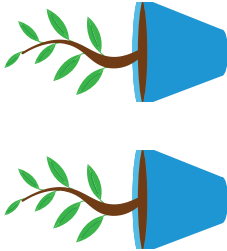
Discussion

Taking into consideration the results from your experiment, discuss with other students how infrared light can help us better understand what we see. Summarise your conclusions below.

Did you know?

The European Space Agency (ESA) has helped develop lots of satellites that use different types of cameras for looking at Earth. A group of missions called the Sentinels aim to improve our understanding and management of the Earth's environment. One of the missions is called Sentinel-2 and consists of two twin satellites. The cameras onboard the satellites take images in visible as well as in infrared light, and they cover the whole planet every five days! Sentinel-2 can be used to monitor plant growth, map changes in land cover, and monitor the world's forests.



Objects	Describe your observations		Explain your observations
	Visible light	Infrared light	
Remote control 			
LED vs. candle 			
Living vs. fake plants 			

→ Activity 3: Looking at Earth in infrared light

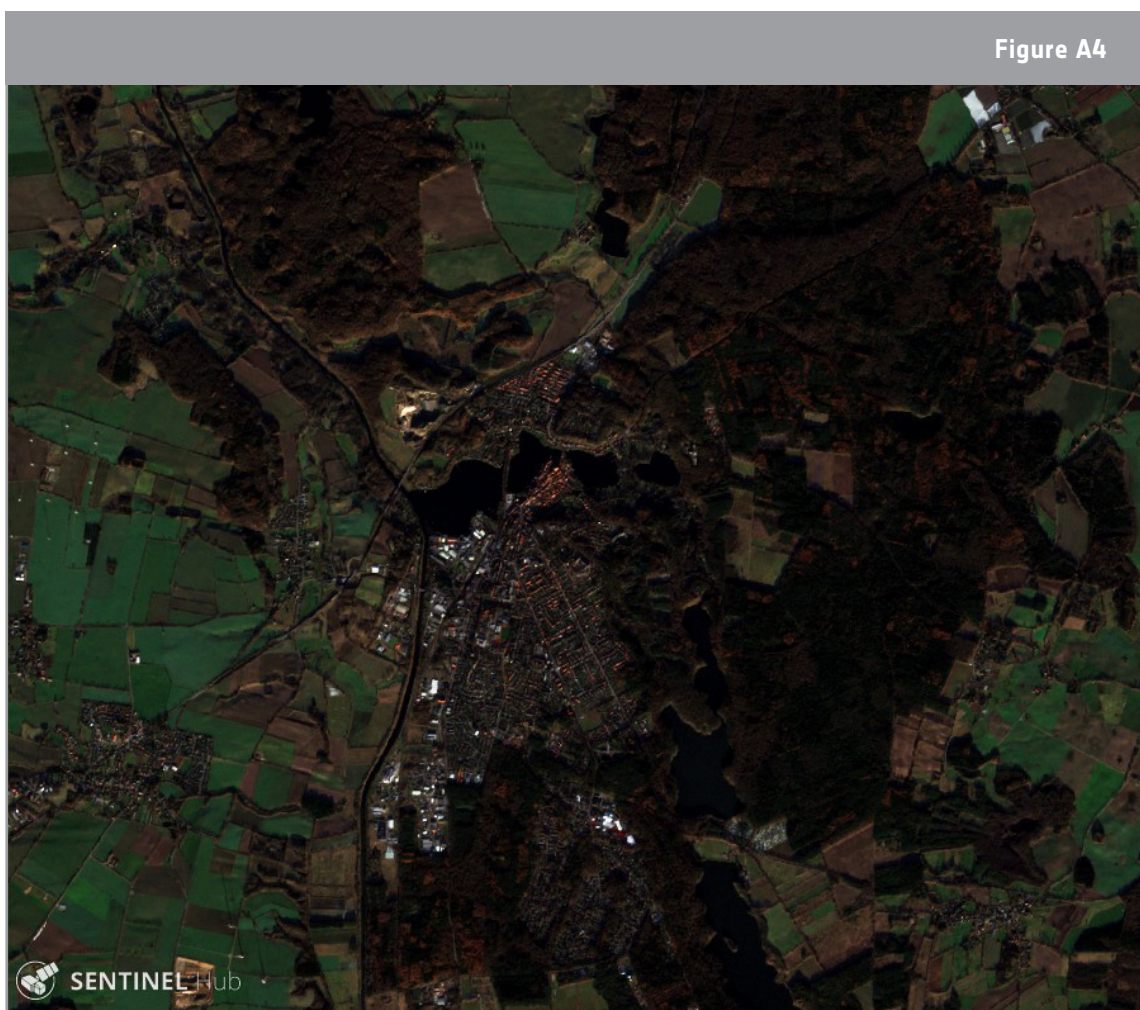
Infrared cameras are used in Earth observation satellites. With the help of computers, we can then visualise the light we cannot see with our own eyes. What comes out is a 'false colour image'. If we display the light visible to human eyes, we call it a 'true colour image'. A true colour image combines actual measurements of reflected red, green, and blue light, and shows the world as we see it. A false colour image uses at least one wavelength outside the visible range. As a result, the colours in the final image may not be what we expect them to be. For example, grass is not always green!

In this activity you will analyse satellite images and compare true colour images with false colour images. Will you be able to find the differences?

Exercise

1. Observe the true colour image below taken by the Sentinel-2 satellite (Northern Germany, 28.11.2016). Which of the following features can you identify?

- | | |
|----------------------|-------------|
| • Agriculture fields | • Lakes |
| • Snow | • Streets |
| • Forest | • Cars |
| • Clouds | • Buildings |
| • River | • People |



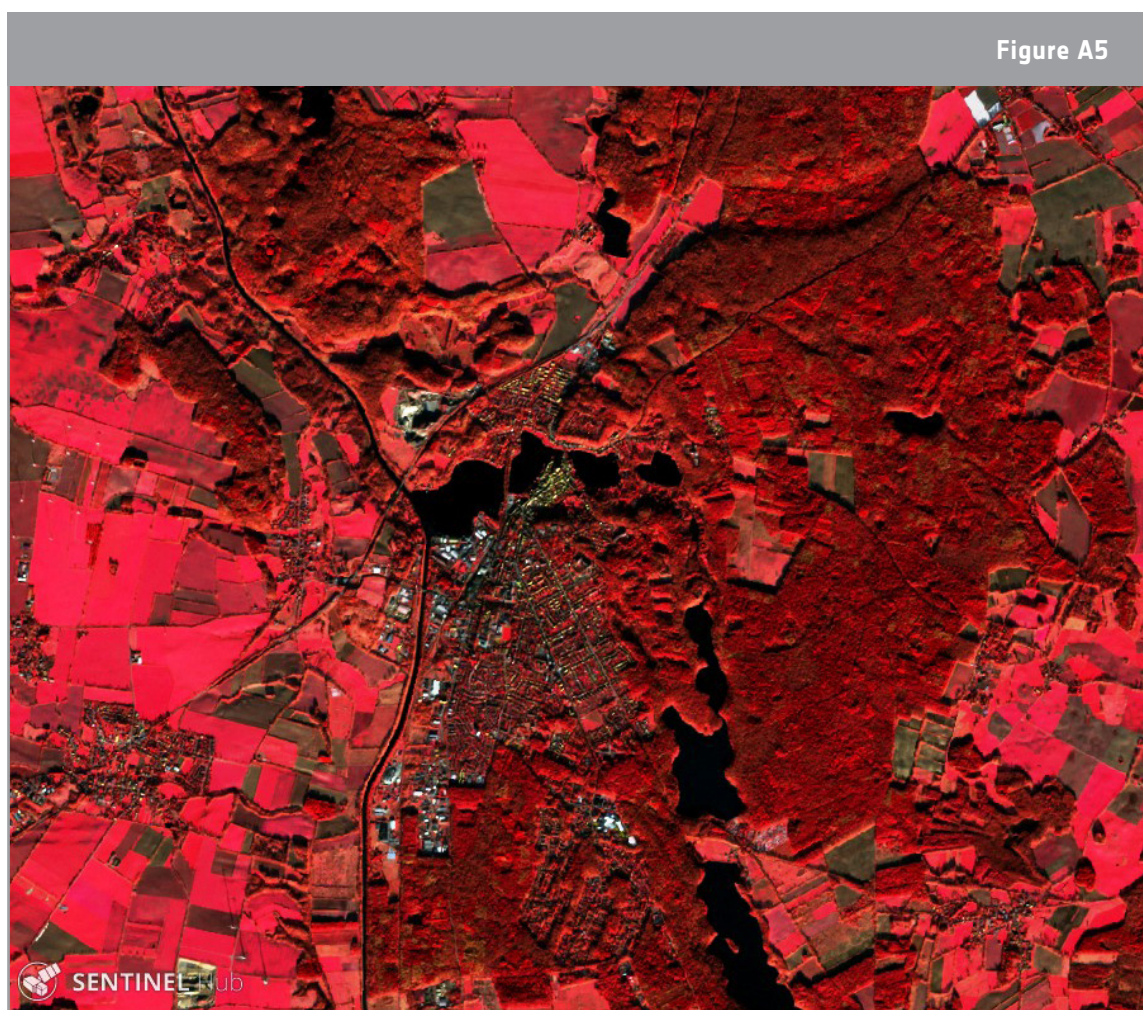
↑ True colour image taken by the Sentinel-2 satellite. Contains modified Copernicus Sentinel data [2017] processed by Sentinel Hub.

2. Observe the false colour image taken by the Sentinel-2 satellite (Northern Germany, 28.11.2016).

Note: The false colour image shows reflected near-infrared light as red.

- a. Try to find the features you previously observed. Can you also identify new features?

- b. What surface type/feature appears red in the false colour image? Distinguish between bright red and dark red.



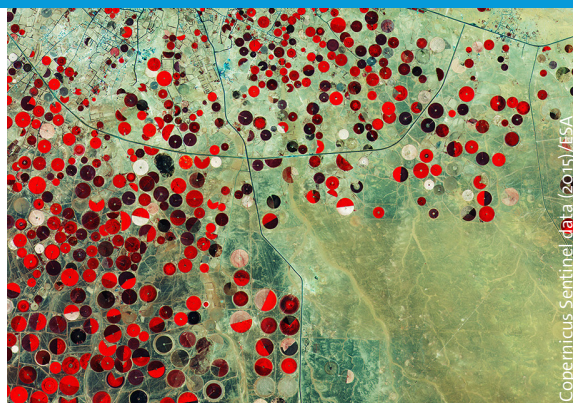
↑ False colour image taken by the Sentinel-2 satellite. Contains modified Copernicus Sentinel data [2017] processed by Sentinel Hub.

3. Describe the differences and similarities between the true colour image in Exercise 1 and the false colour image in Exercise 2.

4. Discuss the advantages and disadvantages of the true colour images and the false colour images showing near-infrared light.

Did you know?

This image from the Sentinel-2A satellite shows how Saudi Arabia's desert is being used for agriculture. The circles come from an irrigation system, where the long water pipe rotates around a well at the centre. It is a false colour image and the near-infrared is displayed in red. Plants reflect most of this light. These high reflection values explain the bright red of the irrigated fields. Near-infrared light is often used to monitor vegetation from space.



→ Links

ESA resources

ESA teach with space – infrared webcam hack video | VP15:

esa.int/spaceinvideos/Videos/2017/06/Infrared_webcam_hack_-_using_an_infrared_webcam_to_observe_the_world_in_a_new_way_-_classroom_demonstration_video_VC15

ESA classroom resources:

esa.int/Education/Classroom_resources

ESA space projects

ESA's Earth Observation missions

www.esa.int/Our_Activities/Observing_the_Earth/ESA_for_Earth

Sentinel -2

www.esa.int/Our_Activities/Observing_the_Earth/Copernicus/Sentinel-2

Extra information

Online platform to access satellite imagery

<https://apps.sentinel-hub.com/eo-browser>

Video Sentinel-2: an introduction

esa.int/spaceinvideos/Videos/2015/07/Sentinel-2_an_introduction

ESA Earth Observation Image of the Week

esa.int/spaceinimages/Sets/Earth_observation_image_of_the_week

A brightening of Jupiter's auroral 7.8- μm CH_4 emission during a solar-wind compression

J. A. Sinclair^{1*}, G. S. Orton¹, J. Fernandes^{1,2}, Y. Kasaba³, T. M. Sato⁴, T. Fujiyoshi⁵, C. Tao⁶, M. F. Vogt⁷, D. Grodent⁸, B. Bonfond⁸, J. I. Moses⁹, T. K. Greathouse¹⁰, W. Dunn¹¹, R. S. Giles¹, F. Tabataba-Vakili¹, L. N. Fletcher¹² and P. G. J. Irwin¹³

Enhanced mid-infrared emission from CH_4 and other stratospheric hydrocarbons has been observed coincident with Jupiter's ultraviolet auroral emission^{1–3}. This suggests that auroral processes and the neutral stratosphere of Jupiter are coupled; however, the exact nature of this coupling is unknown. Here we present a time series of Subaru-COMICS images of Jupiter measured at a wavelength of 7.80 μm on 11–14 January, 4–5 February and 17–20 May 2017. These data show that both the morphology and magnitude of the auroral CH_4 emission vary on daily timescales in relation to external solar-wind conditions. The southern auroral CH_4 emission increased in brightness temperature by about 3.8 K between 15:50 UT, 11 January and 12:57 UT, 12 January, during a predicted solar-wind compression. During the same compression, the northern auroral emission exhibited a duskside brightening, which mimics the morphology observed in the ultraviolet auroral emission during periods of enhanced solar-wind pressure^{4,5}. These results suggest that changes in external solar-wind conditions perturb the Jovian magnetosphere in such a way that energetic particles are accelerated into the planet's atmosphere, deposit their energy as deep as the neutral stratosphere, and modify the thermal structure, the abundance of CH_4 or the population of energy states of CH_4 . We also find that the northern and southern auroral CH_4 emission evolved independently between the January, February and May images, as has been observed at X-ray wavelengths over shorter timescales⁶ and at mid-infrared wavelengths over longer timescales⁷.

Images at 7.80- μm were obtained using Subaru-COMICS (Cooled Mid-Infrared Camera and Spectrograph) on 11–14 January, 4–5 February and 17–20 May 2017 (UT). A subset of these images is shown in Figs. 1 and 2, which respectively show southern and northern polar projections at times when the southern auroral region (SAR; 330°–60° W in system III longitude) and northern auroral region (NAR; centred at 180° W in system III longitude) were visible on the disk of Jupiter. These images demonstrate variability of both the magnitude and morphology of the 7.80- μm CH_4 emission over timescales of days to months. Further details of the measurements and processing are provided in the Methods and Supplementary Information.

In terms of the morphology, the strongest 7.80- μm emission in both auroral regions appears enclosed inside the statistical mean of the ultraviolet emissions of the main oval⁸. Figure 3 shows the results of ionosphere-to-magnetosphere mapping model calculations (see Methods) and demonstrates that the positions of strongest CH_4 emission in the auroral regions predominantly correspond to radial distances of more than 95 Jupiter radii (R_J); beyond the day-side magnetopause⁹ and potentially on open field lines. The exception is the morphology of the emission in the NAR at 16:13 UT on 12 January (Fig. 2a), when a poleward, duskside feature of stronger emission parallel to the eastern boundary of the statistical oval was observed. This feature was not present less than 24 h later (Fig. 2b) and we have ruled out variable atmospheric seeing conditions between these two nights as the source of this intermittent morphology (see Supplementary Fig. 2). A similar morphology for the ultraviolet auroral emission, described as the 'duskside-active region', has also been observed during periods of enhanced solar-wind pressure, and has been attributed to duskside/night-side reconnection associated with the Vasyliunas or Dungey cycles or velocity shears caused by changing flows on the nightside magnetospheric flank^{4,5,10}. Ionosphere-to-magnetosphere mapping calculations map 73° N, 155° W (an example location covered by the duskside feature) to roughly 100 R_J at a local time of 19.0 h. Unlike the NAR, the SAR does not appear to exhibit any smaller-scale morphology, although its position at a comparably higher latitude than the NAR reduces the effective spatial resolution and thus the ability to resolve smaller-scale features. In contrast to previous studies^{7,11}, we find no obvious movement in the longitudinal position of the southern auroral CH_4 emission.

To quantify temporal changes in the magnitude of the auroral emission and its relation to solar-wind conditions, we calculated the residual radiance between each auroral region and a lower-latitude zonal mean, henceforth named the auroral-quiescent residual ΔT_b (see Methods). Figure 4 compares the auroral-quiescent residual and uncertainty for both auroral regions and the results of a solar-wind propagation model (see Methods). The solar-wind propagation model predicts the arrival of a solar-wind compression at Jupiter at approximately 22:00 UT on 11 January, when the dynamical pressure was predicted to have increased from less than 0.1 nPa to 0.7 nPa. The auroral-quiescent residual increased from $\Delta T_b = 8.0 \pm 0.3$ K at

¹Jet Propulsion Laboratory, California Institute of Technology, Pasadena, CA, USA. ²Department of Physics and Astronomy, California State University, Long Beach, CA, USA. ³Planetary Plasma and Atmospheric Research Center, Tohoku University, Sendai, Japan. ⁴Space Information Center, Hokkaido Information University, Ebetsu, Japan. ⁵Subaru Telescope, National Astronomical Observatory of Japan, Hilo, HI, USA. ⁶National Institute of Information and Communications Technology, Tokyo, Japan. ⁷Center for Space Physics, Boston University, Boston, MA, USA. ⁸Université de Liège, STAR Institute, Laboratoire de Physique Atmosphérique et Planétaire, Liège, Belgium. ⁹Space Science Institute, Boulder, CO, USA. ¹⁰Southwest Research Institute, San Antonio, TX, USA. ¹¹Department of Space and Climate Physics, University College London, London, UK. ¹²Department of Physics and Astronomy, University of Leicester, Leicester, UK. ¹³Atmospheric, Oceanic and Planetary Physics, Clarendon Laboratory, University of Oxford, Oxford, UK.

*e-mail: james.sinclair@jpl.nasa.gov

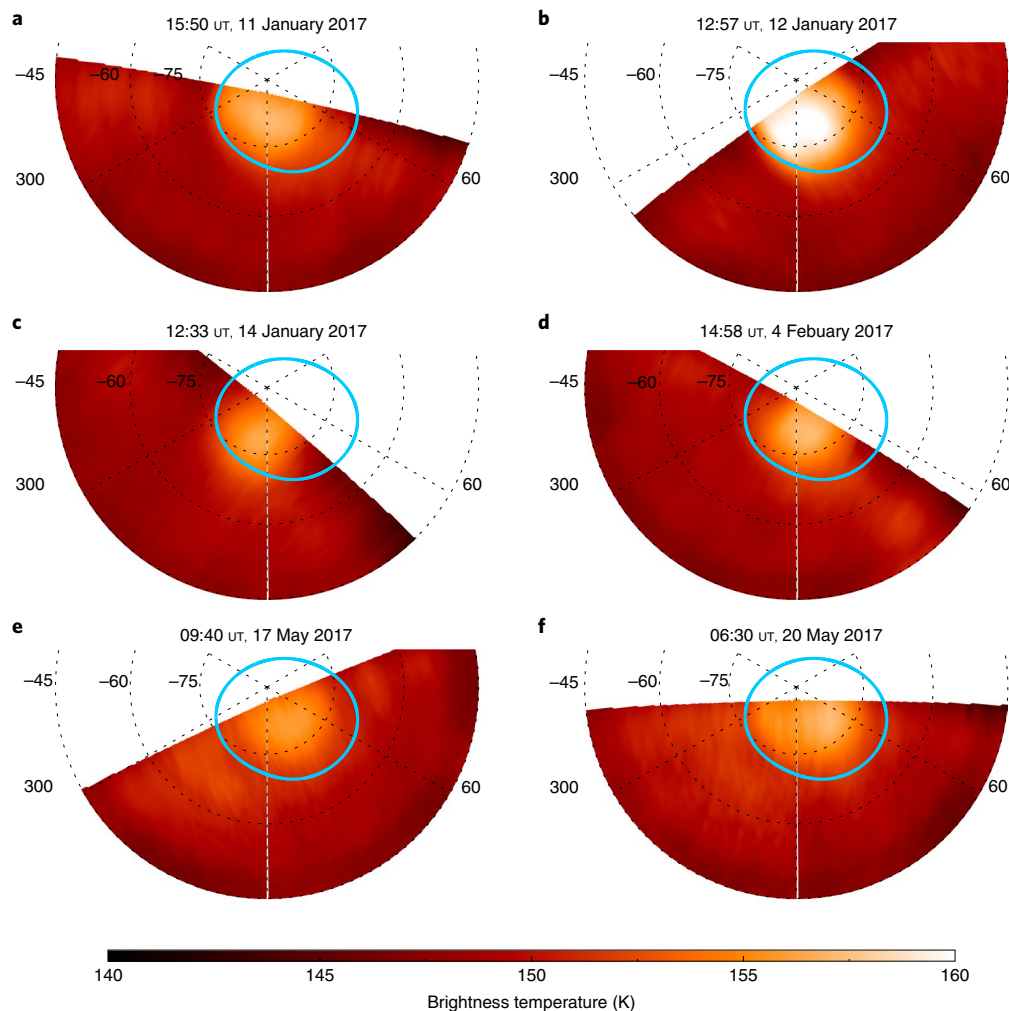


Fig. 1 | Southern polar projections of Jupiter's 7.80- μm CH_4 emission. a–f, Images were recorded by Subaru-COMICS on 11 January (a), 12 January (b), 14 January (c), 4 February (d), 17 May (e) and 20 May (f) 2017. These are a subset of the observations shown in Supplementary Fig. 1, when the SAR (330°–60° W, system III) was fully or partially visible on the disk. The colour scale indicates the brightness temperature. Solid light-blue lines represent the statistical-mean position of the ultraviolet auroral main oval emission⁸. For consistency with the Juno science team and the community supporting the Juno mission, increasing system III longitude is shown anticlockwise. All latitudes and longitudes are in degrees and are planetocentric and System III, respectively.

15:50 UT 11 January to $\Delta T_b = 11.8 \pm 0.5$ K at 12:57 UT 12 January—a net increase of 3.8 ± 0.6 K in brightness temperature T_b , or a roughly 25% increase in radiance. Although the viewing geometries of the SAR differ between these two images, forward-model calculations of the 7.80- μm emission (see Methods) at these two geometries differ by only 0.7 K in T_b and thus cannot explain all of the observed change. From 12:57 UT 12 January to 12:33 UT 14 January, the SAR returned to a brightness similar to that observed pre-compression; this brightness then remained roughly constant in all subsequent measurements (although variability between these measurements cannot be ruled out).

The NAR was not visible on the disk of Jupiter in the images taken on 11 January (before the solar-wind compression) and so we do not know whether it also brightened during the same solar-wind compression. However, the aforementioned duskside-active emission captured by COMICS at 16:13 UT on 12 January (Fig. 2a) occurred shortly after the solar-wind compression, which reiterates that this morphology is probably driven by enhanced solar-wind conditions and their perturbing effect on the nightside magnetosphere. From 16:13 UT 12 January to 12:30 UT 13 January, the auroral-quietest residual of the NAR was constant in time within uncertainty and

subsequently decreased significantly to 1.2 ± 1.1 K. Similarly, measurements in May show the NAR emission to be weak and comparable with, if not weaker than, lower-latitude regions. From 18 May to 19 May, there was a marginal increase in the emission in the NAR during a small solar-wind compression (about 0.2 nPa); however, the change in emission was not significant with respect to measurement uncertainty. Without measurements between 13 January, 5 February and 18 May, it is uncertain whether the NAR emission was consistently weaker in time or whether it exhibited short-term (daily or weekly) variability and the measurements by chance captured periods of weaker emission. We favour the latter possibility given that the measurements on 5 February and 17 May were preceded by at least seven days of steady, low-pressure (less than 0.05 nPa) solar-wind conditions. We note the results of a recent study¹², which showed that the total auroral power during a solar-wind compression exhibited a positive correlation with the duration of steady, quiescent solar-wind conditions preceding the compression. We also note that the northern auroral C_2H_6 emission was shown in previous work to weaken during periods of low solar activity, which similarly suggests a connection with solar-wind conditions on longer timescales¹³.

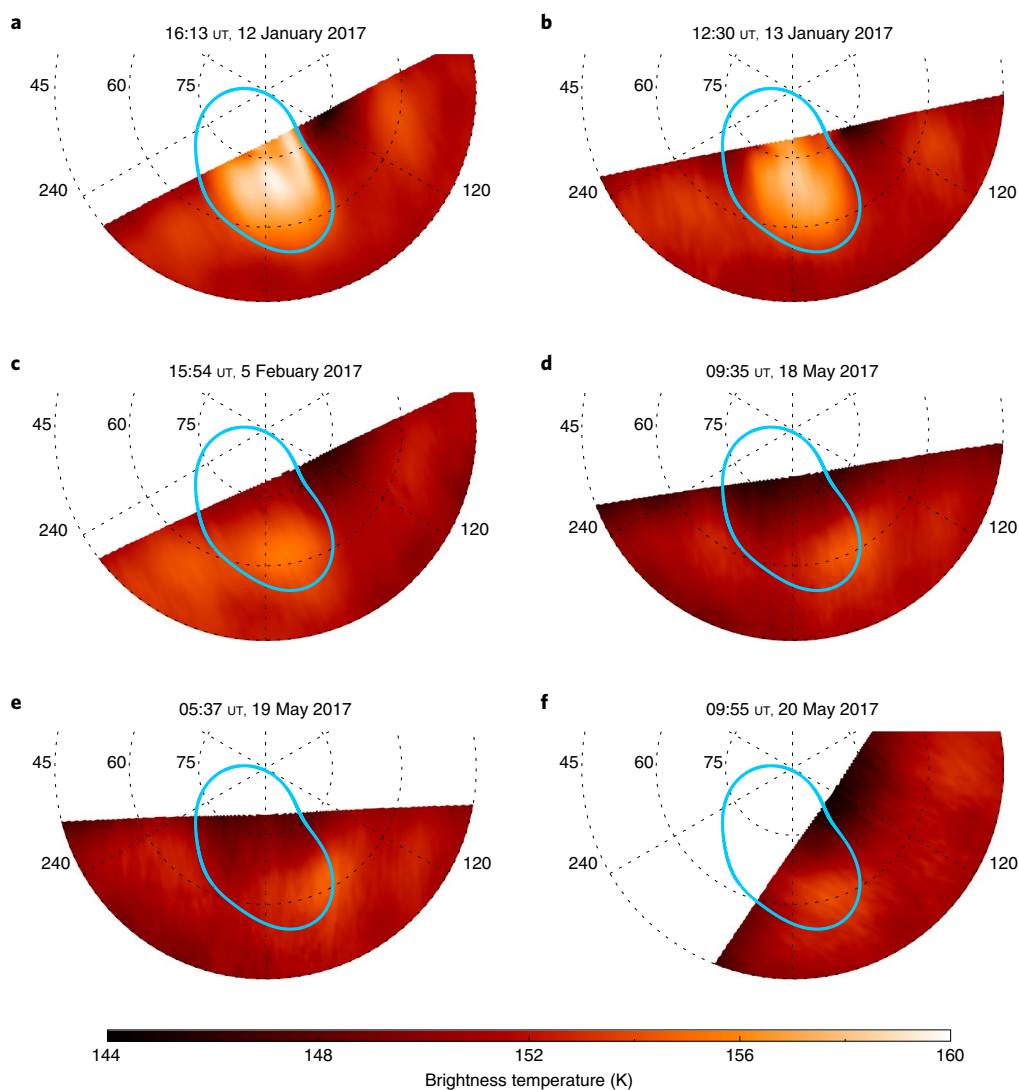


Fig. 2 | Northern polar projections of Jupiter's 7.80- μm CH_4 emission. **a–f**, Images were recorded by Subaru-COMICS on 12 January (**a**), 13 January (**b**), 5 February (**c**), 18 May (**d**), 19 May (**e**) and 20 May (**f**) 2017. These are a subset of the observations shown in Supplementary Fig. 1, when the NAR (centred at 180° W, system III) was fully or partially visible on the disk. The colour scale indicates the brightness temperature. Solid light-blue lines represent the statistical-mean position of the ultraviolet auroral main oval emission⁸. All latitudes and longitudes are in degrees and are planetocentric and System III, respectively.

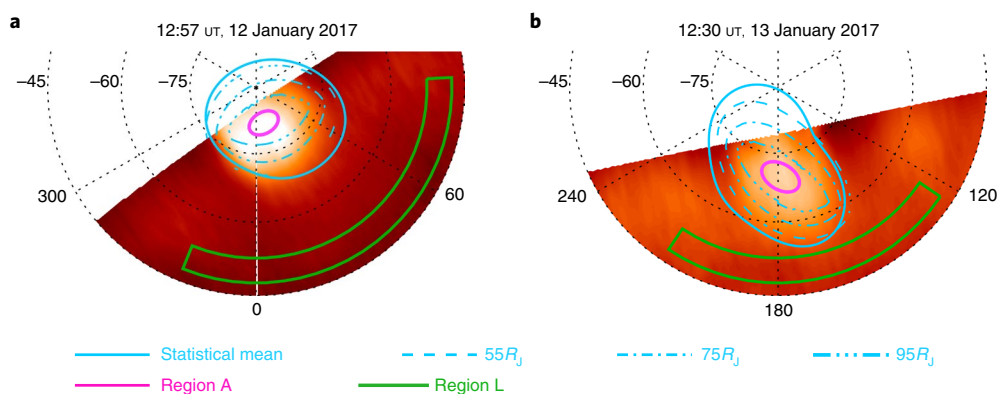


Fig. 3 | Polar projections and regions chosen for analysis. **a, b**, Subaru-COMICS 7.80- μm images recorded at 12:57 UT, 12 January 2017 (**a**; shown in the south) and 12:30 UT, 13 January 2017 (**b**; shown in the north), as in Figs. 1 and 2, shown again here for comparison with the ultraviolet main oval statistical mean⁸ and contours that map to different distances in the magnetosphere of Jupiter, as indicated in the legend. The region enclosed within the 95 R_J contour is interpreted to map to the outer magnetosphere/magnetopause. Regions A and L (enclosed within the magenta and green regions) were chosen to represent the auroral and non-auroral regions, respectively, for calculations of the relative radiance and its variability, as detailed in the Methods. All latitudes and longitudes are in degrees and are planetocentric and System III, respectively.

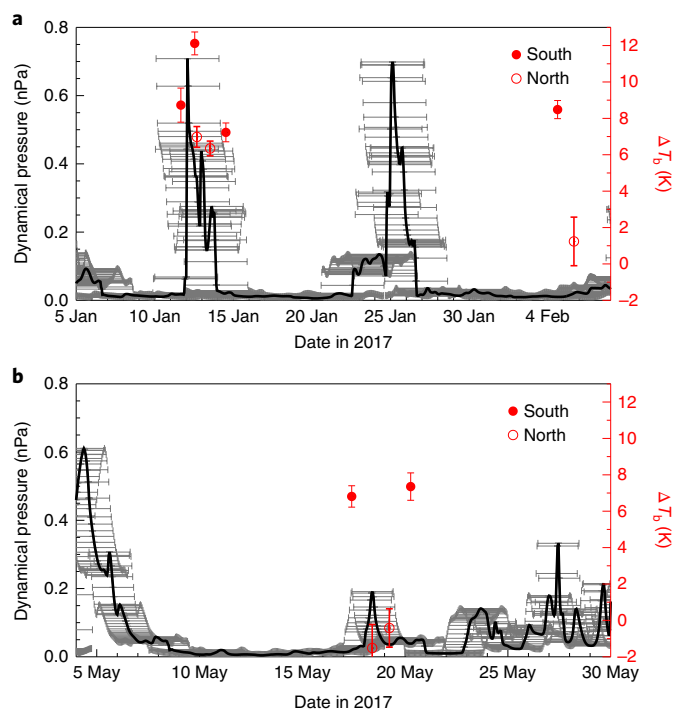


Fig. 4 | Auroral-quiescent residual over time. a,b, The residual 7.80- μm brightness temperature ΔT_b (left axis) between region A and region L, as described in the text and Methods, are shown as red circles with error bars. Results are shown for January 2017 (**a**) and May 2017 (**b**). Predicted solar-wind dynamical pressure at Jupiter (right axis; see Methods) is shown as the solid black line, with horizontal error bars showing the potential time error. The data suggest a brightening of Jupiter's southern auroral CH_4 emission in response to a solar-wind compression at approximately 22:00 UT on 11 January 2017.

The daily variability of the southern auroral CH_4 emission suggests that the source of the variability is in the upper stratosphere/mesosphere to thermosphere region (10–1 μbar), where the thermal inertial timescales are much shorter (around four weeks at 1 μbar)¹⁴ compared to the lower stratosphere (around 30 weeks at 1 μbar)¹⁴. We suggest that the observed changes in CH_4 emission result from: (1) variable auroral-related heating of the 10- to 1- μbar level, (2) auroral-driven changes in the vertical CH_4 profile near its homopause at roughly 1 μbar , (3) variable non-local thermodynamic equilibrium (non-LTE) effects that modify the population of energy states of CH_4 or (4) some combination of (1)–(3). To explore the first two possibilities and to determine what magnitude and type of change in the vertical temperature or CH_4 profiles could yield an increase in T_b of 3–4 K at 7.80 μm , we performed a series of radiative-transfer calculations using NEMESIS (see Methods).

As shown in Supplementary Fig. 5a,b, assuming the CH_4 abundance is held fixed, a 3–4-K change in T_b would require either: (1) the pressure level of the mesosphere–thermosphere transition to move deeper in the atmosphere by approximately a pressure-scale height or (2) the lapse rate in the thermosphere to increase by a factor of 2. The former corresponds to a total, atmospheric temperature increase of more than 100 K at the 0.5- μbar level, assuming a thermospheric lapse rate similar to that measured during Galileo's descent¹⁵, whereas the latter corresponds to a total, atmospheric temperature increase of about 20 K at 0.5 μbar . In steady state, thermospheric general circulation models show that the mesosphere-to-thermosphere transition pressure is deeper in the auroral regions compared to the non-auroral regions^{16,17}. Yates et al.¹⁸ performed time-dependent thermospheric circulation modelling to investigate

the response of the thermospheric structure and circulation to solar-wind compressions and expansion events. Between steady and compressed solar-wind conditions, the model predicted a warming of around 20 K and an increase in lapse rate near 70°N due to increased rates of joule heating at pressures lower than 1 μbar (with the lower model boundary set at 2 μbar). This is consistent with the two-fold increase of the thermospheric lapse rate required to brighten the 7.80- μm emission by 3–4 K, as detailed above.

As shown in Supplementary Fig. 5c, assuming a fixed vertical temperature profile, increasing the altitude of the CH_4 homopause (with respect to the Moses et al.¹⁹ model A CH_4 profile) by greater than a pressure-scale height would yield a 3–4-K increase in T_b at 7.80 μm . At the 0.2- μbar level, this would correspond to an increase in the volume mixing ratio of the order of 10^{-4} . In solving the vertical continuity equation assuming that the change in volume mixing ratio is driven entirely by advection and not a chemical source (that is $w = (-\Delta X/\Delta t)/(\Delta X/\Delta z)$, where w is the vertical velocity, X is the volume mixing ratio, t is time and z is height), a change in vertical wind of 2.7 cm s^{-1} with respect to the steady state would be required. The Bougher et al. thermospheric model¹⁶ predicts vertical winds near 70°S of approximately 50 cm s^{-1} at the 0.2- μbar level in steady state, and thus a change in vertical wind of 2.7 cm s^{-1} is reasonable. A higher-altitude homopause of CH_4 (and other hydrocarbons) in Jupiter's auroral regions was also found to optimize the consistency between Juno and Hisaki measurements²⁰.

Non-LTE effects are likely to be important at the altitudes where the source of variability has been inferred or could itself be the driver of the observed variability. In the absence of a strong radiation source, classical non-LTE effects become non-negligible at pressures below 0.1 mbar, where collisional timescales become longer than the spontaneous radiative lifetime^{21–23}. Without a sufficient number of thermal collisions, the population of rotational and vibrational energies deviates from the translational energy population and thus can no longer be described as a Boltzmann distribution. In comparison to non-auroral regions, the upper-stratospheric heating present in Jupiter's auroral regions^{7,24,25} also yields a larger contribution of photons at mid-infrared wavelengths from pressure levels where classical non-LTE processes become non-negligible. In addition, currents of electrons and ions in Jupiter's auroral regions and the resulting charged-particle collisions and dissociative recombinations may induce a non-Boltzmann population of the excited energy states of CH_4 . A further process might be ‘ H_3^+ shine’, whereby the downward flux of H_3^+ emission in lines in the 3–4 μm range ‘pump’ overlapping CH_4 ν_3 lines, exciting the vibrational modes and thereby modifying the population of lines responsible for the ν_4 band at approximately 7.80 μm (ref. ²⁶). Modelling of the aforementioned non-LTE processes will be the subject of future work.

We cannot distinguish between temperature, CH_4 abundance and non-LTE effects driving the variable CH_4 emission observed between 11 and 12 January 2017. Nevertheless, all of these processes describe a direct coupling of the neutral stratosphere in Jupiter's auroral regions to the external magnetosphere of Jupiter and solar-wind environment. Although daily variability of the northern auroral C_2H_4 and C_2H_6 emission has been observed in previous studies^{27,28}, we believe that the results presented here represent a substantial advance in the understanding of this phenomenon. First, the availability of solar-wind measurements and their modelled propagation to Jupiter's orbit allow the variability of the CH_4 emission to be tentatively linked to external solar-wind changes and their perturbing effect on the magnetosphere. Second, COMICS imaging at high-diffraction-limited spatial resolution allows the morphology of the CH_4 emission and its variability to be resolved at finer spatial details and mapped to the outer magnetosphere/magnetopause using ionosphere-to-magnetosphere mapping calculations. Auroral-related heating and chemistry dominate the forcing of the thermal structure and composition at Jupiter's poles^{7,24,25}; our results

suggest that these processes are directly connected to the external magnetosphere. This phenomenon could therefore be ubiquitous for rapidly rotating Jupiter-like exoplanets with an internal plasma source around a magnetically active star²⁹. In particular, magnetohydrodynamic simulations of a hot Jupiter at a close orbital separation of 0.05 au from its host star predict auroral powers several orders of magnitude larger than on Earth, affecting both polar and equatorial regions³⁰. The coupling of the neutral stratosphere and magnetosphere of Jupiter presented here may therefore be important in the near-future characterization of Jupiter-like exoplanets from the James Webb Space Telescope and of directly imaged planets whose atmospheres are sensed predominantly at higher latitudes.

Methods

COMICS 7.8- μm images. The COMICS^{31,32} instrument is mounted at the Cassegrain focus of the Subaru Telescope, which is located at the Mauna Kea Observatory (approximately 4.2 km above sea level). Subaru's 8.2-m primary aperture provides a diffraction-limited spatial resolution of approximately $0.24''$ at $7.8\ \mu\text{m}$, which corresponds to a latitude–longitude footprint of approximately $2.5^\circ \times 2^\circ$ at $\pm 70^\circ$ latitude. COMICS provides both imaging and spectroscopic capabilities over a spectral range of approximately $7\text{--}25\ \mu\text{m}$. Images are measured on a 320×240 array of Si:As blocked impurity band pixels each with a scale of $0.13''$, which provides a total field of view of $42'' \times 32''$. Images can be measured over a number of discrete filters in both the N band ($7\text{--}13\ \mu\text{m}$) and Q band ($17\text{--}25\ \mu\text{m}$). We focus on images obtained in the $7.80\text{-}\mu\text{m}$ filter, which is sensitive to Jupiter's stratospheric CH_4 emission (Supplementary Fig. 3). Images were measured on 11–14 January, 4–5 February and 17–20 May 2017. Measurements were performed during periods when Jupiter was available at airmasses lower than 3. The full disk of Jupiter (with equatorial diameters of approximately $36''$ in January, $39''$ in February and $42''$ in May) could not be measured in a single image by the COMICS field of view. In the January and February measurements, the full disk of Jupiter was measured using a 2×1 mosaic of individual images centred at Jupiter's mid-northern and mid-southern latitudes. In May, a 2×2 mosaic was conducted owing to Jupiter's larger size during this time period. For each individual image, A-frames (of Jupiter) and B-frames (dark sky $60''$ north of Jupiter) were continuously recorded over a total exposure time of 20 s. Further details of the measurements presented here are provided in Supplementary Table 1.

Imaging processing, calibration and error handling. Images were processed and calibrated using the Data Reduction Manager. A $-B$ subtraction was performed to remove telluric sky emission. The resulting images were then divided by a 'bad pixel mask' that accounts for corrupted pixels (due to cosmic ray damage, bright star saturation, manufacturer flaws, and so on) and by a flatfield to remove variations in pixel-to-pixel sensitivity across the detector. A limb-fitting procedure was used to assign latitudes, longitudes and local zenith angles to each pixel on the disk of Jupiter, using the known sub-observer latitude and longitudes at the time of each exposure. The absolute radiometric calibration of the images and correction for telluric absorption was conducted by scaling the observed lower-latitude zonal-mean brightness to those measured by Cassini's CIRS³³ instrument during the 2001 flyby. This procedure is described in greater detail in Fletcher et al.³⁴. We chose this method of calibration because experience with past mid-infrared images of Jupiter and Saturn has demonstrated that the radiometric calibration using a standard star provides inconsistency between datasets obtained on different nights^{34,35}. As detailed further in the Auroral–quiescent residual calculations section of Methods, our analysis of the images involved comparing the relative brightness of the auroral regions with a lower-latitude region over time, which negates errors introduced by offsets in the absolute calibration between nights. The reduced and radiometrically calibrated images are shown in Supplementary Fig. 1 in units of brightness temperature (T_b) at $7.80\ \mu\text{m}$. Portions of the image within 6 pixels (or approximately $0.8''$) of the assigned limb were removed as a conservative means of removing the effects of seeing and diffraction in blurring dark sky together with emission from Jupiter. The noise-equivalent spectral radiance was calculated by finding the standard-deviation emission of dark-sky pixels more than $1.5''$ (approximately 12 pixels) away from the planet. This was calculated for each image to capture changes in sensitivity due to variations in airmass and telluric atmospheric conditions between measurements. A centre-to-limb variation correction in the longitudinal direction was applied to correct for the foreshortening and limb-brightening, such that longitudes at different viewing geometries on different nights could be more readily compared. A power-law fit, of the form $\log R = a \log \mu + b$, where R is radiance, $\mu = \cos \theta$ and θ is the zenith emission angle, was performed in each latitude band to derive a centre-to-limb correction factor. For the January and February measurements, we performed the power-law correction using the image from 15:50 UT 11 January (Supplementary Fig. 1a) in the northern hemisphere and the image from 12:30 UT 13 January (Supplementary Fig. 1d) in the southern hemisphere. For the May measurements, the images from 09:40 UT 17 May and 09:35 UT 18 May (Supplementary Fig. 1i,j)

were similarly chosen to perform the power-law correction in the northern and southern hemispheres, respectively. These specific images were chosen because they best capture non-auroral longitudes in each hemisphere.

Ionosphere-to-magnetosphere mapping. We adopted the ionosphere-to-magnetosphere mapping calculation by Vogt et al.^{36,37} to map a location on the planet in planetocentric latitude and system III longitude to its position in radial distance and local time in the Jovian magnetosphere. The calculation is performed by imposing magnetic flux equivalence of a specified region at the equator to the area at which it maps in the ionosphere assuming a given internal field model. We adopted the VIPAL (Voyager Io Pioneer Anomaly Longitude) internal field model³⁸ owing to its validity in both the northern and southern hemispheres and to larger (roughly $95R_J$) radial distances. Stepping through latitude and longitude in increments of 1° polewards of $\pm 45^\circ$ latitude, the ionosphere-to-magnetosphere mapping calculation was performed to derive the local time and distance within the magnetosphere at each location. Regions enclosed within the statistical ultraviolet oval for which the calculation did not produce a real value were interpreted as mapping beyond the $95R_J$ limit of the model, which also marks the estimated position of the dayside magnetopause⁹. This calculation was used to derive the contours of distance shown in Fig. 3.

Auroral–quiescent residual calculations. Figure 3 demonstrates the areas denoted by region A and region L at high northern and high southern latitudes. Region A was chosen as a subregion of the auroral regions that mapped to the outer magnetosphere and was commonly sampled by all measurements presented in Figs. 1 and 2. Region L was chosen as a lower-latitude region away from the area of auroral influence, which is sampled at $\mu = \cos(\theta_{\text{em}})$ (where θ_{em} is the zenith emission angle on Jupiter) in the range $0.4 < \mu < 1$ in each image. By calculating the residual between region A and region L, any inconsistencies in the radiometric calibration from one night to the next are effectively removed, which would otherwise affect a comparison of the absolute radiance in time. The mean radiances within region A and region L were calculated. The 1σ uncertainty on the mean radiance in each region was chosen to be the larger of: (1) the noise-equivalent spectral radiance of each image (see the Imaging processing, calibration and error handling section of Methods) scaled by $1/\sqrt{n_p}$, where n_p is the number of pixels averaged, and (2) the standard deviation of the mean radiance in the region. The radiances and uncertainties were then converted to brightness-temperature units and the brightness-temperature residual and uncertainty were calculated.

Solar-wind propagation model. The Juno spacecraft continues to provide information on the magnetic and charged-particle fields while performing 53.5-day orbits inside Jupiter's magnetosphere. However, the Juno spacecraft cannot provide in situ measurements of the external solar-wind conditions outside Jupiter's magnetosphere. In the absence of such measurements, we look to modelling results. A solar-wind propagation model³⁹ was adopted to calculate the solar-wind dynamical pressure ($p_{\text{dyn}} = \rho v^2$, where ρ is the density and v is the velocity of the solar wind) impinging on Jupiter's magnetosphere. This model is used extensively for the magnetospheres of the outer planets^{40–42} in the absence of in situ measurements of the solar-wind conditions. The model adopts hourly measurements of the solar wind and magnetic field at the nose of Earth's bow shock from OMNI⁴³ as input and then performs 1D magnetohydrodynamic (MHD) calculations to model the solar-wind flow out to Jupiter's bow shock. The 1D model prediction of a 3D problem can introduce uncertainties on the arrival time and magnitude of the dynamical pressure of solar-wind compressions. When the magnitude of the Earth–Sun–Jupiter angle is less than 50° , the uncertainty of the arrival time of the solar-wind shock is less than ± 20 h and that of the maximum dynamic pressure is 38% (ref. 42). Given the Earth–Sun–Jupiter angles were between 80° and 120° in during January–February 2017, we adopted a 48-h time error on the results of the solar-wind propagation model. In May 2017, the Earth–Sun–Jupiter angle was approximately 18° and thus we assumed a time error of 20 h for May 2017. These values also seem to be commensurate with a statistical comparison of 1D MHD predictions and solar-wind data measured by several spacecraft⁴⁴. These errors are shown in Fig. 4.

Nemesis forward-model calculations. A single, broadband measurement of the CH_4 emission does not provide sufficient information to invert or retrieve atmospheric parameters and determine at what altitudes they vary. Nevertheless, we computed synthetic or forward-model spectra for a range of vertical temperature and CH_4 profiles to explore what changes in those atmospheric parameters could yield the observed $7.80\text{-}\mu\text{m}$ brightening of 3–4 K of the SAR. The NEMESIS forward model and retrieval tool⁴⁵ was adopted to compute forward-model spectra of the radiance in the COMICS $7.80\text{-}\mu\text{m}$ bandpass. Forward-model spectra were computed using the line-by-line method using the sources of line information for CH_4 , CH_3D and $^{13}\text{CH}_4$, C_2H_2 , C_2H_6 , NH_3 and PH_3 detailed in table 4 of Fletcher et al.⁴⁶. Calculations were performed using a square instrument function with a width of $0.04\ \text{cm}^{-1}$ (chosen on the basis of a balance of a sufficiently high spectral resolution to resolve both weak and strong emission lines while minimizing computational expense) and subsequently convolved with the COMICS $7.80\text{-}\mu\text{m}$ bandpass and the telluric transmission spectrum

(see Supplementary Fig. 2). The vertical temperature and CH_4 profiles were varied as detailed below. The remaining parameters of our model atmosphere, including the vertical C_2H_2 , C_2H_4 , C_2H_6 , NH_3 and PH_3 profiles, were held constant because they have negligible effect on the spectrum in the 7.80- μm bandpass. Further details of the model atmosphere are provided in Sinclair et al.²⁴. Note that the current NEMESIS forward model assumes LTE conditions, whereas conditions in the auroral regions may have departed from LTE, as discussed in the main text.

First, we kept the vertical CH_4 profile and its isotopologues fixed to the 'model A' vertical profile from Moses et al.¹⁹. Starting from the temperature profile shown in Supplementary Fig. 4a, we modified the vertical temperature profile in the range 0.1 mbar to 1 μbar , which includes the transition from the upper stratosphere/mesosphere to the thermosphere. The vertical temperature gradient (or lapse rate) in thermosphere was fixed and the pressure level of the mesosphere–thermosphere transition was varied as shown in Supplementary Fig. 5a. For each profile, a forward model was computed at the same viewing angle ($\mu = \cos(\theta_{\text{em}}) = 0.205$) as region A in the SAR at 12:57 UT 12 January (during the solar-wind compression). The synthetic spectrum was convolved with the 7.80- μm bandpass (as detailed above) and converted to T_{b} . These T_{b} values are shown in the legend in Supplementary Fig. 5a. Further sets of forward models and brightness temperatures were similarly computed, where the pressure level of the mesosphere–thermosphere transition was fixed at 0.2 μbar and the vertical temperature gradient (or lapse rate) was varied, as shown in Supplementary Fig. 5b.

Second, we fixed the vertical temperature profile as shown in Supplementary Fig. 4a. Starting from the vertical CH_4 profile derived from model A of Moses et al.¹⁹, the pressure level of the methane homopause was varied as shown in Supplementary Fig. 5c, and a forward-model radiance in the 7.80- μm bandpass was calculated and converted to T_{b} . These values are shown as the legend of Supplementary Fig. 5c.

Data availability

The COMICS images presented here are publicly available on the SMOKA (Subaru Mitaka Okayama-Kiso Archive) system (<https://smoka.nao.ac.jp/>). Reduced and calibrated images may be requested from J.A.S. The Data Reduction Manager is a suite of IDL software designed for reduction and processing of planetary images and is available in compressed format from G.S.O. on request (glenn.s.orton@jpl.nasa.gov). The ionosphere-to-magnetosphere mapping calculation is also written in IDL and is available from M.F.V. on request (mvogt@bu.edu). Results of the solar-wind propagation model in a specific time period may be requested from C.T. (chihiro.iao@nict.go.jp). The NEMESIS forward model and retrieval tool is written in Fortran and is available as a GitHub repository; a user account for this repository may be requested from P.G.J.I. (patrick.irwin@physics.ox.ac.uk).

Received: 24 August 2018; Accepted: 4 March 2019;

Published online: 08 April 2019

References

- Caldwell, J., Gillett, F. C. & Tokunaga, A. T. Possible infrared aurorae on Jupiter. *Icarus* **44**, 667–675 (1980).
- Kim, S. J., Caldwell, J., Rivolo, A. R., Wagener, R. & Orton, G. S. Infrared polar brightening on Jupiter. III. Spectrometry from the Voyager 1 IRIS experiment. *Icarus* **64**, 233–248 (1985).
- Flasar, F. M. et al. An intense stratospheric jet on Jupiter. *Nature* **427**, 132–135 (2004).
- Grodent, D., Gérard, J.-C., Clarke, J. T., Gladstone, G. R. & Waite, J. H. A possible auroral signature of a magnetotail reconnection process on Jupiter. *J. Geophys. Res. Space* **109**, A05201 (2004).
- Nichols, J. D. et al. Response of Jupiter's auroras to conditions in the interplanetary medium as measured by the Hubble Space Telescope and Juno. *Geophys. Res. Lett.* **44**, 7643–7652 (2017).
- Dunn, W. R. et al. The independent pulsations of Jupiter's northern and southern X-ray auroras. *Nat. Astron.* **1**, 758–764 (2017).
- Sinclair, J. A. et al. Independent evolution of stratospheric temperatures in Jupiter's northern and southern auroral regions from 2014 to 2016. *Geophys. Res. Lett.* **44**, 5345–5354 (2017).
- Bonfond, B. et al. The tails of the satellite auroral footprints at Jupiter. *J. Geophys. Res. Space* **122**, 7985–7996 (2017).
- Joy, S. P. et al. Probabilistic models of the Jovian magnetopause and bow shock locations. *J. Geophys. Res. Space* **107**, 1309 (2002).
- Grodent, D. et al. Jupiter's aurora observed with HST during Juno orbits 3 to 7. *J. Geophys. Res. Space* **123**, 3299–3319 (2018).
- Drossart, P. et al. Thermal profiles in the auroral regions of Jupiter. *J. Geophys. Res.* **98**, 18803 (1993).
- Kita, H. et al. Characteristics of solar wind control on Jovian UV auroral activity deciphered by long-term Hisaki EXCEED observations: evidence of preconditioning of the magnetosphere? *Geophys. Res. Lett.* **43**, 6790–6798 (2016).
- Kostiuk, T. et al. Variability of mid-infrared Aurora on Jupiter: 1979 to 2016. In *American Geophysical Union Fall Meeting 2016* P33C-2155 (AGU, 2016).
- Zhang, X. et al. Radiative forcing of the stratosphere of Jupiter, part I: atmospheric cooling rates from Voyager to Cassini. *Planet. Space Sci.* **88**, 3–25 (2013).
- Seiff, A. et al. Thermal structure of Jupiter's atmosphere near the edge of a 5- μm hot spot in the north equatorial belt. *J. Geophys. Res.* **103**, 22857–22890 (1998).
- Bougher, S. W., Waite, J. H., Majeed, T. & Gladstone, G. R. Jupiter thermospheric general circulation model (JTGCM): global structure and dynamics driven by auroral and Joule heating. *J. Geophys. Res. Planets* **110**, E04008 (2005).
- Gérard, J.-C. et al. Altitude of Saturn's aurora and its implications for the characteristic energy of precipitated electrons. *Geophys. Res. Lett.* **36**, L02202 (2009).
- Yates, J., Achilleos, N. & Guio, P. Response of the jovian thermosphere to a transient 'pulse' in solar wind pressure. *Planet. Space Sci.* **91**, 27–44 (2014).
- Moses, J. I. et al. Photochemistry and diffusion in Jupiter's stratosphere: constraints from ISO observations and comparisons with other giant planets. *J. Geophys. Res. Planets* **110**, E08001 (2005).
- Clark, G. et al. Precipitating electron energy flux and characteristic energies in Jupiter's main auroral region as measured by Juno/Jedi. *J. Geophys. Res. Space* **123**, 7554–7567 (2018).
- Appleby, J. F. CH_4 nonlocal thermodynamic equilibrium in the atmospheres of the giant planets. *Icarus* **85**, 355–379 (1990).
- Kim, S. J. Infrared processes in the Jovian auroral zone. *Icarus* **75**, 399–408 (1988).
- López-Puertas, M. & Taylor, F. *Non-LTE Radiative Transfer in the Atmosphere* (World Scientific, 2001).
- Sinclair, J. A. et al. Jupiter's auroral-related stratospheric heating and chemistry I: analysis of Voyager-IRIS and Cassini-CIRS spectra. *Icarus* **292**, 182–207 (2017).
- Sinclair, J. A. et al. Jupiter's auroral-related stratospheric heating and chemistry II: analysis of IRTF-TEXES spectra measured in December 2014. *Icarus* **300**, 305–326 (2018).
- Halthore, R. N., Allen, J. E. Jr & Decola, P. L. A non-LTE model for the Jovian methane infrared emissions at high spectral resolution. *Astrophys. J. Lett.* **424**, L61–L64 (1994).
- Kostiuk, T., Romani, P., Espenak, F. & Livengood, T. A. Temperature and abundances in the Jovian auroral stratosphere. 2: ethylene as a probe of the microbar region. *J. Geophys. Res.* **98**, 18823 (1993).
- Livengood, T. A., Kostiuk, T. & Espenak, F. Temperature and abundances in the Jovian auroral stratosphere. 1: ethane as a probe of the millibar region. *J. Geophys. Res.* **98**, 18813 (1993).
- Nichols, J. D. & Milan, S. E. Stellar wind-magnetosphere interaction at exoplanets: computations of auroral radio powers. *Mon. Not. R. Astron. Soc.* **461**, 2353–2366 (2016).
- Cohen, O., Kashyap, V. L., Drake, J. J., Sokolov, I. V. & Gombosi, T. I. The dynamics of stellar coronae harboring hot Jupiters. II. A space weather event on a hot Jupiter. *Astrophys. J.* **738**, 166 (2011).
- Kataza, H. et al. COMICS: the cooled mid-infrared camera and spectrometer for the Subaru telescope. *Proc. SPIE* **4008**, 1144–1152 (2000).
- Okamoto, Y. K. et al. Improved performances and capabilities of the cooled mid-infrared camera and spectrometer (COMICS) for the Subaru telescope. *Proc. SPIE* **4841**, 169–180 (2003).
- Flasar, F. M. et al. Exploring the Saturn system in the thermal infrared: the composite infrared spectrometer. *Space Sci. Rev.* **115**, 169–297 (2004).
- Fletcher, L. N. et al. Retrievals of atmospheric variables on the gas giants from ground-based mid-infrared imaging. *Icarus* **200**, 154–175 (2009).
- Parrish, P. D. et al. Saturn's atmospheric structure: the intercomparison of Cassini/CIRS-derived temperatures with ground-based determinations. *Bull. Am. Astron. Soc.* **37**, 680 (2005).
- Vogt, M. F. et al. Improved mapping of Jupiter's auroral features to magnetospheric sources. *J. Geophys. Res. Space* **116**, A03220 (2011).
- Vogt, M. F. et al. Magnetosphere-ionosphere mapping at Jupiter: quantifying the effects of using different internal field models. *J. Geophys. Res. Space* **120**, 2584–2599 (2015).
- Hess, S. L. G., Bonfond, B., Zarka, P. & Grodent, D. Model of the Jovian magnetic field topology constrained by the Io auroral emissions. *J. Geophys. Res. Space* **116**, A05217 (2011).
- Tao, C., Kataoka, R., Fukunishi, H., Takahashi, Y. & Yokoyama, T. Magnetic field variations in the jovian magnetotail induced by solar wind dynamic pressure enhancements. *J. Geophys. Res. Space* **110**, A11208 (2005).
- Badman, S. V. et al. Weakening of Jupiter's main auroral emission during January 2014. *Geophys. Res. Lett.* **43**, 988–997 (2016).
- Kinrade, J. et al. An isolated, bright cusp aurora at Saturn. *J. Geophys. Res. Space* **122**, 6121–6138 (2017).
- Lamy, L. et al. The aurorae of Uranus past equinox. *J. Geophys. Res. Space* **122**, 3997–4008 (2017).
- Thatcher, L. J. & Müller, H.-R. Statistical investigation of hourly OMNI solar wind data. *J. Geophys. Res. Space* **116**, A12107 (2011).

44. Zieger, B. & Hansen, K. C. Statistical validation of a solar wind propagation model from 1 to 10 AU. *J. Geophys. Res. Space* **113**, A08107 (2008).
45. Irwin, P. G. J. et al. The NEMESIS planetary atmosphere radiative transfer and retrieval tool. *J. Quant. Spectrosc. Rad. Transfer* **109**, 1136–1150 (2008).
46. Fletcher, L. N. et al. The origin and evolution of Saturn's 2011–2012 stratospheric vortex. *Icarus* **221**, 560–586 (2012).

Acknowledgements

All data presented were obtained at the Subaru Telescope, which is operated by the National Astronomical Observatory of Japan. COMICS observations obtained on 11, 12 January and 19, 20 May were proposed by and awarded to Y.K. using Subaru classical time. COMICS observations on 13, 14 January, 4, 5 February and 17, 18 May were proposed by and awarded to G.S.O. through the Keck-Subaru time exchange programme. We acknowledge the W. M. Keck Observatory, which is operated as a scientific partnership between California Institute of Technology, the University of California and NASA and supported financially by the W. M. Keck Foundation. We recognize and acknowledge the very important cultural role and reverence that the summit of Maunakea has always had within the indigenous Hawaiian community. We are most fortunate to have the opportunity to conduct observations from this mountain. The research was carried out at the Jet Propulsion Laboratory, California Institute of Technology, under a contract with NASA. We thank the NASA Postdoctoral and Caltech programmes for funding and supporting J.A.S. during this research. G.S.O. was supported by grants from NASA to the Jet Propulsion Laboratory/California Institute of Technology.

Author contributions

J.A.S. led the analysis of the observations and the preparation of this Letter. G.S.O. and Y.K. were principal investigators of the awarded telescope time. J.A.S., G.S.O., Y.K., T.M.S. and T.F. participated in the measurements at the Subaru Telescope. J.F. performed the reduction and calibration of the images. C.T. and M.F.V. provided model output for the interpretation of the results. P.G.J.I. is the lead developer of the NEMESIS code. All remaining authors contributed to the interpretation of the results and the preparation of the Letter.

Competing interests

The authors declare no competing interests.

Additional information

Supplementary information is available for this paper at <https://doi.org/10.1038/s41550-019-0743-x>.

Reprints and permissions information is available at www.nature.com/reprints.

Correspondence and requests for materials should be addressed to J.A.S.

Publisher's note: Springer Nature remains neutral with regard to jurisdictional claims in published maps and institutional affiliations.

© The Author(s), under exclusive licence to Springer Nature Limited 2019

A pulsating auroral X-ray hot spot on Jupiter

G. R. Gladstone^{*}, J. H. Waite, Jr.[†], D. Grodent[‡], W. S. Lewis^{*}, F. J. Crary[†], R. F. Elsner[§], M. C. Weisskopf[§], T. Majeed[†], J.-M. Jahn^{*}, A. Bhardwaj[§], J. T. Clarke^{||}, D. T. Young[†], M. K. Dougherty[¶], S. A. Espinosa[#] & T. E. Cravens[☆]

^{*} Southwest Research Institute, San Antonio, Texas 78228, USA

[†] University of Michigan, Ann Arbor, Michigan 48109, USA

[‡] NASA Marshall Space Flight Center, Huntsville, Alabama 35812, USA

[§] Vikram Sarabhai Space Centre, Trivandrum, India

^{||} Boston University, Boston, Massachusetts 02215, USA

[¶] Blackett Laboratory, Imperial College of Science and Technology, London SW7 2BZ, UK

[#] Max-Planck-Institut für Aeronomie, D-37191 Katlenburg-Lindau, Germany

[☆] University of Kansas, Lawrence, Kansas 66045, USA

Jupiter's X-ray aurora has been thought to be excited by energetic sulphur and oxygen ions precipitating from the inner magnetosphere into the planet's polar regions^{1–3}. Here we report high-spatial-resolution observations that demonstrate that most of Jupiter's northern auroral X-rays come from a 'hot spot' located significantly poleward of the latitudes connected to the inner magnetosphere. The hot spot seems to be fixed in magnetic latitude and longitude and occurs in a region where anomalous infrared^{4–7} and ultraviolet⁸ emissions have also been observed. We infer from the data that the particles that excite the aurora originate in the outer magnetosphere. The hot spot X-rays pulsate with an approximately 45-min period, a period similar to that reported for high-latitude radio and energetic electron bursts observed by near-Jupiter spacecraft^{9,10}. These results invalidate the idea that jovian auroral X-ray emissions are mainly excited by steady precipitation of energetic heavy ions from the inner magnetosphere. Instead, the X-rays seem to result from currently unexplained processes in the outer magnetosphere that produce highly localized and highly variable emissions over an extremely wide range of wavelengths.

Observations were made with the high-resolution camera (HRC) of the Chandra X-ray Observatory on 18 December 2000 for an entire 10-h Jupiter rotation (from 10–20 UT) in support of the Cassini fly-by of Jupiter. These observations show strong auroral emissions from high latitudes (Fig. 1) as well as a rather featureless

disk that probably results from a combination of reflected and fluoresced solar X-rays¹¹. The Chandra data are time-tagged and thus can be mapped into jovian latitude and system III longitude coordinates (system III longitudes are based on the 9.925-hour rotation period of Jupiter's magnetic field). Comparison of the resulting X-ray emission map with simultaneous far-ultraviolet images obtained by the Hubble Space Telescope imaging spectrograph (HST-STIS) shows that the northern auroral X-rays are concentrated in a 'hot spot' within the main ultraviolet auroral oval at high magnetic latitudes (Fig. 2).

The hot spot is located roughly at 60–70° north latitude and 160–180° system III longitude; no similar hot spot is seen in the south, but this is almost certainly due to the poor viewing geometry for the southern polar cap. We note that this same hot-spot region is the site of enhanced infrared emissions from CH₄ (ref. 4), C₂H₂ (ref. 5), C₂H₄ (ref. 6) and C₂H₆ (ref. 7), as well as highly variable H₂ emissions at far-ultraviolet wavelengths⁸, and a 'dark spot' in the sunlight reflected from Jupiter at mid-ultraviolet wavelengths¹².

Jupiter's main auroral oval lies at latitudes that map magnetically to radial distances near 30 jovian radii, R_J (refs 13–15); the location of the hot spot at latitudes poleward of the main oval indicates that the bulk of the jovian X-ray emissions must connect along magnetic field lines to regions in the jovian magnetosphere well in excess of 30 R_J from the planet. The Chandra HRC observations therefore call into question earlier views that attribute the X-ray auroral emissions to energetic particles diffusing planetward from the outer regions of the Io plasma torus and precipitating in the atmosphere at latitudes

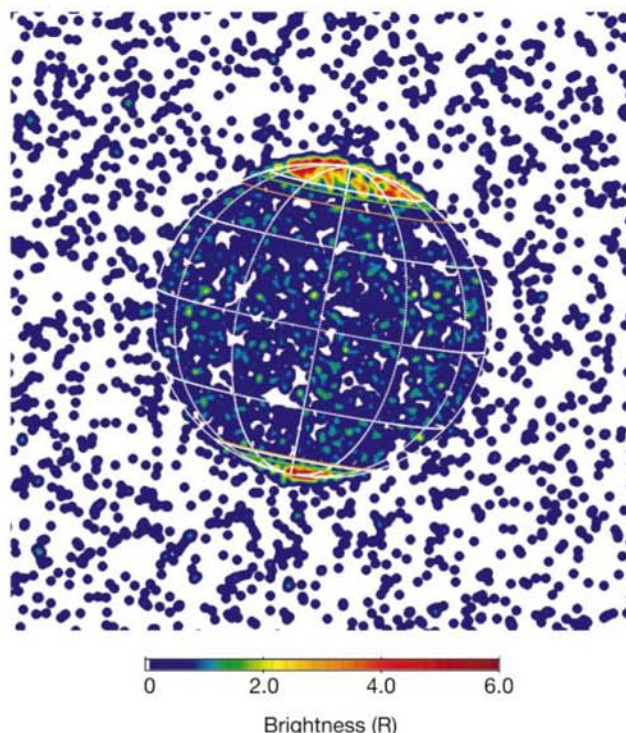


Figure 1 Chandra X-ray Observatory image of Jupiter on 18 December 2000. False colour brightnesses are indicated in rayleighs (R). The observation lasted 10 h (10–20 UT) and each X-ray photon has been smeared by double the 0.4-arcsecond full-width half-maximum point-spread-function of the high-resolution camera. A jovian-centric graticule with 30° intervals is overplotted, along with the maximum equatorward extent of the $L = 5.9$ (orange lines) and $L = 30$ (green lines) footprints of the VIP4 model¹⁶ magnetosphere. The auroral emissions are located at much higher latitudes than we expected on the basis of previous X-ray observations and indicate a connection with Jupiter's outer magnetosphere. An animation showing the time dependence of these observations may be viewed at http://pluto.space.swri.edu/yosemite/jupiter/chandra_hrc.html.

below those of the main oval³. On the other hand, our magnetic mapping of the hot spot to distances greater than $30R_J$ means that the source of the precipitating particles is unclear, because at such large distances from Jupiter there are insufficient S and O ions (B. H. Mauk, personal communication) to account for the hot-spot emissions. Another ion source or excitation mechanism (such as electron bremsstrahlung) must be considered.

Further evidence that some process other than energetic ion precipitation from the inner magnetosphere is responsible for the bulk of the observed auroral X-rays is provided by the lack of expected correlation between the X-ray emission morphology and the surface magnetic field strength (that is, the magnetic field strength at $1R_J$) as determined with the VIP4 model¹⁶ (Fig. 2). That is, for the nominal mechanism of generation by energetic ion precipitation, the brightest X-ray emissions would be expected where the eastward drifting (that is, toward lower longitude) ions encounter the most steeply decreasing surface magnetic field strength along their L-shell footprint (that is, the locus of intersection of their magnetic field lines with the surface of Jupiter) and only if the field strength is lower than in the conjugate hemisphere^{17,18}. Thus, although we would expect emissions at slightly higher latitudes than the $L = 5.9$ footprint of the Io plasma torus, at system III longitudes of 0° – 60° in the north and 120° – 260° in the south, we found minor clusters of X-rays near the $L = 5.9$ footprint near 140° in the north and 80° – 120° in the south.

A result even more puzzling than the high-latitude location of the X-ray hot spot is revealed when the X-ray counts are plotted as a function of time. The resulting light curve and power spectrum (Fig. 3) show a very strong ~ 45 -min oscillation in the emitted X-rays. One of the primary goals of the Chandra and HST campaigns supporting the Cassini fly-by was to search for transient auroral variations that might be related to the interaction of the solar wind

with Jupiter's magnetosphere. However, correlative Cassini solar-wind data acquired upstream at about $200R_J$ show no comparable periodicity, even accounting for the 5–10-h delay time for the propagation from the spacecraft to the planet. Likewise, no 45-min periodicities were seen in Galileo and Cassini energetic-particle and plasma-wave measurements at the time of the Chandra observations, although such periodicities are seen at other times (W. S. Kurth, personal communication). Forty-minute oscillations have been seen before in energetic particles in the outer magnetosphere and in radio waves^{9,10}. Following the Ulysses fly-by of Jupiter, intermittent bursts of 1–200-kHz radio emissions with an approximately 40-min period were observed for several months originating from high southern-jovian latitudes; these bursts were correlated with Ulysses measurements of solar-wind velocity and both relativistic (>8 MeV) and lower (~ 50 keV) energy electrons from Jupiter⁹. However, the origin of these quasi-periodic radio bursts has not been explained.

As there is no apparent correlation between the auroral X-rays and the solar-wind parameters measured by Cassini before and during the Chandra observations, it seems most likely that the oscillations arise from processes internal to the jovian magnetosphere. Global ultra-low-frequency (ULF) oscillations of the magnetic field and of the density of high-energy ions are ubiquitous in the jovian magnetosphere and are generally found to have periods in the 10–20-min range^{19,20}. Certain models of the ULF oscillations as standing waves along magnetic field lines indicate that spacecraft motion affects the measured periods so that they are closer to one hour in a reference frame that corotates with Jupiter¹⁹. The observed ULF oscillations may arise in a resonance with the bounce periods of the energetic particles (that is, the period for a magnetically trapped ion to repeat its north–south motion along a field line). Scattering of some portion of this particle population into the loss cone could

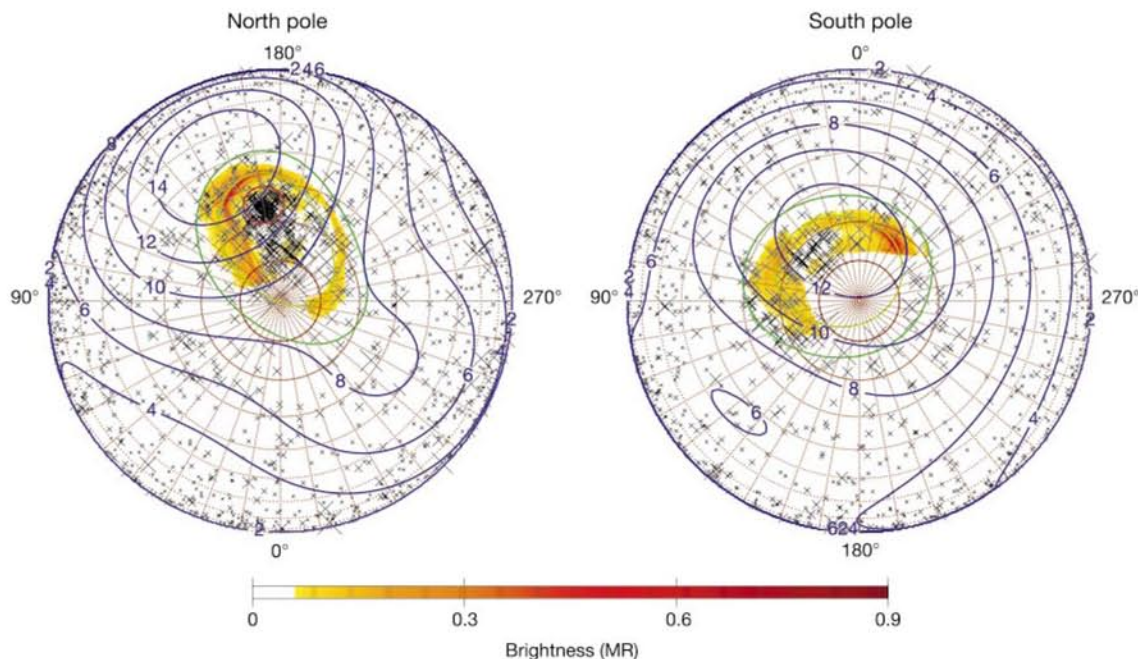


Figure 2 Polar projections of X-rays seen by Chandra and simultaneous far-ultraviolet images obtained by the Hubble Space Telescope. The mapped locations of individual X-ray photons (crosses) are overlaid on averages of several northern (left) and southern (right) auroral images made with the Hubble Space Telescope imaging spectrograph (HST-STIS) during 10–20 UT on 18 December 2000. The mapping assumes that the X-ray and ultraviolet auroras peak in emission at 240 km above the 1-bar pressure level. The size of each cross gives an approximate indication of the uncertainty in location of the corresponding X-ray photon, and only photons with emission angles of $<85^\circ$ are shown. The HST-STIS images made with the 25MAMA filter are displayed in false colour with

auroral H_2 emission brightnesses in megarayleighs (MR) as indicated by the colour bar. Surface VIP4 model¹⁶ magnetic field strength contours are shown for comparison (dark blue). The $L = 5.9$ and $L = 30$ footprints of the VIP4 model magnetosphere are also included (outer and inner green ovals, respectively), and a 10° graticule (brown dotted lines) with system III longitudes labelled. Most of the northern auroral X-rays are unexpectedly located well within the main far-ultraviolet oval and are coincident with the polar-cap far-ultraviolet emissions. The red circle in the northern auroral plot (left) shows the region defined for the hot spot used in the timing analysis. The apparent increase in X-rays toward the equator is an artefact of the polar projection.

result in quasi-periodic precipitation that would account for the periodicity observed in the X-ray emissions. However, bounce periods vary with particle energy, distance from Jupiter, and pitch angle, and it is unclear what would cause a narrow range of periods to dominate this resonance over much of the magnetosphere.

It is difficult to estimate the power in the emitted X-rays, because the Chandra HRC responds over a broad energy range (0.1–10 keV) with a variable sensitivity that peaks near an energy of 1.1 keV. We currently have no knowledge of the details of the emitted spectrum, so we can only make very rough estimates of the emitted power. Assuming a photon energy of 574 eV (corresponding to an O^{6+} emission feature expected to be bright in ion auroras or solar-wind charge exchange^{21,22}), the estimated X-ray luminosities of the disk of Jupiter and its northern and southern auroras are about 2.3, 1.0 and 0.4 GW, respectively. These results are consistent with previous observations made with low spatial resolution^{1,2}.

As we note above, it is difficult to account for the ion flux needed to produce the estimated luminosities with a source region located in the outer magnetosphere. If the emissions are indeed generated by heavy-ion precipitation, one possibility is high-latitude recon-

nection of the planetary and solar-wind magnetic fields, with the subsequent entry of the highly ionized (but low energy) heavy-ion component of the solar wind. The captured solar-wind ions could be accelerated to MeV energies by the field-aligned currents present in the outer magnetosphere^{22–24}. Such particles could also be consistent with the observed plasma waves. For example, the bounce period of 20 MeV oxygen ions on a dipole field line at $L = 120R_J$ with an equatorial pitch angle of 30° is about 38 minutes. Although outer magnetospheric field lines are not dipolar²⁵, they are close enough for this simple calculation to be informative. We wondered whether electron bremsstrahlung, originally rejected primarily on energetic grounds, should be reconsidered as an explanation for the X-rays. The energetics argument still holds: the power needed to produce the brightest far-ultraviolet ‘flares’ seen in the same polar-cap region as the X-ray hot spot is a few tens of TW (ref. 8), much less than the estimated power of a few PW (ref. 1) needed to produce the observed X-rays by electron bremsstrahlung. Thus, explaining the observed hot-spot X-rays with electron bremsstrahlung still seems unpromising. Whatever ultimate source is determined for the hot-spot X-rays, it should probably also account for the far-ultraviolet flare emissions, the various hydrocarbon infrared emissions, and possibly the mid-ultraviolet dark spot, as it is unlikely that these various phenomena occur in the same area of the upper atmosphere of Jupiter and yet are unrelated to one another. □

Received 3 August; accepted 18 December 2001.

- Metzger, A. E. *et al.* The detection of x-rays from Jupiter. *J. Geophys. Res.* **88**, 7731–7741 (1983).
- Bhardwaj, A. & Gladstone, G. R. Auroral emissions of the giant planets. *Rev. Geophys.* **38**, 295–353 (2000).
- Mauk, B. H. *et al.* Hot plasma parameters of Jupiter’s inner magnetosphere. *J. Geophys. Res.* **101**, 7685–7695 (1996).
- Caldwell, J. J., Halthore, R., Orton, G. & Bergstralh, J. Infrared polar brightenings on Jupiter. 4. Spatial properties of methane emission. *Icarus* **74**, 331–339 (1988).
- Drossart, P. *et al.* Enhanced acetylene emission near the north pole of Jupiter. *Icarus* **66**, 610–618 (1986).
- Kostiuk, T., Romani, P., Espenak, F., Livengood, T. A. & Goldstein, J. J. Temperature and abundances in the Jovian auroral stratosphere. 2. Ethylene as a probe of the microbar region. *J. Geophys. Res.* **98**, 18823–18830 (1993).
- Livengood, T. A., Kostiuk, T., Espenak, F. & Goldstein, J. J. Temperature and abundances in the Jovian auroral stratosphere. 1. Ethane as a probe of the millibar region. *J. Geophys. Res.* **98**, 18813–18822 (1993).
- Waite, J. H. Jr *et al.* An auroral flare at Jupiter. *Nature* **410**, 787–789 (2001).
- MacDowall, R. J. *et al.* Quasiperiodic jovian radio bursts: Observations from the Ulysses radio and plasma wave experiment. *Planet. Space Sci.* **41**, 1059–1072 (1993).
- Krimigis, S. M. *et al.* A nebula of gases from Io surrounding Jupiter. *Nature* **415**, 994–996 (2002).
- Maurellis, A. N. *et al.* Jovian x-ray emission from solar x-ray scattering. *Geophys. Res. Lett.* **27**, 1339–1342 (2000).
- Vincent, M. B. *et al.* Jupiter’s polar regions in the ultraviolet as imaged by HST/WFPC2: Auroral-aligned features and zonal motions. *Icarus* **143**, 205–222 (2000).
- Connerney, J. E. P., Baron, R., Satoh, T. & Owen, T. Images of excited H_2^+ at the foot of the Io flux tube in Jupiter’s atmosphere. *Science* **262**, 1035–1038 (1993).
- Clarke, J. T. *et al.* Hubble Space Telescope imaging of Jupiter’s UV aurora during the Galileo orbiter mission. *J. Geophys. Res.* **103**, 20217–20236 (1998).
- Prangé, R. *et al.* Detailed study of FUV jovian auroral features with the post-COSTAR HST faint object camera. *J. Geophys. Res.* **103**, 20195–20215 (1998).
- Connerney, J. E. P., Acuña, M. H., Ness, N. F. & Satoh, T. New models of Jupiter’s magnetic field constrained by the Io flux tube footprint. *J. Geophys. Res.* **103**, 11929–11939 (1998).
- Gehrels, N. & Stone, E. C. Energetic oxygen and sulfur ions in the jovian magnetosphere and their contribution to the auroral excitation. *J. Geophys. Res.* **88**, 5537–5550 (1983).
- Herbert, F., Sandel, B. R. & Broadfoot, A. L. Observations of the jovian UV aurora by Voyager. *J. Geophys. Res.* **92**, 3141–3154 (1987).
- Khurana, K. K. & Kivelson, M. G. Ultralow frequency MHD waves in Jupiter’s middle magnetosphere. *J. Geophys. Res.* **94**, 5241–5254 (1989).
- Wilson, R. J. & Dougherty, M. K. Evidence provided by Galileo of ultra low frequency waves within Jupiter’s middle magnetosphere. *Geophys. Res. Lett.* **27**, 835–838 (2000).
- Liu, W. & Schultz, D. R. Jovian x-ray aurora and energetic oxygen ion precipitation. *Astrophys. J.* **526**, 538–543 (1999).
- Cravens, T. E. Comet Hyakutake x-ray source: Charge transfer of heavy solar wind ions. *Geophys. Res. Lett.* **24**, 105–108 (1997).
- Bunce, E. J. & Cowley, S. W. H. Local time asymmetry of the equatorial current sheet in Jupiter’s magnetosphere. *Planet. Space Sci.* **49**, 261–274 (2001).
- Krupp, N. *et al.* Local time asymmetry of energetic ion anisotropies in the jovian magnetosphere. *Planet. Space Sci.* **49**, 283–289 (2001).
- Smith, E. J., Davis, L. Jr & Jones, D. E. in *Jupiter* (ed. Gehrels, T.) 788–829 (Univ. Arizona Press, Tucson, 1976).
- Leahy, D. A. *et al.* On searches for pulsed emission with application to four globular cluster x-ray sources: NGC 1851, 6441, 6624, and 6712. *Astrophys. J.* **266**, 160–170 (1983).

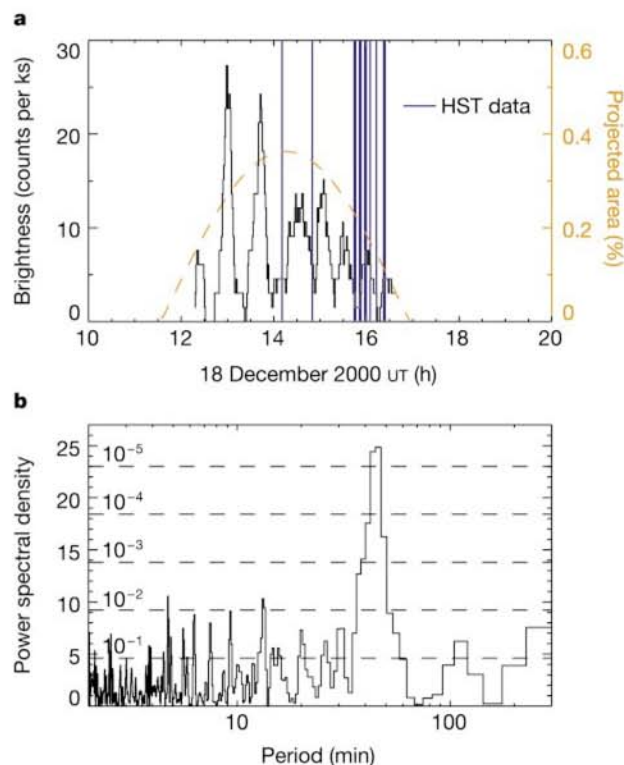


Figure 3 Light-curve and power-spectrum data for the auroral hot spot. **a**, Light curve showing the X-ray count rate measured by Chandra as a function of time for the auroral hot spot. Here we defined the hot spot region to include only those X-rays emitted within a 5° -radius circle centred on a latitude of 65° and a system III longitude of 170° (as shown by the red circle in Fig. 2). The total number of X-rays emitted from this region is 113, and the plot shows an 11-min boxcar smoothing of a 1-min binning of the data. The orange dashed line shows the projected area of the hot spot (as a percentage of the projected area of Jupiter). The times of the HST-STIS northern auroral region images shown in Fig. 2 are indicated by vertical purple lines. Unfortunately, no images were obtained during any of the bright X-ray pulses. **b**, Power spectrum of the hot spot signal, normalized so that, if the photons were randomly distributed over the visibility period, the mean power spectral density of any particular frequency bin would be expected to have a value of 2 (ref. 26). The peak at a period of approximately 45 min is clearly seen. The peak at 300 min is associated with the approximately 600-min rotation period of Jupiter. The dashed lines are labelled with the probability of a random signal exceeding that level in a particular frequency bin (for example, the 45-min period peak has a 4×10^{-6} likelihood of having been attained at random).

Acknowledgements

We thank B. H. Mauk, S. Krimigis, W. S. Kurth and M. Kaiser for helpful discussions. The support of the Chandra Project and the Smithsonian Astrophysical Observatory is gratefully acknowledged. A portion of this work is based on observations made with the NASA/ESA Hubble Space Telescope, obtained at the Space Telescope Science Institute, which is operated by the Association of Universities for Research in Astronomy, Inc.

Correspondence and requests for materials should be addressed to G.R.G.
(e-mail: randy@whistler.space.swri.edu).

Exoplanetary Atmospheres: Key Insights, Challenges and Prospects

Nikku Madhusudhan¹

¹Institute of Astronomy, University of Cambridge, Cambridge, UK, CB3 0HA;
email: nmadhu@ast.cam.ac.uk

xxxxxx 0000. 00:1–59
Copyright © 0000 by Annual Reviews.
All rights reserved

Keywords

Extrasolar planets, exoplanetary atmospheres, planet formation, habitability, atmospheric composition

Abstract

Exoplanetary science is on the verge of an unprecedented revolution. The thousands of exoplanets discovered over the past decade have most recently been supplemented by discoveries of potentially habitable planets around nearby low-mass stars. Currently, the field is rapidly progressing towards detailed spectroscopic observations to characterise the atmospheres of these planets. While various surveys from space and ground are expected to detect numerous more exoplanets orbiting nearby stars, the imminent launch of JWST along with large ground-based facilities are expected to revolutionise exoplanetary spectroscopy. Such observations, combined with detailed theoretical models and inverse methods, provide valuable insights into a wide range of physical processes and chemical compositions in exoplanetary atmospheres. Depending on the planetary properties, the knowledge of atmospheric compositions can also place important constraints on planetary formation and migration mechanisms, geophysical processes and, ultimately, biosignatures. In the present review, we will discuss the modern and future landscape of this frontier area of exoplanetary atmospheres. We will start with a brief review of the area, emphasising the key insights gained from different observational methods and theoretical studies. This is followed by an in-depth discussion of the state-of-the-art, challenges, and future prospects in three forefront branches of the area.

Contents

1. Introduction	2
2. Observational Methods	7
2.1. Transit Spectroscopy	7
2.2. High-resolution Doppler Spectroscopy	9
2.3. Direct Imaging	10
3. Theoretical Advancements	13
3.1. Self-consistent Models	13
3.2. Atmospheric Retrieval	15
3.3. Disequilibrium Models	16
4. Atmospheric Characterisation of Exoplanets	17
4.1. Chemical Compositions	18
4.2. Clouds/Hazes	23
4.3. Temperature Structures	24
4.4. Atmospheric Dynamics	26
4.5. Atmospheric Escape	28
5. Implications for Planetary Formation	29
5.1. The Basic Picture	29
5.2. Compositions of Accreted Material	30
5.3. End-to-end Studies	30
6. Habitable Planets and Biosignatures	34
6.1. Habitable Planets	35
6.2. Biosignatures	35
6.3. Observational Prospects	36
7. Future Landscape	37
7.1. Exoplanetary Atmospheres with Current Facilities	37
7.2. Exoplanetary Atmospheres with JWST	38

1. Introduction

Planetary atmospheres serve as Rosetta Stones for planetary processes. Encoded in the spectrum of a planetary atmosphere is information about its various physical and chemical properties which in turn provide key insights into myriad atmospheric processes as well as the formation and evolutionary history of the planet. Over a century of spectroscopic observations of planets and moons in the solar system have revealed a vast treasury of information on their diversity in all these aspects. From the giant storms and NH_3 clouds on Jupiter to the dense sulphuric clouds on Venus, from H_2 -rich giant planets to CO_2 -rich Venus and Mars, and then the unique Earth, the atmospheric diversity of the solar system is a sight to behold for the intrepid explorer. Yet, all the breathtaking diversity of the solar system arises from a surprisingly limited range of macroscopic planetary parameters from a cosmic context. The equilibrium temperatures of the solar system planets lie between 50 and 500 K, with only Venus and Mercury being above 300 K. The planetary sizes and masses fall in three broad ranges - the gas giants ($8\text{--}11 R_\oplus$, $\sim 100\text{--}320 M_\oplus$), the ice giants ($4 R_\oplus$, $\sim 14\text{--}17 M_\oplus$), and the terrestrial planets ($\leq 1 R_\oplus$, $\leq 1 M_\oplus$). In contrast, the thousands of exoplanets known today span a range in bulk properties that would have been considered impossible two decades ago with temperatures ranging between 200 - 4000 K and radii and masses spanning continuously over a large range ($\sim 0.5\text{--}20 R_\oplus$, $\sim 1\text{--}10^4 M_\oplus$).

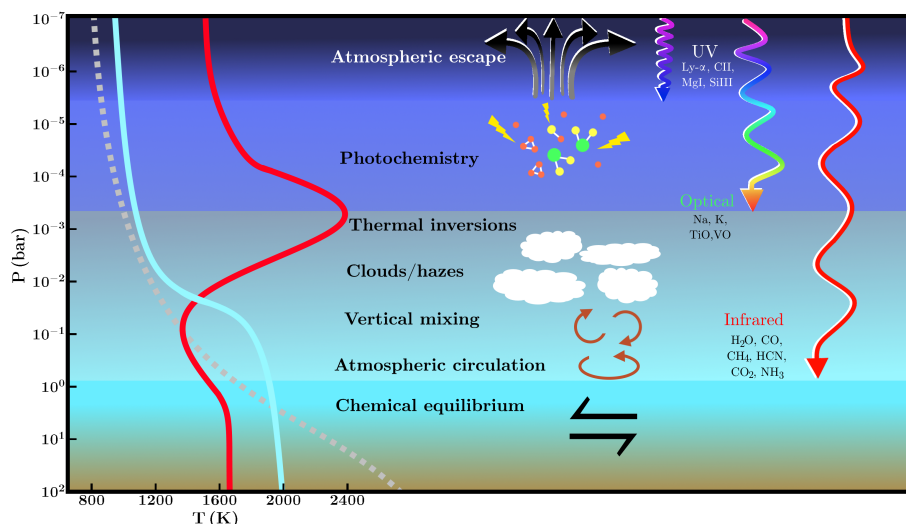


Figure 1: Processes active in exoplanetary atmospheres and how they are probed by different parts of the electromagnetic spectrum. These processes occur in different regions of the atmosphere and are labelled at the relevant location. On the right, the penetration depths of UV, optical and infrared light are shown, indicating which processes can be probed by observations in each wavelength range. The chemical species whose signatures can be detected in each wavelength range are also indicated. On the left are shown three types of temperature profile which can arise as a result of atmospheric processes: the profile of a highly-irradiated planet with a thermal inversion (red), that of an irradiated planet without a thermal inversion (cyan), and the temperature profile of a poorly irradiated planet (grey, dashed).

It is only natural then that the atmospheres of these exoplanets may also be expected to be similarly diverse. As such, exoplanetary atmospheres serve as excellent laboratories to study planetary processes and formation mechanisms over the entire possible range of macroscopic properties - masses, radii, temperatures/irradiation, orbital architectures, and host stellar types.

The information obtained about an exoplanetary atmosphere depends on the nature of observations. Figure 1 shows a schematic of atmospheric processes that can be observed in exoplanets with different spectral ranges probing different regions, and hence different processes, in the atmosphere. The different atmospheric processes can be understood as a function of the pressure (P) in the atmosphere. Deep in the atmosphere ($P \gtrsim 1$ bar) the pressure and temperature, and hence density and opacity, are high enough that thermochemical equilibrium and radiative-convective equilibrium prevail, i.e., chemical reactions occur faster than kinetic processes. The resulting composition then is that which minimises the Gibbs free energy of the system for the given temperature, pressure, and elemental abundances. Higher up in the atmosphere, between ~ 1 mbar and ~ 1 bar, various processes become more prevalent including atmospheric dynamics, clouds/hazes, and temperature inversions, as a result of complex interplay between the incident radiation field, chemical

composition, and other planetary properties. These processes strongly influence, and are influenced by, the atmospheric chemical composition and temperature structure both of which can be out of equilibrium. Further up in the atmosphere ($P \sim 10^{-6} - 10^{-3}$ bar), the low density and high radiation field cause photochemical processes to govern the atmospheric composition through photodissociation of prominent molecules into their constituent atomic species and formation of new ones. Eventually, at very low pressures, atmospheric escape of atomic species lead to mass loss from the atmosphere. Therefore, each region of the atmosphere provides a window into specific physicochemical processes. At the same time, different chemical species and different regions of the atmosphere are accessible to different parts of the electromagnetic spectrum. Prominent molecular species (e.g. H_2O , CO , CO_2 , CH_4 , etc) absorb primarily in the infrared due to rovibrational transitions, with the exception of some heavy metal species (TiO , VO , TiH , etc.) which also have strong visible absorption. On the other hand, atomic species absorb primarily in the optical and UV, depending on the excitation and ionisation states. Therefore, while UV observations probe the uppermost regions of the atmosphere where the composition is entirely atomic, the infrared observations probe lower regions of the atmosphere where the composition is primarily molecular, with optical spectra probing intermediate regions. Thus the spectral range of observations governs the region in the atmosphere probed and the corresponding physicochemical properties and processes.

The study of exoplanetary atmospheres has progressed at a tremendous pace in recent years. Just a decade ago, fewer than 25 transiting exoplanets were known and the first directly imaged planets were just being discovered. Observations of exoplanetary atmospheres were still in their infancy. Prior to that, only a handful of atomic species were detected robustly, mostly in the two famous transiting hot Jupiters HD 209458b and HD 189733b, using transmission spectra in the optical and UV obtained with the Hubble Space Telescope (HST) (50, 272). The first detections of exoplanetary atmospheres using multi-band space-based infrared photometry and spectrophotometry with Spitzer and HST were being made (51, 96, 258). The instruments used for these early measurements (such as the HST NICMOS spectrograph and Spitzer photometric instruments) were never designed for exoplanetary observations which require extreme sensitivities (e.g., photometric precisions better than $\sim 10^{-4}$). As such, the early measurements were intensely debated for their accuracy and several were subsequently revised as the systematics were better understood and analysis methods improved. This in stark contrast to the present day as high confidence and reproducible detections of exoplanetary spectra with HST are routine, as discussed below. At the same time the first attempts for transit spectroscopy from the ground were also being made (214, 246). Even so, inferences of molecular absorption and pressure-temperature profiles (e.g. thermal inversions) relied heavily on forward models with solar-like elemental compositions and equilibrium conditions (125, 43). Statistical constraints on atmospheric properties of exoplanets using atmospheric retrieval methods were still a dream for the future. On another front, the first thermal phase curves, and brightness maps, were being observed for hot Jupiters using infrared photometry with the Spitzer space telescope (126). At the same time, the first three-dimensional atmospheric circulation models were being developed for hot Jupiters (237) to explain the observed thermal phase curves. In summary, about a decade ago major observational facilities were being pushed to their limits to detect spectra of transiting exoplanets. At the same time, concomitant developments in theory were being pursued to explain the extant observations, however sparse. Such were the humble beginnings of atmospheric characterisation of exoplanets a decade ago.

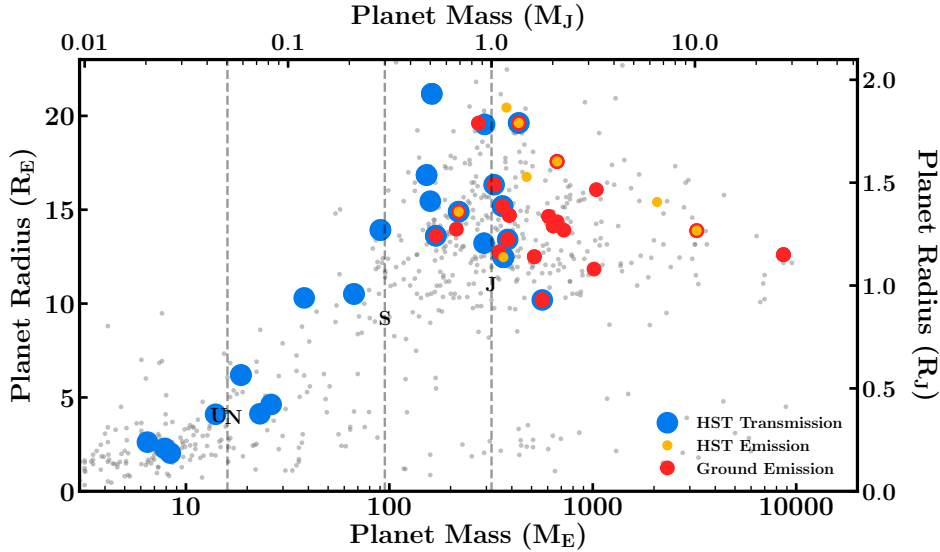


Figure 2: Masses versus radii of transiting exoplanets whose atmospheres have been observed. Planets with HST transmission/emission observations are shown by blue/yellow circles, respectively. Emission observations from ground-based facilities are shown in red. All known planets in this mass and radius range, with or without atmospheric observations, are shown for reference as grey points. Solar System planets are denoted in black by their initials and represented by the vertical dashed lines. Data obtained from the NASA Exoplanet Archive at <https://exoplanetarchive.ipac.caltech.edu/>.

Fast forward to the present - the field has transformed beyond recognition. Firstly, robust detections of exoplanetary atmospheric spectra are routinely made today using a variety of techniques: transit spectroscopy (50), direct imaging (174), as well as Doppler spectroscopy (251), both from space as well as the ground. Here, robustness of a result implies high statistical significance of a detection and its reproducibility by multiple groups using the same dataset. The space-based instruments used for the purpose in recent years are mainly HST spectrographs such as WFC3 in the near-infrared (177, 63) and STIS in the optical and UV (244, 71), and until recently the Spitzer IRAC 1 and 2 bands in the infrared (65), all of which have been very well characterized compared to the early observations a decade ago. Atmospheres of nearly a hundred exoplanets have been detected using at least one technique in at least one spectral band, as shown in Fig. 2. However, meaningful constraints on atmospheric properties require more than a few photometric observations. The required high-precision spectra over a broad spectral range have been observed for tens of giant exoplanets resulting in robust inferences of their chemical and/or thermal properties. Beyond detecting atmospheric spectra (63), the advent of atmospheric retrieval techniques (162) have enabled inverting the observed spectra to obtain detailed statistical estimates of atmospheric properties of exoplanets as a standard procedure. Such observations and inversion techniques are providing initial constraints on key atmospheric properties such as prominent molecular and atomic species (e.g. H_2O , CO , CH_4 , CO_2 ,

HCN, TiO, VO, Na, K), elemental ratios (e.g. O/H, C/O ratios), temperature profiles (including thermal inversions), clouds/hazes, circulation patterns, and exospheres.

The field is now moving beyond atmospheric characterisation of individual exoplanets towards comparative characterisation of ensembles of planets. Such constraints on atmospheric properties of exoplanets have advanced theories of a vast range of corresponding physicochemical processes in exoplanetary atmospheres, spanning chemical and radiative processes, atmospheric dynamics, atmospheric escape, and clouds/hazes. The derived chemical abundances are also being used to investigate constraints on planetary formation and evolutionary processes, which is one of the major current frontiers of the field (164, 140). At the same time, the first observations of chemical signatures in atmospheres of low-mass exoplanets, e.g. Neptunes and super-Earths, are becoming feasible, giving rise to the fledgling area of exogeology (265, 74, 277). Observations have also been attempted for transiting planets in the habitable zones of low-mass stars. While no such detection has yet been feasible the prospect of detecting an atmospheric signature of a rocky planet, potentially in the habitable zone, seems like a realisable dream.

Developments on the observational front have been led by both demonstrations of new detection methods as well as new instrumentation. The most remarkable of these successes have been in three directions corresponding to three detection methods. First, extensive high-precision transit spectroscopy with HST instruments from the UV to NIR have led to atmospheric characterisations in a large sample of transiting exoplanets. In particular, the HST WFC3 spectrograph in the NIR has made H₂O detections in exoplanetary atmospheres a routine matter today, with observed planets ranging from dozens of hot Jupiters to exo-Neptunes and even a super-Earth. This is remarkable considering that the H₂O abundances are not known for the giant planets in our own solar system owing to their low temperatures at which H₂O condenses. Besides HST, remarkable developments have also been made in transit spectroscopy using ground-based facilities. Such observations have led to detections of key species such as Na, K, and TiO, as well as of thermal emission from transiting exoplanets. Second, starting with the first detections a decade ago, direct imaging and spectroscopy of exoplanets is a highly successful technique today with nearly ten objects discovered and various dedicated ground-based surveys now underway. Finally, within this decade high-resolution Doppler spectroscopy in the near-infrared has made it possible to detect molecules in exoplanetary atmospheres, both transiting and non-transiting, by cross-correlation with template spectra. This technique has been very successful in detecting prominent molecules in several giant exoplanets orbiting bright stars. Beyond these broad developments, numerous advances have been made in various aspects of each detection method as will be discussed in this review. Concomitant advancements have also been made in atmospheric modelling, retrieval and theoretical studies.

The present review is an attempt to discuss the state-of-the-art of this exciting frontier. We will briefly review the recent advances in observational and theoretical methods in sections 2 and 3. We will then review the state-of-the-art, challenges, and future landscape of three frontier topics in the area. We will discuss advances in atmospheric characterisation of exoplanets in section 4, those on implications for planetary formation in section 5, and on habitability and biosignatures in section 6. We will conclude with a discussion on the landscape for the immediate future.

2. Observational Methods

Exoplanetary atmospheres have been observed using a wide range of methods that allow complementary constraints on their physicochemical properties. The methods fall into three broad categories: (a) Transit spectroscopy, (b) High-resolution Doppler spectroscopy, and (c) Direct imaging spectroscopy. While transit spectroscopy and Doppler spectroscopy are most conducive for atmospheric characterisation of close-in planets, direct imaging is more suited for planets at larger orbital separations. These various methods have been discussed in detail in the literature (227, 78, 167, 135, 26). The bulk properties of exoplanets whose atmospheres have been observed are shown in Fig. 2. Here we briefly outline each of these methods, their capabilities and limitations, and their future prospects.

2.1. Transit Spectroscopy

Transit spectroscopy has been the most successful avenue for their atmospheric characterisation of exoplanets to date, both by number of planets observed and the range of atmospheric constraints obtained (50, 63). This is due to both the larger number of planets detected using the transit method as well as the favourable geometry which makes it relatively easier for atmospheric observations compared to other methods. The transit method allows three configurations to observe a planet's atmosphere: (a) a 'transmission spectrum' when the planet transits in front of the host star, i.e. at primary eclipse (b) an emission spectrum as the planet passes behind the host star, i.e. at secondary eclipse, and (c) a phase curve as the planet orbits between the primary and secondary eclipses (127, 256). During the primary eclipse, the star light along the line of sight passes through the atmosphere at the day-night terminator of the planet. The resultant spectrum observed contains absorption features of the planetary atmosphere imprinted on the stellar spectrum. The difference between the in-transit and out-of-transit spectrum, normalised by the out-of-transit spectrum, yields the transmission spectrum. The transmission spectrum is effectively a measure of extinction due to the planetary atmosphere at its day-night terminator region. On the other hand, the secondary eclipse spectrum measures the emergent spectrum from the dayside atmosphere of the planet. Just prior to secondary eclipse the combined spectrum of both the star and the planetary dayside is observed. This combined spectrum, when subtracted by stellar spectrum, which is observed during secondary eclipse, yields the planetary spectrum. Finally, the phase curve provides a spectrum of the planet at different phases. Each of these configurations of transit spectroscopy provides different and complementary constraints on the atmospheric properties of a transiting planet. A panorama of state-of-the-art atmospheric spectra observed during primary and secondary eclipse is shown in Fig. 3.

A transmission spectrum is essentially a measure of the thickness of the atmosphere probed perpendicular to the line of sight as a function of wavelength. It provides constraints primarily on the chemical composition of the atmosphere at the day-night terminator region, along with the mean molecular weight and temperature through the scale height. Different spectral regions provide constraints on different chemical species. Prominent molecules expected in giant exoplanetary atmospheres such as H_2O , CO , CH_4 , CO_2 , HCN , TiO/VO , etc., have significant abundances and strong absorption features in the infrared and/or visible wavelengths making them detectable in transmission spectra (161, 188). Similarly, atomic features of alkali metals Na and K have strong absorption features in the visible (233, 244). On the other hand, transmission spectra are also excellent probes of scattering in atmospheres. Different sources of scattering such as Rayleigh scattering for small particles

HST: Hubble Space Telescope

Spitzer: Spitzer Space Telescope

JWST: James Webb Space Telescope

VLT: Very Large Telescope

GTC: Gran Telescopio Canarias

E-ELT: European Extremely Large Telescope

GMT: Giant Magellan Telescope

TMT: Thirty Meter Telescope

WFIRST: Wide Field Infrared Survey Telescope

HabEx: Habitable Exoplanet Observatory

LUVOIR: Large UV Optical Infrared Surveyor

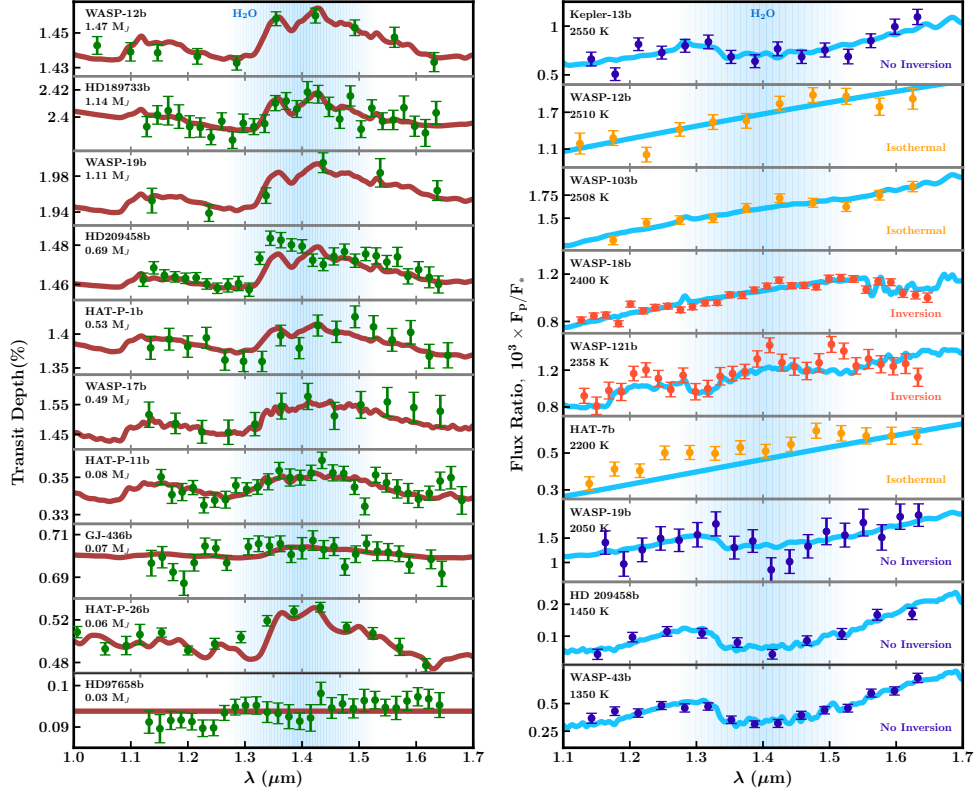


Figure 3: A panorama of primary (left) and secondary (right) eclipse spectra of transiting planets. Observations and error bars are obtained from the sources listed in table 1, while nominal models which fit these observations are shown by brown and blue lines. The spectral range affected by water absorption is shaded in blue and water features are present in many of the spectra. Left panel: Transmission spectra of planets arranged by ascending mass. Right panel: Secondary eclipse spectra arranged by ascending temperature and spanning a range of temperature structures from isotherms to profiles with thermal inversions.

versus Mie scattering for larger particles imprint distinct features in the optical transmission spectra and, hence, provide constraints on the presence of clouds/hazes in the atmospheres (274). Furthermore, the presence of high-altitude cloud decks in the atmosphere can also reduce the observable region of the atmosphere and mute the spectral features. Transmission spectra also provide unique probes of exoplanetary exospheres via detections of ionic species which have strong absorption features in the visible and UV (71). Recent studies have also investigated the impact of stellar heterogeneity on the spectral features observed in transmission spectra (178, 198). This is of particular significance to low-mass exoplanets orbiting M Dwarfs which are known to be active (211).

An emission spectrum, on the other hand, directly probes the temperature structure of the dayside atmosphere of the planet along with its chemical composition (132, 256). In principle, the full planetary spectrum observed at secondary eclipse contains both reflection and emission. Whereas reflection dominates at optical wavelengths, corresponding to the

peak of the stellar spectrum for FGK stars, the planetary emission typically dominates in the infrared owing to the lower temperatures. The planet-star flux contrast increases with wavelength as the star gets fainter and the planet gets brighter with wavelength. Thus, most of the dayside observations of exoplanetary atmospheres have been reported in the infrared. The observed spectrum probes the brightness temperature of the planet at different wavelengths, which effectively translates to measuring the temperatures at different depths in the atmosphere corresponding to the planetary photosphere at different wavelengths. The shapes and amplitudes of the spectral features are governed by both the chemical composition and temperature gradient in the atmosphere. For a given composition, a temperature profile with negative (positive) gradient, i.e., temperature decreasing (increasing) with altitude, leads to absorption (emission) features in the emergent spectrum. Therefore, emission spectra can provide powerful constraints on the presence of thermal inversions in exoplanetary atmospheres (discussed further in section 4.3). At the same time, for a given temperature profile the abundances of the chemical species affect the amplitude of the spectral feature. Thus, thermal emission spectra can provide strong constraints on both the composition as well as the temperature profile of the dayside atmosphere.

A phase curve measures the emergent spectrum of the planet, and hence its atmospheric properties, as a function of orbital phase (256). In addition to the constraints on composition and temperature, thermal phase curves provide direct constraints on the atmospheric dynamics and energy transport in the atmosphere. A thermal phase curve can also be deconstructed to provide the longitudinal temperature distribution in the planetary atmosphere as a function of depth. Thus, atmospheric observations of transiting exoplanets can provide constraints on a wide range of atmospheric processes as discussed above. The specific constraints on the various processes reported by existing observations are discussed in further detail in section 4.

2.2. High-resolution Doppler Spectroscopy

High-resolution Doppler spectroscopy of close-in planets has offered a powerful means to detect chemical species in atmospheres of close-in giant exoplanets, particularly hot Jupiters (251, 24). A detailed review of this area can be found in (26). This method involves phase-resolved high-resolution ($R \sim 10^5$) spectroscopy of the star-planet system to infer the Doppler motion of the planet using the planetary spectral lines. The combined spectra, observed using large ground-based facilities, contain contributions from both the stellar and planetary spectra along with telluric features due to the Earth's atmosphere. For a typical hot Jupiter the RV semi-amplitude of the planet is $1000\times$ larger than that of the star. Thus, the stellar and telluric features are relatively unchanged during the course of the observations, compared to the planetary spectral lines which undergo significant Doppler shifts. The stellar and telluric features in the data are removed using various detrending methods (37, 24, 47) which aim to remove the non-varying components leaving behind only the time-varying signal from the planet. In addition, some of the spectral regions with dense telluric contamination are masked out in the data. The resulting residual spectra after detrending are then cross-correlated with template planetary spectra containing the expected prominent molecules. For the matching planet spectrum the orbital motion of the planet can be reconstructed; in particular, the radial velocity semi-amplitude of the planet (K_p) and systemic velocity (V_{sys}) are constrained. A high significance peak in the K_p - V_{sys} plane constitutes a detection of the molecule present in the model template; typically a $5\text{-}\sigma$

signal-to-noise is considered a strong detection. The measured K_p , along with the known stellar velocity, also provides an independent constraint on the mass of the planet and the orbital inclination of the system (37). This method has been used to detect chemical species in a number of close-in hot Jupiters, e.g. molecular species CO (251, 37), H₂O (24), TiO (196), HCN (101, 47), and atomic species Fe, Ti, Ti+ (106). In addition to molecular detections, this technique has also led to constraints on the temperature profiles (196) and atmospheric wind speeds (251, 155).

This technique has also been used for atmospheric characterisation of directly-imaged planets at large orbital separations. This has been demonstrated by the CO detection in β Pic b (250) using a combination of high-contrast imaging and high resolution spectroscopy. Given their large orbital separations such planets are not expected to be tidally locked. Thus, their rotational velocity can be measured via the broadening of the spectral line. A rotational velocity of 25 km/s was measured for β Pic b using CO spectral features. The combination of high resolution spectroscopy and high contrast imaging enhances the sensitivities to flux contrasts beyond that achievable by either method. Furthermore, the combination of the cross-correlation technique with adaptive optics assisted integral-field spectrographs at medium resolution can also be used for detecting chemical species across the two-dimensional field of the image. Such ‘molecular mapping’ has been successfully demonstrated for high-significance detections of prominent molecular species such as H₂O and CO in directly imaged planets (107, 204).

The future of high-resolution Doppler spectroscopy offers both exciting avenues and commensurate challenges. With the advent of new high-resolution spectrographs, both on current and future facilities, it is natural to expect this as a promising pathway for molecular detections in exoplanetary atmospheres. Indeed, studies have suggested the feasibility of detecting molecules in the atmospheres of terrestrial-size planets with upcoming large facilities such as the E-ELT (248, 220). However, the detection significances of the species are arguably reliant on the metrics used for quantifying the signals and the detrending approaches. Latest studies are beginning to quantify these aspects (47). On another front, this technique on its own is less conducive for measuring the abundances of detected species; the signal is sensitive mainly to the line positions rather than the depths. However, the combination of this technique with low-resolution transit spectroscopy where possible may provide a solution in this regard (41). A viable future direction is one where new chemical species are first detected using this technique and the targets, if transiting, are then followed up with low-medium resolution transit spectroscopy for abundance estimates. The recent first inferences of HCN (101, 47) and atomic species (106) in hot Jupiters using this technique may be the first steps in this direction.

2.3. Direct Imaging

Spectroscopy of planets discovered via direct imaging offers another avenue to characterise exoplanetary atmospheres. In this method, the spectrum of the planet is obtained directly by nulling out the contribution from the star using a coronagraph. Though simple in principle, such observations are challenging given the stringent requirements on the sensitivity and inner-working angle (78). For example, a Jupiter analogue orbiting a sun-like star at 10 pc would require a planet-star flux contrast below 10^{-7} in the near-infrared at an inner working angle of 0.5''; the requirements are even more stringent in the optical. However, for young giant planets with high temperatures ($\gtrsim 1000$ K) at large orbital separations the

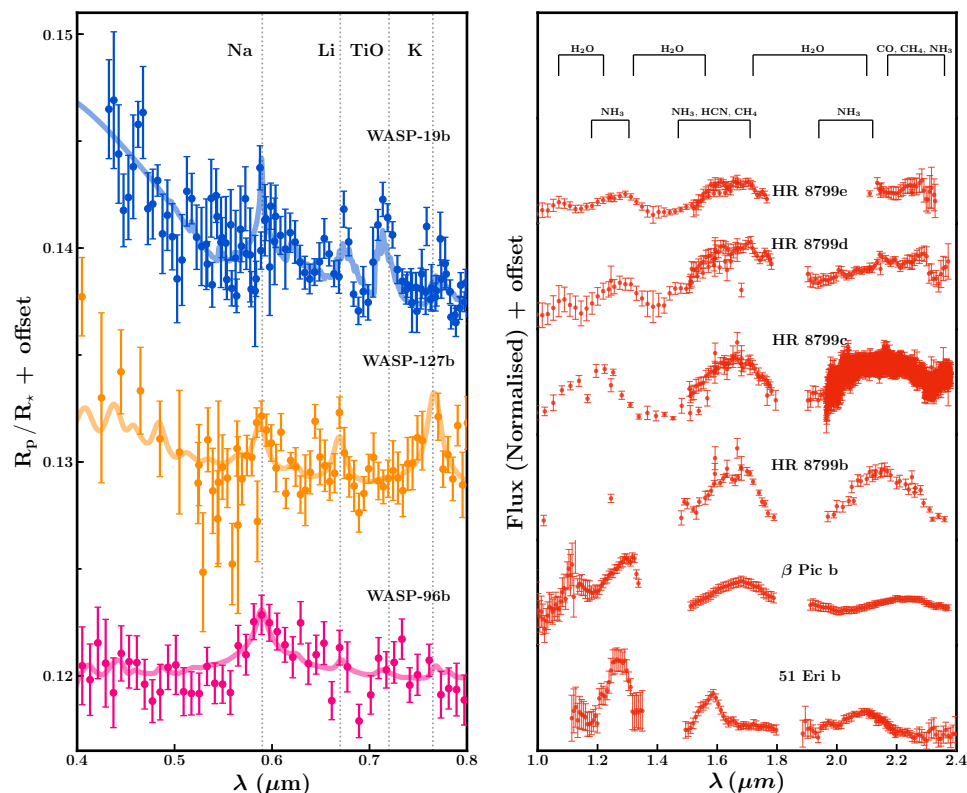


Figure 4: High-quality spectra of transiting (left) and directly-imaged (right) planets obtained with ground-based telescopes (sources are listed in table 1). For the spectra of transiting planets, nominal models which fit the data are also shown. The locations of spectral features arising from different chemical species are marked by dashed lines (left) and brackets (right). In both panels, the spectra are arbitrarily offset for clarity.

planet-star flux contrasts in the near-infrared approaches 10^{-4} making them detectable with current facilities. While the numbers of objects discovered via direct imaging are far fewer than transiting exoplanets, the spectra are typically of higher resolution and higher signal-to-noise ratio owing to the large-aperture ground-based facilities with adaptive optics used for this purpose. As such, the method has been successful in obtaining thermal emission spectra of several young giant exoplanets in the near-infrared.

The atmospheric properties that can be constrained with directly imaged spectra are similar to those for transiting exoplanets but with some important differences. A directly imaged spectrum is similar to an emission spectrum observed for transiting planets as discussed above and, hence, can provide important constraints on the temperature profile and composition of the atmosphere. However, unlike transiting planets the planetary radius and mass, and hence gravity, are not known a priori. This leads to degeneracies in accurately estimating the chemical compositions from the spectra because the shapes of the spectral features depend strongly on the gravity. Nevertheless, the higher resolution and signal-to-noise of the observed spectra make it possible to obtain robust detections of chemical

species in the atmospheres notwithstanding the challenges in obtaining specific quantitative constraints on the atmospheric properties. For example, high-confidence detections of H_2O , CO , and CH_4 have been reported for several directly imaged exoplanets in recent years (see table 1). Given the long orbital periods, the spectrum of a planet is typically obtained at a single orbital phase which is unknown, which restricts constraints on atmospheric dynamics. However, precise constraints on the globally-averaged compositions and temperature profiles at the observed phase are possible using atmospheric retrieval techniques. Additionally, given the low irradiation regime the atmospheric temperature profiles of directly imaged planets are expected to be markedly different from those of transiting exoplanets which tend to be highly irradiated. Initial constraints have been reported for a few objects while highlighting the challenges in resolving the various degeneracies. The specific constraints obtained for directly imaged planets are discussed in more detail in section 4.

The observational landscape of atmospheric characterisation of directly imaged planets is promising, limited only by sample size. Only ~ 10 directly imaged planets have been discovered since the first detections a decade ago (174, 118). The small current sample is arguably due to the paucity of giant exoplanets orbiting young stars at large orbital separations with flux contrasts above the detection thresholds of extant surveys. However, with new surveys increasingly aiming at higher sensitivities and inner working angles the sample size is likely to increase (93). On the other hand, current facilities have already provided spectacular spectra for some of these known planets, such as those in the HR 8799 system (e.g., 15, 129, 14, 174, 144, 143, 93) and 51 Eri b (159). The high-quality spectra are obtained thanks to high-contrast instruments on large-aperture ground-based telescopes operating in the near-infrared e.g., Keck (129), GPI on Gemini (93), SCExAO on Subaru (117), SPHERE on VLT (29). In the near future, the JWST will provide a high-stability platform for high-contrast imaging and spectroscopy in the near-mid infrared from space (21). In the late 2020s, NASA’s WFIRST mission is expected provide another space-based platform for direct imaging of giant exoplanets, particularly in the optical.

These facilities will be followed by the 25-40 m class telescopes in the next decade (mid-late 2020s), such as the E-ELT (39.3m), TMT (30m), and GMT (25.4 m), which will have unprecedented sensitivity for direct imaging. The E-ELT could in principle allow the detection of some atmospheric signatures of habitable-zone super-Earths and Earth-like planets orbiting the nearest stars (248). The high sensitivities required for such observations may be achieved by a combination of high dispersion spectroscopy and high contrast imaging, as has been demonstrated for the giant planet β Pic b with the VLT(250). While an exciting possibility, such observations will still be limited to spectral regions with relatively weaker telluric contamination and/or thermal background and, hence, limited molecular features in the NIR. On the other hand, space based facilities can provide the capabilities to surmount these limitations by offering broad spectral coverage (UV to IR) and very high sensitivities. Studies are underway for future large space-borne facilities in the 2030s focused on direct imaging and spectroscopy of habitable-zone exoplanets in search of potential biosignatures. Two such examples are HabEx (90) and LUVOIR (156). These mission concepts aim at very high contrast $\lesssim 10^{-10}$ direct imaging and spectroscopy over the UV-NIR spectral range using different flux suppression techniques and apertures, e.g. 4-m aperture for HabEx with coronagraph and starshade, and 8-12 m aperture for LUVOIR with a coronagraph.

SUMMARY POINTS

1. Advances in atmospheric spectroscopy have been made in three directions: (1) Transit spectroscopy, (2) Direct imaging, (3) High-resolution Doppler spectroscopy
2. Transit spectroscopy has been the most successful method: Nearly 100 exoplanets with atmospheres detected and over 20 giant exoplanets with high-precision multi-band spectra.
3. Transit spectroscopy allows observations of transmission spectra of day-night terminator, thermal emission spectra of dayside, and phase curves over the orbit.
4. Direct imaging provides high S/N thermal emission spectra at a single phase. Nearly 10 directly imaged planets known with high quality spectra available for several of them.
5. High-resolution Doppler spectroscopy allows detection of chemical signatures in planetary spectra Doppler shifted due to radial velocity of the planet. Chemical detections made in seven hot Jupiters.

3. Theoretical Advancements

Alongside observations, important advancements are being made in theoretical modelling and inverse methods to investigate exoplanetary atmospheres. These developments can be classified into three main categories: (1) Forward spectral modelling, (2) Retrieval methods (or inverse methods), and (3) Atmospheric theory. The primary observable in the characterisation of an exoplanetary atmosphere is an atmospheric spectrum. Firstly, even before an observation is made, a theoretical model spectrum is required to assess the feasibility of the observation and to predict the potential science return from the observation. This is the goal of forward spectral models which are used to compute spectra of exoplanetary atmospheres under specific assumptions about the atmospheric properties such as chemical abundances, chemical equilibrium, and/or radiative-convective equilibrium. Once the true spectrum of the planet is observed it may or may not match the spectrum predicted a priori. Thus, in practice, the observed spectrum is interpreted using atmospheric retrieval methods, or inverse methods, which involve deriving statistical constraints on the atmospheric properties of a planet from the spectral data using robust parameter estimation methods. The models used in retrievals, in this case, do not assume chemical/radiative equilibrium but rather use parametric atmospheric properties to be constrained by the data. Beyond spectral models and inverse methods, a wide range of studies use detailed theoretical models to investigate the various physical and chemical processes possible in exoplanetary atmospheres, e.g., non-equilibrium chemistry, atmospheric circulation, clouds/hazes, atmospheric escape, thermal inversions, and the like. In what follows, we review the key advancements in these areas.

3.1. Self-consistent Models

Self-consistent models are used to compute spectra of exoplanetary atmospheres for given assumptions about macroscopic parameters such as gravity, irradiation, and elemental abundances. Self-consistent models currently used in the field range from plane-parallel 1D models in chemical and radiative-convective equilibrium to full three-dimensional general circulation models (GCMs). Detailed reviews of such models can be found in various recent

works (167, 89, 110, 105, 173). Here we briefly summarise the state-of-the-art. While 1-D models are the most commonly used to predict and interpret individual spectra, GCMs are used extensively in interpreting phase-resolved spectra and photometric phase curves.

3.1.1. 1-D Equilibrium Models. A one-dimensional self-consistent model typically assumes an elemental composition (e.g., solar abundances) and equilibrium conditions such as thermochemical equilibrium and radiative-convective equilibrium, in a plane-parallel geometry. While the assumption of chemical equilibrium allows computation of the chemical abundances (i.e. atomic or molecular abundances) from the elemental abundances, the condition of radiative-convective equilibrium allows computation of the pressure-temperature (P - T) profile in the atmosphere consistent with the chemistry. The assumption of radiative-convective equilibrium is particularly relevant for modelling thermal emission spectra of exoplanets because the temperature gradients in the atmosphere play a critical role in the formation of emergent spectral features. The models compute radiative transfer through the atmosphere with the resultant chemical composition and P - T profile to generate the spectrum. A number of such models are available in the literature today with varying degrees of sophistication and flexibility. Early models in the field until recently were generally adapted from stellar spectral models and were computed on fixed grids of opacities, e.g., assuming solar elemental ratios with varying metallicities (231, 13, 81, 43). Newer models are now being custom-built for exoplanetary atmospheres and allow more flexible computations of spectra over a wider range of conditions to reflect the possible diversity of exoplanetary atmospheres (68, 182, 170, 89). These models span a wide range in chemical abundances (e.g. C/O ratios and metallicities), irradiation (from highly irradiated to non-irradiated), treatment of clouds/hazes, and strong visible absorbers such as TiO/VO that can cause thermal inversions. These models differ in their treatment of various aspects such as the radiative transfer, radiative versus convective energy transport, scattering, and opacities (110).

Central to all atmospheric models are the sources of opacity considered. The opacity is driven by the combination of chemical abundances and their absorption cross sections. While the chemical abundances depend on the modelling approach as discussed in this section (e.g. assuming chemical equilibrium, disequilibrium or parametric abundances), their absorption cross sections are fixed in the models. Therefore, the accuracy of model spectra are critically reliant on the accuracy of the absorption line lists from which the cross sections are derived. Such accurate line lists are required for a wide range of temperatures (~ 300 - 4000 K) and compositions possible in exoplanetary atmospheres, which extend beyond traditional applications. This need has been widely recognised in the field and substantial progress has been made in recent years towards accurate high-temperature line lists of numerous molecular species of importance for exoplanetary atmospheres (260). For example, recent line lists are now available for various species including H_2O (10, 221), CO (221, 147), CO_2 (221, 108, 109), CH_4 (284, 285), NH_3 (283), HCN (100, 11), collision-induced-absorption (215) and AlO (203). These developments have greatly improved the accuracies of such line lists as well as their applicability to exoplanetary atmospheres.

3.1.2. General Circulation Models. GCMs solve the full three-dimensional structure of the atmosphere given the planetary bulk parameters and irradiation field. These models compute the chemical, thermal, dynamical and radiative properties of the atmosphere in extensive detail. Starting with the first coupled GCMs, with both radiative

and dynamical treatment, about a decade ago (239) a number of GCMs are prevalent in the field today with varied levels of complexity. The latest GCMs span a wide range of irradiation conditions, from highly irradiated planets to non-irradiated isolated sub-stellar objects, and orbital parameters (e.g., eccentricities, obliquities), and masses (e.g. 238, 202, 122, 145, 212, 153, 67, 36, 66, 180). These models have been used to explain phase-resolved spectra and thermal phase curves of hot Jupiters (239, 122, 153) and to explore various physical processes in detail (239, 202, 200, 67). One of the key successes of GCMs is the predictions of strong equatorial jets in irradiated hot Jupiters that can lead to shifting of the hot spot in the dayside atmospheres away from the sub-stellar point (240). This effect, predicted nearly a decade ago (240, 239), has been substantiated by other GCMs in the literature (e.g. 213, 241, 67) as well as by numerous observations of hot Jupiters as discussed in section 4.4. These models have also recently considered the effect of latent heat on the atmospheric properties through condensate formation and chemical recombination (259, 22). GCM models also show a trend of day-night temperature contrasts in hot Jupiters increasing with equilibrium temperatures (128), consistent with observations and empirical studies (128, 224). Atmospheres of highly irradiated and tidally locked hot Jupiters have also been predicted to contain larger planetary-scale bands compared to those of weakly irradiated and faster rotating planets like the solar-system giant planets.

Recent studies are moving beyond hot Jupiter atmospheres with solar abundances. Early GCMs typically assumed solar elemental abundances for hot Jupiters, from which the molecular compositions were calculated assuming thermochemical equilibrium. Recent GCMs are now being used to explore the effect of chemical composition on the dynamical processes in the atmospheres. New GCMs are capable of simultaneously modelling the dynamics coupled with chemistry, radiative transfer, and clouds (202, 200, 145, 67, 153). GCMs are now also exploring lower-mass planets which are within the reach of current and forthcoming observational facilities. In particular, several studies have explored the effect of metallicities in sub-Jovian mass planets such as Neptunes and super-Earths which are not necessarily hydrogen-rich (146, 287, 67). Such studies have sought to model and explain observations of thermal phase curves of super-Earths, e.g. 55 Cancri e, that are already feasible with current facilities (65).

3.2. Atmospheric Retrieval

Atmospheric retrieval refers to deriving the atmospheric properties of a planet from its observed spectrum. The canonical retrieval method comprises a parametric forward model of an exoplanetary atmosphere coupled with a parameter estimation algorithm to estimate the model parameters given a spectral dataset. The free parameters in the model include the dominant chemical species with strong features in the observed spectral bandpass, the temperature profile, and the macroscopic clouds/haze parameters, e.g. the location in the atmosphere, spatial extent and opacity, besides any other free parameters relevant to the spectrum at hand. Starting with the first retrieval codes a decade ago, a number of codes are currently available in the field with applicability over the wide range of observations possible. A recent review of existing retrieval codes and capabilities in the field can be found in (162). The latest developments in retrievals include incorporation of non-equilibrium phenomena at varying levels of complexity, such as different prescriptions for clouds/hazes (e.g. 16, 151, 143, 157), deviations from radiative-convective equilibrium (89), and benchmarking with three-dimensional circulation models (27). On the other hand, state-of-the-art codes use a

wide range of parameter estimation methods spanning Markov chain Monte Carlo methods (27), optimal estimation gradient-descent algorithms (16), nested sampling algorithms (e.g., 23), and machine learning algorithms (279). In recent years, state-of-the-art retrieval codes have allowed detailed constraints on the chemical compositions, temperature profiles, and properties of clouds/hazes in a number of exoplanets, both transiting and directly-imaged (162).

3.3. Disequilibrium Models

Planetary atmospheres are seldom in equilibrium in entirety. Various processes can drive an atmosphere out of chemical, radiative, and thermal equilibria. These processes, illustrated in Fig. 1, include vertical mixing and photochemical processes, circulation, clouds/hazes, atmospheric escape, etc., one or more of which dominate in any observed region of the atmosphere. The ultimate model atmosphere would include all these processes simultaneously over the entire atmosphere, troposphere to exosphere. However, such a comprehensive unified model for exoplanetary atmospheres is impractical at present. Additionally, exoplanetary spectra are typically observed in a limited spectral band at a time constraining some atmospheric properties/processes but with almost no constraints on other aspects. Therefore, a realisable and useful approach currently is to explore each individual processes in detail while allowing for appropriate boundary conditions or simplified prescriptions to represent the interplay with other processes. This has been the approach in the field. Theoretical studies in recent years have explored each of the aforementioned processes in exoplanetary atmospheres in varied detail as summarised below. Here we only discuss briefly developments in atmospheric chemistry and clouds/hazes. A comprehensive review of theoretical developments in atmospheric escape processes can be found in (199).

3.3.1. Atmospheric Chemistry. State-of-the-art models of atmospheric chemistry in exoplanets span a wide range in complexity. While the most extensive chemical networks are considered in 1-D models of non-equilibrium chemistry (e.g., 188, 267, 263), recent studies are beginning to combine chemical codes in 3-D General Circulation Models (287, 67). A recent review of such models can be found in (163). The chemistry in a planetary atmosphere is a strong function of the macroscopic parameters such as the elemental abundances (e.g., of H, O, C), stellar irradiation, gravity, and mean molecular mass. In particular, there is a clear dichotomy between primary atmospheres which are expected to be dominated by H_2/He as in the giant planets and secondary atmospheres that are expected to be dominated by heavier molecules such as H_2O , CO_2 , or N_2 , as in the terrestrial planets. Given the bulk properties, the key processes governing the chemistry in a planetary atmosphere include chemical equilibrium, mixing processes, photochemistry, and chemical diffusion. Each of these processes dominate in a particular region of the atmosphere (see e.g. Fig. 1), depending primarily on the incident irradiation and, hence, the temperature profile in the atmosphere. Chemical equilibrium dominates in the deep atmosphere, typically for $P \gtrsim 1$ bar where the high density and temperature lead to fast thermochemical reactions. At the other extreme, photochemical reactions dominate in the upper atmosphere typically for $P \lesssim 10^{-3}$ bar where the incident UV/optical flux is high and the densities are too low for thermochemical reactions to dominate. In the intermediate regions between these two extremes dynamical processes, such as vertical mixing, dominate the chemical composition of the atmosphere. Recent studies have investigated the critical dependence of all aspects

of chemistry in exoplanetary atmospheres on the macroscopic parameters, e.g. the level of stellar irradiation, metallicity, and C/O ratio (188, 186, 268, 287, 68).

3.3.2. Clouds/Hazes. A critical factor in the understanding of exoplanetary atmospheres is the prevalence of clouds/hazes which can affect both the atmospheric processes and the observed spectra. Numerous theoretical studies have posited the ubiquity of clouds in atmospheres at all temperatures. Detailed reviews on models of clouds/hazes in exoplanetary and sub-stellar atmospheres can be found in (173, 163). While the clouds in solar system planets are composed of volatile-rich condensates (e.g. H_2O , NH_3 , hydrocarbons, etc.), those in hot exoplanets can span a wide range of refractory-rich compositions. Models of exoplanetary atmospheres over the years have explored the effects of a wide range of clouds/hazes on exoplanetary spectra, both for irradiated planets observed via transit as well as directly-imaged planets. Recent developments on the understanding of clouds/hazes in exoplanetary atmospheres have proceeded in two directions. On one hand, there have been major efforts on self-consistent cloud modelling at varying levels of detail - from one-dimensional self-consistent models (e.g., 172, 182, 68) to three dimensional cloud models (202, 67), as well as detailed studies of clouds microphysics (103). On the other hand, various studies have explored the range of cloud compositions observable with existing and upcoming facilities (176, 274, 205), spanning from refractory clouds in high-temperature atmospheres to volatile clouds in low-temperature atmospheres.

SUMMARY POINTS

1. Advancements in atmospheric modelling of exoplanets have been made in various directions, spanning 1-D to 3-D self-consistent models, atmospheric retrievals, and models of various disequilibrium processes.
2. Self-consistent spectral models are used to compute the spectra of exoplanetary atmospheres given the macroscopic parameters (e.g., gravity, irradiation, elemental abundances) and assumptions of chemical and/or radiative-convective equilibrium.
3. Forward models range from one-dimensional equilibrium models to three-dimensional general circulation models (GCM).
4. Atmospheric retrievals, or inverse modelling, involves using parametric models and parameter estimation methods to derive atmospheric properties from observed spectra. Derived properties include chemical compositions, temperature profiles, cloud/hazes, and deviations from chemical or radiative equilibrium.
5. Disequilibrium models include detailed modelling of various processes that drive atmospheres out of chemical and/or radiative equilibria, e.g., kinetic processes, photochemistry, clouds/hazes, and atmospheric escape.

4. Atmospheric Characterisation of Exoplanets

The combination of state-of-the-art spectroscopic observations and theoretical modelling and retrieval techniques have led to detailed constraints on a wide range of atmospheric properties in numerous exoplanets. Atmospheres of nearly one hundred exoplanets have now been observed in at least two photometric bandpasses, low resolution spectra have been obtained for nearly 40 planets, and medium-high resolution spectra obtained for nearly ten

exoplanets. This is a revolutionary development from a decade ago when barely 25 exoplanets were known to transit and the first directly imaged planets were being discovered. These new observations have led to unprecedented constraints on chemical compositions, temperature profiles, clouds/hazes, atmospheric dynamics, and atmospheric escape, for numerous exoplanets. Here we highlight some of the most recent advances in the characterisation of exoplanetary atmospheres.

4.1. Chemical Compositions

The wide spectral range of exoplanetary spectra observed has enabled robust detections of several key chemical species in their atmospheres, as shown in Table 1. As alluded to in section 1, atomic and ionic species have strong absorption in the UV and visible due to their electronic transitions. On the other hand, prominent molecular species of volatile elements such as H_2O , CO , CH_4 , etc. show strong absorption in the infrared due to their rovibrational transitions, though heavier molecules such as TiO and VO also show strong absorption in the visible. The combination of spectroscopic measurements at different wavelengths and different observing techniques has led to a range of chemical compositions observed in diverse planets. The different chemical species detected probe different regions in the planetary atmosphere, as shown in Fig. 1. The strong UV and visible absorbers such as the atomic species probe the upper regions of the atmospheres where photochemistry is most active, with the ionic species probing the exospheres. On the other hand, the molecular species probe the infrared photosphere between ~ 1 mbar - 1 bar. Table 1 shows the chemical species detected using each observing method. While transmission spectra have been used to probe atmospheres over the entire spectral range from UV - infrared, the emission spectra of both transiting planets and directly imaged planets have been observed predominantly in the infrared where the thermal emission peaks.

Table 1: Chemical detections in exoplanetary atmospheres with different observing techniques.

Transmission Spectra (Primary Eclipse)	
Chemical Species	Planet (References)
H_2O	HD 189733b (178), HD 209458b (63), WASP-12b (133), WASP-17b (171), WASP-19b (112), WASP-39b (276), WASP-43b (132), WASP-52b (266), WASP-63b (123), WASP-69b (266), WASP-76b (266), WASP-121b (77), HAT-P-1b (275), HAT-P-11b (84), HAT-P-18b (266), HAT-P-26b (277), HAT-P-32b (60), HAT-P-41b (266), XO-1b (63)
Na	HD 189733b (214), HD 209458b (50), WASP-17b (244), WASP-39b (194), WASP-52b (52), WASP-69b (48), WASP-96b (193), WASP-127b (53), HAT-P-1b (195), XO-2b (245)

Continued on next page

Table 1 – *Continued from previous page*

Chemical Species	Planet (References)
K	WASP-6b (192), WASP-31b (247), WASP-39b (244), WASP-127b (53), HAT-P-12b (244), XO-2b (243), HD 80606b (55)
TiO	WASP-19b (232)
AlO	WASP-33b (273)
H	HD 189733b (116, 33), HD 209458b (272, 116), GJ 436b (71)
He	WASP-107b (253)
C	HD 209458b (270)
O	HD 209458b (270)
Li	WASP-127b (53)
Ca	HD 209458b (8)
Sc	HD 209458b (8)
Mg	WASP-107b (271), WASP-12b (83)
Si	HD 209458b (223)

Emission Spectra (Secondary Eclipse)

H ₂ O	WASP-43b (132), HD 209458b (151), HD 189733b (59), WASP-121b (76), Kepler-13Ab (20), WASP-33b (102)
CO	WASP-18b (236)
VO	WASP-121b (76)
TiO	WASP-33b (102)
HCN	HD 209458b (101)

Continued on next page

Table 1 – *Continued from previous page*

Chemical Species	Planet (References)
High-resolution Doppler Spectroscopy	
H ₂ O	51 Peg b (25), HD 179949 b (39), HD 189733b (24), HD 209458b (101)
CO	τ Bootis b (37), HD 209458b (251), 51 Peg b (38), HD 179949 b (39), HD 189733b (219, 40)
TiO	WASP-33b (196)
HCN	HD 209458b (101), HD 189733b (47)
Ti, Fe, Ti+	KELT-9b (106)
Direct Imaging	
H ₂ O	HR 8799b (144), HR 8799c (129), HR 8799d (143), HR 8799e (143), κ And b (262), 51 Eri b (222), Gl 570D (152), HD 3651B (152), β Pic (54), ULAS 1416 (149)
CH ₄	HR 8799b (14), 51 Eri b (222), GJ 504 (114), GJ 758 B (115), Gl 570D (152), HD 3651B (152), ULAS 1416 (149)
NH ₃	Gl 570D (152), HD 3651B (152), ULAS 1416 (149)
CO	HR 8799b (144), HR 8799c (129)

4.1.1. Atomic and Ionic Species. The first chemical detections in exoplanetary atmospheres were of atomic and ionic species observed using HST transmission spectra in the optical and UV (50, 272). Nearly 20 chemical species have now been detected in exoplanetary atmospheres as shown in table 1. In recent years, chemical species have been detected both from space, using HST, as well as large ground-based telescopes. Foremost among these are detections of the alkali species Na and K, one or both of which have now been detected in over a dozen transiting hot Jupiters. The Na doublet has peaks near 576.8 nm whereas K peaks near 778.8 nm. Many of the Na and K detections have been made using the HST STIS spectrograph in the visible (e.g., 244). Recently, He was also detected in the atmosphere of a giant exoplanet using HST at 1083 nm (253). A major development in recent years has been the ability to detect these species routinely and robustly using ground-based facilities. While the first ground-based Na/K detections were already made a decade ago (e.g., 214), recent observations are demonstrating nearly space-quality spectra from large ground-based

telescopes such as VLT and GTC (193, 53). Besides Na and K, the first potential inference of Li was also made from the ground recently using the GTC (53). The above detections were made using medium-resolution spectra from space and the ground. On the other hand, atomic species have also been detected using very high-resolution spectroscopy of transiting planets, e.g. Na and K in the hot Jupiter HD 189733b (282) and Ti and Fe in the ultra hot Jupiter KELT-9b (106).

In addition, several atomic and ionic species have also been discovered using transmission spectra in the UV with HST. These are elements in the exosphere which originated from photodissociation of molecules in the lower atmosphere followed by interactions with higher energy UV photons in the upper atmosphere. Several of the detections are of Lyman alpha absorption of exospheric hydrogen (H) at 121.6 nm using the HST STIS instrument (272, 71). On the other hand, some heavier elements such as C, O, and Mg, have also been detected in the NUV (270, 83). Overall, such exospheric elements have been discovered in nearly ten giant exoplanets, mostly for hot Jupiters but also including a hot Neptune (136, 71). Efforts to detect exospheric elements in super-Earths have not yet resulted in detections but have provided important upper limits on the composition of the lower atmosphere. For example, the non-detection of H in the super-Earth 55 Cancri e rules out a hydrogen-rich atmosphere in the planet and places an upper-limit on the possible amount of H₂O in the atmosphere (70).

4.1.2. Molecular Species. The advent of high-sensitivity infrared spectrographs has made it feasible to robustly detect molecules in exoplanetary atmospheres. The most important molecules in planetary atmospheres are those containing the prominent elements after H and He, namely O, C, and N. Theoretical studies have long predicted that key volatile molecules such as H₂O, CH₄, CO, HCN, CO₂ should be present in H₂-rich atmospheres at high temperatures, e.g. of hot Jupiters, depending on the metallicity, temperature, and C/O ratios (e.g., 46, 189, 161). However, the search for these molecules in exoplanetary atmospheres is usually limited by the spectral range and sensitivities of available instruments. A decade ago only a handful of molecular inferences were reported with very low resolution spectro-photometric data which have since been revised in subsequent analyses. Here we focus on the current state-of-the-art molecular detections.

A major development in this area occurred in the last few years with the advent of the HST Wide Field Camera 3 (WFC3) (177) which allowed high-precision near-infrared spectroscopy of transiting exoplanets (63). The spectral range of the HST WFC3 G141 grism of 1.1-1.7 μm contains strong spectral bands of key volatile species such as H₂O, CH₄, NH₃, and HCN, making it a prime instrument for molecular spectroscopy of exoplanetary atmospheres. Among these species, H₂O has the strongest features in this band and is also predicted to be the most abundant oxygen-bearing species, besides CO, in high temperature atmospheres (161, 188). In the last five years, spectra of nearly 40 transiting exoplanets have been observed with HST WFC3 and robust detections of H₂O have been reported in over ten transiting exoplanets (63, 178, 132, 244, 266). Most of the detections were made for gas giants, though H₂O has also been detected in a few exo-Neptunes (85, 277). Beyond H₂O, initial indications have also been suggested for HCN and NH₃ using HST WFC3 transit spectroscopy (158, 123). In addition, signs of TiO, VO, and AlO have also been reported using HST and/or large ground-based facilities (102, 76, 232, 273).

Complementary to transmission spectra, molecular detections have also been reported using thermal emission spectra of transiting exoplanets. Such spectra using HST WFC3

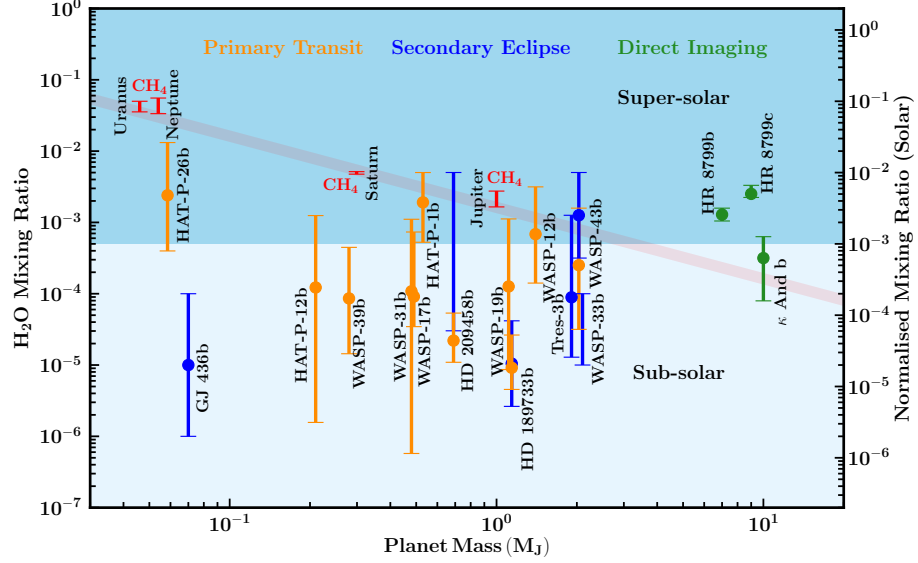


Figure 5: Atmospheric H_2O abundances for exoplanets in the literature. The abundances shown here are those with uncertainties smaller than 2 dex. The methods used in each case are denoted by colour; primary transit (orange), secondary eclipse (blue) and direct imaging (green). The regions of sub-solar and super-solar abundances are shown in light and dark blue, respectively. Methane abundances of the Solar System planets are shown in red (since their water abundances are not known), and a power-law fit for these measurements is shown by the red line. The methane abundances are obtained from the following sources: Jupiter and Saturn (9, 281, 79), Neptune (121), and Uranus (254). The exoplanet H_2O abundances are from various works: HD 209458b (206, 151), HD 189733b (206, 278), WASP-12b (206), WASP-43b (132), WASP-33b (102), TrES-3 (148), GJ 436b (187), HAT-P-26b (277), WASP-39b (206), HR 8799 planets (143), κ And b (262).

have led to detections of H_2O in the dayside of several hot Jupiters (e.g., 59, 132, 151) as well as high-temperature molecules such as TiO (102) and VO (76). At a lower resolution, inferences of CO have been reported in some hot Jupiters based on infrared photometry using Spitzer in the 3.6 and 4.5 μm IRAC bands (e.g., 236).

Beyond transit spectroscopy, more molecular detections at high confidence have now been made through direct imaging and Doppler spectroscopy. High resolution Doppler spectroscopy has led to detections of various molecules including CO (251, 37), H_2O (24), TiO (196), and HCN (101) in hot Jupiters. At the same time, spectroscopy of directly imaged planets have led to detections of CO (129), H_2O (14, 129, 262, 222), and CH_4 (14, 222, 114) in the atmospheres of several planets. Typically, current data quality for directly imaged objects is significantly better compared to transit planets (129, 262, 160). On the other hand, comparative characterisation of directly imaged planets are limited by the much smaller number of objects known, compared to transiting planets, and the lack of

prior knowledge about the masses, radii, and gravity.

4.1.3. Chemical Abundances. Beyond detections of chemical species, the high quality spectra have also led to constraints on the atmospheric chemical abundances using detailed retrieval methods. A recent review of retrieval methods and abundance constraints can be found in (162). Here, we briefly highlight the state-of-the-art abundance constraints. Despite the detections of a wide range of chemical species in tens of exoplanets, robust abundance constraints are available for only a subset of those planets due to the challenges in retrieving abundances from observed spectra. Firstly, constraints on chemical abundances are presently possible using both transit spectroscopy (transmission and emission) and thermal emission spectra of directly imaged planets. Currently, high resolution Doppler spectroscopy on its own is not as sensitive to abundance determinations (24, 41). Secondly, even within transit spectroscopy reliable estimations of chemical abundances require a wide spectral coverage and very high precision observations. In particular, in transmission spectroscopy robust spectra across the visible to near-infrared are required to break the degeneracies between the chemical abundances and the presence of clouds/hazes in the atmosphere. In emission spectra, high-precision observations are required to break the degeneracies between abundances and temperature profiles.

Currently, the most stringent constraints on chemical abundances have been possible for H₂O. Observations of transit spectroscopy in the HST WFC3 band at 1.1-1.7 μm span a strong H₂O feature near 1.4 μm . Furthermore, the HST STIS band in the optical provides important constraints on clouds/hazes in the atmosphere, thereby resolving degeneracies with composition. Such observations have been used to retrieve H₂O abundances for over ten transiting hot Jupiters and Neptunes (16, 206, 277). Similarly, emission spectra in the near-infrared with HST WFC3 have led to constraints on H₂O abundances in the dayside atmospheres of several hot Jupiters (132, 151). In addition to this, ground-based spectra of directly imaged planets have also provided initial constraints on H₂O abundances (262, 143).

The estimated H₂O abundances in transiting and directly-imaged planets are shown in Fig. 5. Most of the H₂O abundance estimates are derived from transmission spectra obtained using HST STIS and WFC3 instruments spanning the optical to near-infrared instruments. While the infrared WFC3 spectral range contains the H₂O feature the optical range is necessary to resolve degeneracies with clouds/hazes. Overall, the abundance estimates from transmission spectra across all transiting hot Jupiters known to date are consistent with sub-solar H₂O abundances. Whether such low abundances are due to low metallicities in the atmosphere or high C/O ratios is currently unknown. A detailed discussion on these aspects can be found in (162). The handful of constraints obtained from emission spectra of a few transiting exoplanets are consistent with both sub-solar and super-solar H₂O abundances given their larger uncertainties. On the other hand, directly imaged planets with their superior spectral quality have led to much more precise abundance estimates and indicate super-solar H₂O abundances (262, 143).

4.2. Clouds/Hazes

Inferences of clouds/hazes in exoplanetary atmospheres have been made using varied techniques and instruments. The effect of clouds/hazes on exoplanetary transmission spectra is evident through (a) subdued spectral features of prominent chemical species (63), and (b) slopes in optical spectra that are deviant from gaseous Rayleigh scattering (209). In addi-

tion, the effects of clouds have also been inferred through optical phase curves of transiting exoplanets (64, 242, 91, 200) as well as a few reflection spectra (75, 175). At the same time, clouds have also been inferred in directly imaged planets through the modulation of their spectral features in the infrared (173). A survey of observational inferences of clouds/hazes until a few years ago can be found in (163). Here, we outline some key trends.

One of the most surprising findings from the large ensemble of exoplanetary transmission spectra observed is the consistently low spectral amplitudes of H_2O absorption features. In the tens of transmission spectra observed to date, for exoplanets over a wide range of masses and temperatures from cool super-Earths to ultra hot Jupiters, every single one has a H_2O feature that is below two scale heights (86, 255, 58). This is in stark contrast to expectations, for which a saturated spectral feature in a transmission spectrum is expected to have an amplitude of ~ 5 -10 scale heights. The low spectral amplitudes may indicate either lower H_2O abundances than assumed in equilibrium models (166), the presence of high-altitude clouds obscuring part of the atmosphere (80, 63), or a high mean molecular weight (150). One way to break the degeneracy is through observations in the optical which, as discussed above, can constrain the scattering mechanisms and hence the presence of clouds/hazes.

A recent survey of transmission spectra (244) spanning the optical and infrared range provided important constraints on both the properties of clouds/hazes as well as the H_2O abundances in ten hot Jupiters. Initial inferences of the data using forward equilibrium models reported the possibility of clouds with no evidence for H_2O depletion (244). However, as discussed in previous section, subsequent studies using atmospheric retrieval methods showed evidence for depleted H_2O abundances in most of the planets in the sample, along with varied levels of clouds/hazes (16, 206). These studies show a diverse range of cloud properties, including the optical slopes, cloud fractions, and cloud-top pressures. Most importantly, these studies show the critical role of the optical range in transmission spectra for constraining both the clouds/hazes as well as the composition. Indeed, other studies that used only near-infrared HST WFC3 spectra show significantly weaker constraints on the cloud parameters and/or the H_2O abundances (266). On the other hand, the low-temperature super-Earths and Neptunes have mostly shown flat spectra in the WFC3 band-pass (131, 124) with a few exceptions (85, 277), which indicate the predominance of clouds in low-temperature atmospheres.

The potential pervasiveness of clouds/hazes has motivated various studies to devise empirical metrics to quantify the cloudiness in exoplanetary atmospheres. Some studies suggest a metric based on the amplitude of the H_2O feature relative to the continuum in adjacent wavelengths (244, 255), or the amplitude of the Na/K line centre relative to their adjacent continua (104). Using known transmission spectra these studies find an intuitive anti-correlation between irradiation and cloud levels, i.e., the likelihood of clouds in atmospheres of hot Jupiters decreases with increasing equilibrium temperature.

4.3. Temperature Structures

Temperature profiles of planetary atmospheres provide important insights into radiative processes and their interplay with chemical and dynamical processes. Measurements of pressure-temperature (P-T) profiles in exoplanetary atmospheres are obtained primarily from thermal emission spectra. An emission spectrum probes the brightness temperature in the atmosphere as a function of the wavelength and, hence, the pressure or altitude corresponding to the photosphere at that wavelength. In principle, transmission spectra of

transiting planets also provide some constraints on the temperature at the day-night terminator region of the atmosphere but the constraints are relatively weak. This is because there is almost no information in a transmission spectrum about emission from the planet, and the constraint on temperature is primarily through the atmospheric scale height which governs the amplitude of the absorption feature. Therefore, the most stringent constraints on P-T profiles in exoplanetary atmospheres have been obtained for dayside thermal emission spectra of transiting hot Jupiters. A detailed review of observational inferences of atmospheric P-T profiles in exoplanets and their theoretical implications have been discussed in several recent works (167, 163, 162). Here we focus on the latest developments in this area and future directions.

Recently, new directions are emerging in our understanding of P-T profiles in exoplanets. Originally, constraints on P-T profiles were obtained using only two or more channels of broadband photometry (e.g., at $3.6\ \mu\text{m}$ and $4.5\ \mu\text{m}$). However, current inferences are based on HST WFC3 spectra in the near-infrared in the $1.1\text{--}1.7\ \mu\text{m}$ band along with Spitzer photometry, making the inferences much more robust. Broadly, three classes of P-T profiles have been robustly measured in hot Jupiters: (1) P-T profiles with no thermal inversions, (2) P-T profiles with thermal inversions, and (3) isothermal profiles. Almost all the hot Jupiters observed to date with equilibrium temperatures below $\sim 2000\ \text{K}$ show temperature profiles clearly decreasing outward, i.e., with no thermal inversions. More irradiated hot Jupiters show a greater diversity of P-T profiles. Most of these extremely irradiated planets show P-T profiles consistent with isothermal profiles. A handful of these planets also show P-T profiles with no thermal inversions, i.e. with temperatures decreasing outward. And finally, after over a decade of searches, three ultra-hot Jupiters ($T_{\text{eq}} \gtrsim 2500\ \text{K}$) have been found with detections of thermal inversions in their dayside atmospheres: WASP-18b (236, 6), WASP-121b (76), and WASP-33b (102). In summary, while it is now evident that very high temperatures ($\gtrsim 2500\ \text{K}$) are a necessary condition for thermal inversions, it is not a sufficient condition since some ultra-hot Jupiters show no signs of thermal inversions (20).

Observational constraints are beginning to provide new insights into the conditions responsible for thermal inversions in irradiated hot Jupiters. Given that thermal inversions are being seen only in the most highly irradiated planets, the so-called ‘ultra-hot Jupiters’, there is support to the original prediction of TiO/VO being the candidate UV/visible absorbers (111, 81) that are causing the inversions. In particular, observations of both WASP-33b and WASP-121b have indicated emission features of TiO (102, 196) and VO (76), respectively. While WASP-18b has not revealed any spectral signatures of TiO/VO, (6) suggested H^- opacity as the putative cause. Another aspect of the ultra-hot Jupiters with inversions is that none of the spectra show evidence for strong H_2O features but do show evidence for CO features. The under-abundant H_2O is evident from the muted H_2O feature in the HST WFC3 band at $1.4\ \mu\text{m}$ whereas the significant CO is evident from the excess emission in the Spitzer $4.5\ \mu\text{m}$ band. These ultra-hot Jupiters have now become the new testing ground for hypotheses on thermal inversions.

Two competing hypotheses have been put forth to explain the thermal inversions and the lack of strong H_2O features from infrared spectra of ultra hot Jupiters. One possibility is a super-solar C/O ratio ($\gtrsim 1$) in these atmospheres which can cause low H_2O abundance and high CO abundance (161, 188, 236). An alternate explanation is that thermal dissociation of H_2O at these high temperatures is responsible for depleted H_2O , while molecules such as CO and TiO are relatively more stable (6, 201, 154). The thermal dissociation is also accompanied by H^- production. This hypothesis can be tested if H^- can be retrieved from

observed spectra. Currently, inferences of H^- (e.g., in WASP-18b) are based on grids of equilibrium models explored to match the data rather than retrieving statistical constraints on the H^- abundance from the data (6). Furthermore, another ultra-hot Jupiter, Kepler-13Ab, which is hotter than WASP-18b, shows a strong H_2O feature in absorption indicating the presence of H_2O and lack of thermal inversion. This latter anomaly has been explained as due to the high mass and gravity of Kepler-13Ab which enhance cold-trap processes removing inversion-causing species (20).

Beyond thermal inversions, temperature profiles also provide important constraints on other atmospheric processes. As discussed above, most of the planets observed to date show temperature profiles with no thermal inversions. For irradiated planets, this implies a lack of strong UV/visible absorbers in their atmospheres. On the other hand, for non-irradiated planets such as those observed with direct imaging, the P-T profiles are naturally expected to be devoid of thermal inversions due to the lack of incoming radiation. This is consistent with observed emergent spectra of directly-imaged planets all of which show only absorption features (14, 129, 160, 29) and the retrieved P-T profiles also show profiles with no inversions (143).

4.4. Atmospheric Dynamics

New observations are leading to detailed constraints on atmospheric circulation patterns in hot Jupiters. Constraints on atmospheric dynamics have been obtained with a variety of observations, such as (1) thermal phase curves (286), (2) measurements of wind speeds (251), (3) eclipse mapping (61). While thermal phase curves in individual photometric bandpasses have been obtained for a large number of exoplanets, full phase resolved spectra have also been obtained (256, 134) allowing for detailed retrievals of composition and vertical temperature profiles as a function of orbital phase, as well as the brightness temperature maps as a function of pressure or depth in the atmosphere. The phase curves also provide constraints on day-night temperature contrasts and the location of the day-side hot spot with respect to the sub-stellar point. On the other hand, high-resolution spectroscopy of key species such as CO and Na are providing direct constraints on the wind speeds in the atmospheres of hot Jupiters (251, 155).

Observations of thermal phase curves of exoplanets are commonplace today. Phase curves have been observed with a number of facilities, including Spitzer, HST, and Kepler. Most of the observations have been conducted for hot Jupiters, however recently a thermal phase curve was reported for the transiting super-Earth 55 Cancri e (65). The ensemble of observations has provided two main insights into atmospheric dynamics and energy transport in irradiated exoplanets (e.g., 122). Firstly, observations generally confirm the trend of lower energy circulation efficiencies (i.e., increased day-night temperature contrasts) with increasing irradiation (i.e., equilibrium temperature). Secondly, and consequently, the majority of phase curves of hot Jupiters show the hot spot in the dayside atmosphere shifted downwind away from the sub-stellar point, as predicted by General Circulation Models.

High-resolution Doppler spectroscopy of hot Jupiters has led to measurements of wind velocities in their atmospheres consistent with predictions of GCMs. Such measurements were first reported for the hot Jupiter HD 209458b using CO absorption in the near-infrared, observed during transit (251), which showed limb-averaged wind speeds of 2 ± 1 km/s. Similar measurements were made for the hot Jupiter HD 189733b using the Na absorption line observed in a high-resolution transmission spectrum in the optical (282) and initially

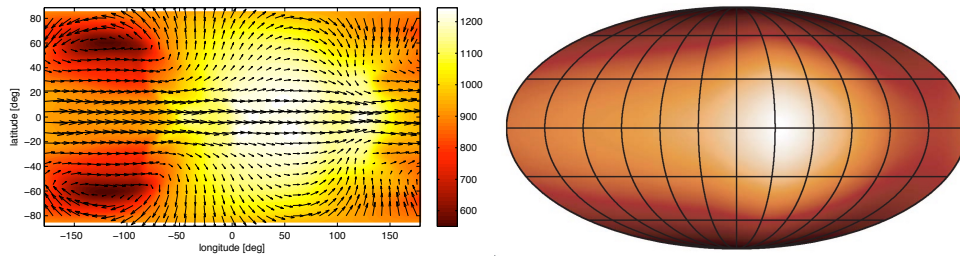


Figure 6: Atmospheric dynamics in hot Jupiters. Left: Theoretical predictions from a GCM of HD 189733b showing an eastward jet and shifting of the hot spot away from the substellar point (241). Wind vectors are shown with arrows and the coloured temperature scale is in Kelvin. Right: Reconstruction of thermal brightness map for the hot Jupiter HD 189733b using thermal phase curve observations in the Spitzer $8\mu\text{m}$ IRAC band (125), conforming with the GCM simulations. Figure courtesy Adam Showman.

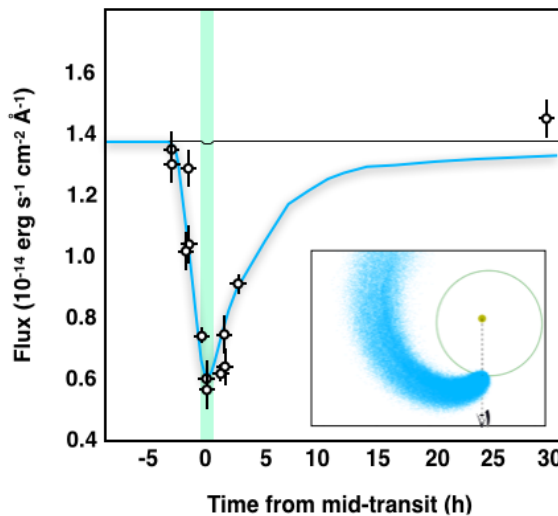


Figure 7: Atmospheric escape of the warm Neptune GJ 436b seen as a strong absorption signature of the stellar HI Lyman- α emission line, based on (71). The figure shows the Lyman- α transit light curve, where each data point is obtained by integrating the flux from the blue wing of the Lyman- α line as a function of time. The optical transit of GJ 436b is shown by the thin horizontal black line and the in-transit time by the vertical green region. Data are from (71) and (142). The blue curve is the model that best fits the spectra as a function of time, resulting from the particle simulation of (32), shown in the inset (where the system is drawn to scale and pole-on). Figure courtesy David Ehrenreich.

reported high wind speeds of 8 ± 2 km/s. The wind speeds were subsequently revised by (155), by accounting for the Rossiter-McLaughlin effect, to be $2.3^{+1.3}_{-1.5}$ km/s and $5.3^{+1.0}_{-1.4}$ km/s eastward on the leading and trailing limbs of the planet, respectively, suggesting a strong equatorial jet. Such measurements are consistent with predictions from GCMs of

hot Jupiters such as HD 209458b and HD 189733b, which show strong eastward equatorial jets and wind velocities of $\sim 1\text{--}3$ km/s (239, 238, 287, 153). Observations such as these provide direct evidence for atmospheric dynamics in hot Jupiters, in addition to thermal phase curves discussed above.

4.5. Atmospheric Escape

As discussed in section 4.1, transmission spectra of transiting exoplanets in the UV have led to strong detections of several atomic species since the early observations of (e.g., 272). In particular, detections of exospheric H using observations of Ly- α absorption in the UV have been reported for a number of giant exoplanets, some recent results include (33, 71). Such observations now only allow key insights into the chemical composition of an exosphere but also provide important constraints on hydrodynamic escape processes, the mass loss rates, and the morphology of the escaping cloud. An extensive discussion of this area can be found in the very recent review of (199) and will not be covered in much detail here. We will note, however, that two key directions are emerging in this area. First, it is becoming evident that highly irradiated Neptune-mass planets orbiting low-mass stars provide the best targets for investigating atmospheric escape processes, e.g., the cases of GJ 436b (71) and GJ 3470b (35). Figure 7 shows the example of GJ 436b. Second, the recent detections of He in the near infrared (253) has opened a new avenue to probe exoplanetary exospheres, both from space using HST as well as from ground (4). These various detections of atomic species have motivated a wide range of theoretical and observational efforts to study escape processes in exoplanets (199).

SUMMARY POINTS

1. The combination of state-of-the-art spectroscopic observations with atmospheric modeling and retrieval techniques has led to a wide range of constraints on atmospheric properties of giant exoplanets.
2. Chemical detections at high confidence include atomic species (H, He, Na, K, Ti, Fe, C, O, Mg) and molecular species (H_2O , CO, HCN, TiO, VO, AlO, CH_4).
3. Reliable abundance constraints are available primarily for H_2O in transiting giant exoplanets. Transmission spectra of most hot Jupiters observed in the visible and near-infrared reveal sub-solar H_2O abundances.
4. Clouds/hazes have been inferred in a number of giant exoplanets, primarily from subdued spectral features and non-Rayleigh slopes in optical transmission spectra.
5. Thermal emission spectra provide key constraints on temperature profiles of giant exoplanets. Thermal inversions have been detected robustly in three ultra-hot Jupiters, with the remaining planets showing no thermal inversions or isothermal profiles.
6. Atmospheric circulation patterns have been constrained using thermal phase curves, phase resolved spectra, measurements of wind speeds and/or eclipse mapping.
7. Atmospheric escape has been observed in several giant exoplanets with hot Neptunes emerging as optimal candidates for detecting exospheres.
8. Overall, atmospheric characterisation is a revolutionary development in the exoplanetary field that only promises to grow as theoretical and observational developments continue.

5. Implications for Planetary Formation

Chemical compositions of planetary atmospheres can provide important insights into their formation and evolutionary mechanisms. As chemical abundances are being measured for exoplanetary atmospheres, an increasing number of studies have been investigating the possibility of using such abundances to answer various open questions about exoplanetary formation. Such studies have mostly focused on giant exoplanets for two main reasons. Firstly, accurate abundance estimates are still only feasibly for giant exoplanets given their higher S/N spectra. Secondly, the H₂/He dominated primary atmospheres of giant exoplanets make them important tracers of their accretion history.

5.1. The Basic Picture

The ultimate goal of this area is to constrain the primordial formation pathways of exoplanets using their present-day observable chemical abundances. Planetary formation involves a large number of highly complex and stochastic processes. At the outset, therefore, it is imperative to establish which particular aspects of planetary formation can be constrained by atmospheric abundances. The basic set-up of the problem is as follows. The primary assumption is that the initial elemental composition of the protoplanetary disk in which a planet formed is the same as that of the host star, since both are expected to have collapsed from the same protostellar cloud. After the initial collapse, the disk cools in time during which the thermodynamic properties of the disk midplane evolve accordingly. As the disk cools, the snowlines of the various volatile species move inwards towards the star. As a result, the chemical compositions of both the gas and solids in the disk evolve as a function of time and location in the disk. For example, H₂O remains in solids outside the H₂O snow line whereas inwards of the snow line it contributes to the gas composition. The same happens with all the prominent volatile species such as CO₂, CO, N₂ and CH₄, which strongly affect the elemental abundance ratios of key elements (e.g., O, C, N) in the disk mid-plane.

Therefore, the chemical composition of a planet depends on the location and time of its formation in the disk as well as the relative amounts of gas and solids it accretes during its formation. Since the planet may migrate through the disk during formation, the net composition is governed by the cumulative accretion history of the planet over its migration pathway. Beyond this basic picture, there are various other complications. For example, the disk itself can have structural inhomogeneities in the form of gaps and overdensities. The solids may be present in a wide distribution of sizes, from micron-sized dust grains to large planetesimals. The disk composition can be affected by various thermal and photochemical processes. Moreover, all these processes happen simultaneously, i.e., the planet forms and grows by accreting while migrating in an evolving disk. At the end of this process, all the material accreted by the planet is reprocessed in the planet post formation, finally resulting in the chemical composition observed in its atmosphere today.

Therefore, the goal of constraining planetary formation processes from atmospheric compositions is a daunting ambition. It is unrealistic to expect for all the involved processes to be constrained solely based on end products. A more reasonable approach is to explore this landscape to assess if any broad regions of the phase space can be constrained or ruled out and to present testable hypotheses given possible atmospheric observations. It is with this spirit that various studies have embarked on this formidable journey.

5.2. Compositions of Accreted Material

The composition of a planet depends on the composition of the material it accretes from the disk both in gas and solid phase. While the gas phase of the disk is mostly composed of H and He with trace quantities of heavy elements, the opposite is true for solids. Therefore, a relatively smaller mass of solids accreted compared to gas can make a disproportionately large contribution to the metallicity of the planet. For example, all the heavy elements in a given amount of solar composition gas amount to only $\sim 1\%$ by mass. Therefore, the relative amounts of gas to solids accreted by a planet determines the heavy metal content of the atmosphere. On the other hand, the compositions of the gas and dust both evolve in time and orbital distance in the protoplanetary disk (73). While various factors govern the evolution of different disk properties, the most relevant property influencing the composition in the disk mid-plane is temperature which is cooler at larger distances and later times. The mid-plane temperature governs the locations of the snow lines of prominent chemical species which in turn govern whether a particular species is in gas phase or solid phase at a given location.

Several studies have investigated the compositions of gas and solids that could be accreted by giant planetary atmospheres. The simplest picture is one of a steady state disk where the mid-plane compositions of the gas and solids are determined solely based on the location in the disk relative to the relevant snow lines. Initial studies considered fixed composition disks where the abundances of prominent species (e.g. H_2O , CO , CO_2) were adopted based on observations of protoplanetary environments and the interstellar medium, or on theoretical models (197, 190, 164). With the abundances fixed, the disk temperature at a given orbital distance governs whether each of these species is in gas phase or in solid phase. The sublimation temperatures of these species are such that the H_2O snow line is closest to the star (nominally around 5 AU) followed by snow lines of CO_2 , CO , and other gases such as CH_4 , N_2 , and noble gases, in that order. For example, between the H_2O and CO_2 snow lines, H_2O is in solid ice phase whereas all the other volatiles are in gas phase. Therefore, how much gas versus ice is accreted onto the planet at a given location decides how much of each species is accreted onto the planet. The sum-total of all the accreted species contributes to the net elemental abundances of oxygen, carbon, nitrogen, etc. Already from this simple picture it is clear that the oxygen abundance in the gas decreases outward in the disk, with a decrement at each snow line, whereas that in the solids increases. This implies that the C/O ratio in the gas increases whereas that in the solids decreases as a function of distance in the disk (197). Figure 8 shows the variation of the C/O ratio in the gas and solids in the disk midplane. Therefore, depending on how much gas versus solids a planet accretes at a given formation location it can accrete a wide range of C/O ratios, spanning sub-solar or super-solar C/O ratios; the solar C/O ratio is 0.54 (7). Beyond the simple picture above, a host of other processes can influence the gas and solid composition in the disk midplane over time (73).

5.3. End-to-end Studies

In recent years various studies have explored the effects of different formation pathways on the final compositions of giant exoplanets. Detailed reviews on the evolution of this area until recently can be found in (163, 210, 140). Figure 9 shows the carbon-oxygen plane with predictions from models assuming different formation pathways.

Here, after briefly summarising initial works, we focus on the latest developments and

the future landscape of this area. The first studies in this direction in the context of giant exoplanets were motivated by the possibilities of measuring elemental abundances and C/O ratios in their atmospheres. Traditionally, solar-system based formation models were used to explain such elemental abundance ratios in giant exoplanets. These argued for local inhomogeneities in formation conditions to explain non-solar abundances (191, 169). However, (197) noted that even in a solar-composition disk, with a C/O ratio of 0.54 (7), the C/O ratio of gas and solids in the disk mid-plane changed as a function of radial distance relative to the snow lines of prominent species such as H₂O, CO, and CO₂. They argued that beyond the CO₂ snow line, the gas composition is dominated by CO, giving it a C/O ratio of 1, such that giant planets forming in such regions with predominant gas accretion can have C/O ratios of 1. This study was followed by (164) who showed that a wide range of C/O ratios and metallicities are possible in giant exoplanets depending on their formation and migration pathways relative to the snowlines. In particular, high C/O ratios (~ 1) and sub-stellar metallicities in giant exoplanets were shown to be possible only via mechanisms that did not involve significant solid accretion into the envelope, e.g., disk-free migration or through pebble accretion without core erosion (165). Meanwhile, a wide range of C/O ratios and super-solar metallicities were possible for disk migration through abundant accretion of planetesimals (164, 184).

The early studies have been followed by various end-to-end studies which investigated the effects of a wide range of formation conditions on atmospheric compositions of giant exoplanets (184, 165, 56, 1, 31, 3). These studies have focused largely on hot Jupiters, which are most amenable to atmospheric abundance measurements. These models attempt to accurately capture the formation of the planet, via different mechanisms, while accounting for the chemical inventory of the accreted material. The important differences between the models are in the treatment of the disk chemistry, the specific accretion efficiency of solids versus gas, and in the nature of the accreted material. For example, (184) reported an integrated chain model which comprises the formation of the planet by core accretion, migration through the disk, and chemical enrichment caused by planetesimal accretion. They explore two formation pathways, depending on the formation location of the planet relative to the H₂O snow line. In this model, the atmospheric elemental composition of the planet is dominated by planetesimal accretion and, regardless of the two formation locations, the composition is predominantly oxygen-rich; owing to significant accretion of H₂O ice. On another front, (56) reported models where the chemistry is treated with an astrochemical model coupled with a disk evolution model. The planet formation is governed by core accretion with gas and planetesimal accretion and formed in specific regions ('traps') in the disk. They also find planets with oxygen-rich C/O ratios of 0.23, owing to an assumed lower C/O ratio in the disc and the assumption of no planetesimal accretion. (269) also found giant planets with high water abundances, but did not compute C/O ratios. Overall, across these various studies, planets formed via core accretion involving significant planetesimal accretion and migration through the disk result in oxygen-rich composition of the planetary envelopes (164, 184, 56).

More recent studies have investigated alternate mechanisms that can influence the heavy element content in giant exoplanetary atmospheres. One new direction explored in this context is the formation of giant planets via pebble accretion and migration through the evolving disk with a given chemical prescription (165). The important aspect of this formation mechanism (139) is that the solid accretion occurs predominantly during the formation of the core until the pebble isolation mass is reached, following which gas accretion dominates

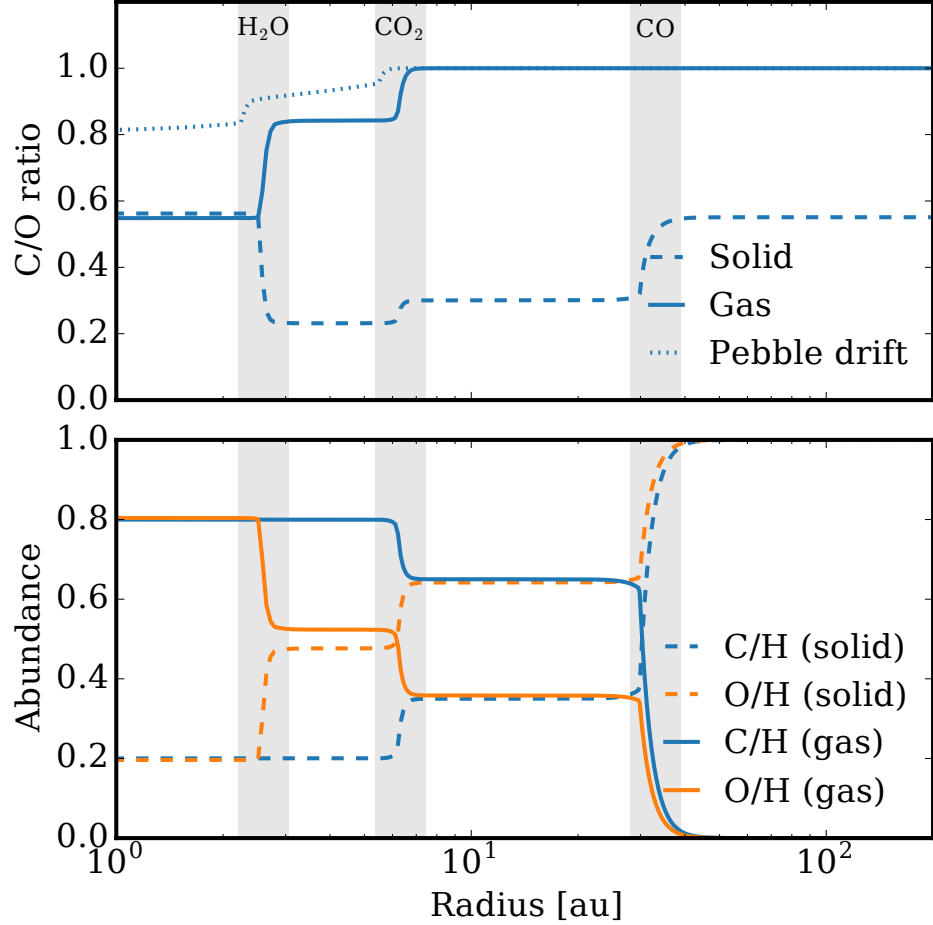


Figure 8: Top: Variation of the C/O ratio of the gas and solids in a disc due to freeze-out. The CO, CO₂ and H₂O snow lines are shown. The width of the snow lines is set by the balance of adsorption vs thermal desorption (31). The dotted line shows a typical case where pebble drift has enhanced the C/O inner the inner region (2, 31). Conversely, the conversion of CO to CO₂ and complex organic molecules reduces the C/O ratio of the gas and increases the C/O ratio of the ices (e.g. (72, 73)). Bottom: Abundance of carbon and oxygen relative to solar in solid and gas phases.

with almost no solid accretion. In this scenario, the envelope composition is dominated by the gas composition, which is typically metal poor and the accreted solids are sequestered in the core. This leads to generally sub-stellar metallicities and the C/O ratio of the envelope depends on the location of accreted gas relative to the snow lines. In principle, super-stellar metallicities and low C/O ratios can also be attained if the cores are allowed to erode and contribute to the envelope composition (1, 165). Beyond this picture, however, further studies have considered the effect of pebble drift on the composition of gas in

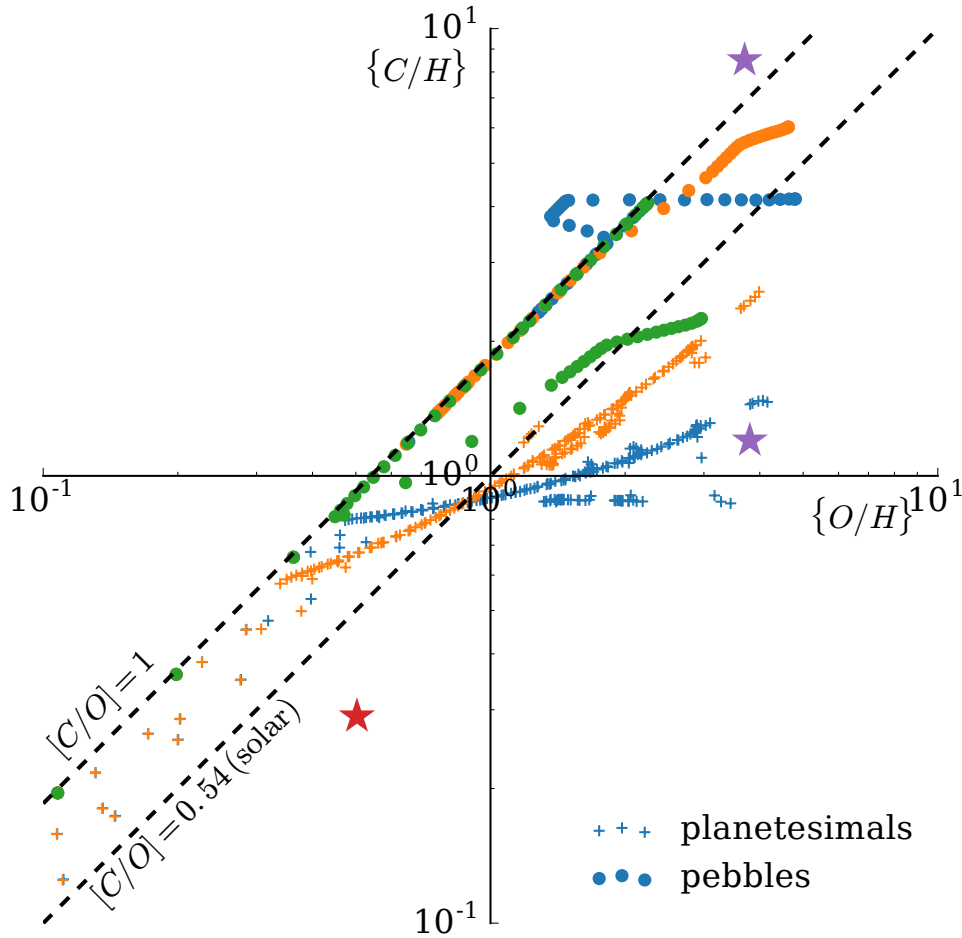


Figure 9: Carbon and oxygen abundances arising from different core accretion models of giant planet formation. The circles denote planets formed by pebble accretion, taking into account the chemical evolution driven by pebble migration (31). Models based on the planetesimal accretion scenario taking into account migration are shown as plus signs (164). The point colours denote the chemical abundance models used from (164): the case 1 and 2 equilibrium models are shown in blue and orange, and the case 2 no-reactions model in green. The purple stars show the models of Jupiter mass planets from (184), while the models of (57) are given by the red star.

the disk (207, 31). Inward drifting pebbles sublime at each snow line crossing, thereby enriching the metallicity of the gas inward of the snow line. A planet formed by accreting such metal-rich gas can naturally possess both high metallicities and a wide range of C/O ratios depending on the specific formation pathway. Overall, the pebble accretion paradigm provides a natural way to explain a wide range of metallicities as well as C/O ratios in giant exoplanetary atmospheres. A new generation of studies are now beginning to investigate

the effect of complex disk chemistry on the compositions of the planets formed via different mechanisms. In previous studies, the treatment of chemistry in the disk was simplistic based on fixed condensation fronts depending on the mid plane temperature (197, 164). New studies considering full chemical kinetics along with the evolving disk show significant evolution in the gas and ice compositions (e.g. C/O ratios) of the disk mid-plane beyond what fixed chemical prescriptions assume (73). Future end-to-end models including such full chemical treatment may find a wider diversity of planetary compositions than currently predicted. A recent study with an end-to-end model combined a full chemical model with a hydrodynamical model of planet formation by gravitational instability (113). They suggested the possibility of dust grains, along with their volatiles, sedimenting to the cores and preventing the enrichment of their envelopes with the volatiles. Therefore, planetary envelopes formed via gravitational instability may not entirely reflect the bulk composition of the formation locations. Finally, new studies are also suggesting that besides the carbon and oxygen abundances, the nitrogen abundance may also be an important diagnostic of planetary formation pathways (208, 30).

SUMMARY POINTS

1. The key goal is to use elemental abundances in exoplanetary atmospheres to constrain their formation and migration history. Basic premise: elemental composition of protoplanetary disk same as the protostellar nebula.
2. Composition of the disk (e.g. C/H, O/H, C/O ratios) in gas and solids change as a function of orbital distance and age, with snow lines of H₂O, CO, and CO₂ governing key transitions in elemental abundances. Further in the disk beyond the CO₂ snowline the C/O ratio in the gas approaches 1.
3. Giant planet composition depends on the relative amounts of gas vs solids accreted by the planet from different locations in the disk relative to the snow lines.
4. Giant planet formation via core accretion with significant planetesimal accretion and migration through the disk leads to super-solar metallicities and sub-solar (oxygen-rich) C/O ratios, i.e., $C/O \lesssim 0.5$.
5. Giant planet formation beyond the CO/CO₂ snow lines but with disk-free migration can lead to sub-solar metallicities and carbon-rich compositions with C/O approaching 1.
6. Giant planet formation by pebble accretion can lead to a diverse range of metallicities and C/O ratios depending on the efficiency of core erosion as well the contribution of pebble drift to the disk composition.

6. Habitable Planets and Biosignatures

The detection of a biosignature in the atmosphere of a terrestrial-size planet represents the holy grail of exoplanetary science. The current population of discovered transiting exoplanets contain dozens of rocky exoplanets in their habitable zones (138). It is conceivable that a chemical signature in the atmosphere of a habitable exoplanet may be discovered within the next decade with large facilities in space (e.g. JWST) and ground (e.g. E-ELT). However, whether or not the detected chemical will be a robust signature of life is a subject of much debate (179, 49). Nevertheless, the prospects of finding a potential biosignature in

the atmosphere of a terrestrial exoplanet are promising given the rapid increase in new discoveries of such planets and the new observational facilities on the horizon. Recent reviews of various aspects of this area can be found in (179, 49, 87, 228, 163)

6.1. Habitable Planets

One of the most revolutionary findings from exoplanet detection surveys has been the high occurrence rate of rocky exoplanets in the solar neighbourhood (88). Earth-size planets are now known to be very common, and more so around low-mass stars. In particular, dozens of terrestrial-size exoplanets are known with equilibrium temperatures conducive for liquid water to exist on the surface. In principle, these planets may be be classed as habitable-zone planets, though the extent of a habitable zone is subject to the planetary interior and atmospheric properties as well as the astrophysical conditions assumed. A detailed review of the various factors affecting habitability of terrestrial exoplanets can be found in various recent works (97, 228, 130, 95, 119, 235, 99). These factors include the atmospheric and geophysical conditions in the planet, its orbital parameters and evolution, the nature and evolution of the host star and its environment, magnetospheric protection, and the planet's formation history, among other factors. The dozens of potentially habitable planets now known are found orbiting mostly late-type K and M stars, meaning their environmental conditions may be expected to be very different and diverse compared to the terrestrial experience. An exact Earth analog is yet to be discovered. From an observational standpoint, however, planets orbiting late-type stars provide a fortuitous opportunity to characterise their atmospheres. Their small stellar sizes provide large planet-star contrasts, both in radius and flux, making them conducive for transit spectroscopy. This 'small star opportunity' has emerged to be the cornerstone in the search for habitable planets and biosignatures in the near future. In particular, the recent discoveries of habitable-zone planets orbiting nearby stars such as TRAPPIST-1 (92) and Proxima Cen (5) provide new impetus in this direction. As discussed below, discovering biosignatures in the atmospheres of such planets may be within the reach of upcoming observational facilities.

6.2. Biosignatures

The ultimate breakthrough in exoplanetary science will be the detection of a biosignature in the atmosphere of a rocky habitable-zone exoplanet. But, what is a biosignature? Nominally, an ideal biosignature gas would need to satisfy some natural conditions (230), such as (a) it should not have any false positives, i.e., should not be a product of non-biological mechanisms, (b) it should have strong enough spectral features to be detectable, and (c) it should be abundant enough to be detectable. Traditionally, the prominent biosignatures based on the Earth's atmosphere were thought to be O_2 , O_3 , N_2O , and CH_4 ; though CH_4 is known to be produced in minor quantities geologically (49). By far, the most promising biosignature for Earth-like planets had originally been considered to be O_2 and, hence, O_3 . However, recent studies suggest the possibility of abiotic mechanisms which can also produce O_2 in detectable quantities (179). It may be safe to say that currently there is no single molecule that may qualify as a unique biosignature upon detection in extraterrestrial atmospheres. Nevertheless, recent studies are suggesting several approaches for progress in this direction. Firstly, any assessment of a biosignature has to take into account various aspects of the environment that are required for the planet to be conducive to life (49). These include characterisation of the stellar host and bulk properties of the planet as well as the

atmospheric ‘climatic’ conditions. Ultimately, a probabilistic measure of life may be more plausible than a binary inference (49). Furthermore, while there is no single ideal molecule, the combination of multiple species (e.g. O_2 and CH_4) may be a potential biosignature under the given conditions. In this regard, a detection of O_2 and CH_4 and/or N_2O along with liquid H_2O on a habitable-zone planet, i.e. an almost exact Earth analogue, may be a sure sign of life.

While designing metrics centered on terrestrial experience may be a convenient starting point, it will likely serve us better to be open to surprises. As is common experience in exoplanetary science, reality has rarely conformed to our expectations. From planetary detections to atmospheric studies, most of the findings to date have defied expectations. Initial studies show that the possible space of biochemical byproducts may comprise of numerous chemical species (226, 228), and may indeed be non-denumerably infinite. For example, species such as O_2 , O_3 , N_2O , CH_4 , CO_2 , CH_3SH , CH_3Cl , C_2H_6 and NH_3 , may all be potential bio-signatures in Earth-like conditions (226, 228). In addition, different stellar environments may reduce or increase the chances of potential biosignatures. For example, while planets around M dwarfs may be subject to an extremely harsh UV environment which can be catastrophic for terrestrial-like life (234, 119), the same environments may also be conducive for abiogenesis, producing species essential for primordial life such as HCN (216, 217).

6.3. Observational Prospects

A prudent approach to searching for biosignatures in terrestrial exoplanets is likely to be one that is driven by observational capability rather than terracentric predictions of an ideal biosignature. Several recent studies have discussed the observational capabilities of upcoming facilities that would be sensitive to detecting chemical signatures in rocky exoplanets (119, 229, 226, 87). Atmospheric characterisation of Earth-like planets around sun-like stars may be beyond the capabilities of current and upcoming facilities. However, a more promising pathway that has emerged in recent years is the atmospheric characterisation of planets orbiting low-mass stars such as TRAPPIST-1 (92) and Proxima Centauri (5). Recent studies show that dedicated spectroscopic observations with JWST could take us within the reach of detecting chemical signatures for habitable planets in both TRAPPIST-1 (185, 17) and Proxima Cen b (252). Furthermore, these atmospheres may also be probed by large ground-based facilities (e.g. E-ELT) using a combination of high-resolution spectroscopy and high-contrast imaging (248, 220). New studies are underway for a future generation of facilities such as LUVOIR (28) and HabEx (181) that would enable characterisation of potential biospheres of Earth-like planets around sun-like stars (280).

SUMMARY POINTS

1. The detection of an atmospheric biosignature in a rocky exoplanet represents the holy grail of the field.
2. Defining a unique biosignature remains a theoretical challenge, but several candidate molecules have been suggested.
3. Detection of a potential biosignature may be within the reach of upcoming observational facilities.

7. Future Landscape

It is clear that the future of exoplanetary science lies in detailed characterisation of exoplanetary atmospheres. Numerous surveys both from space and on the ground are geared towards discovering planets orbiting nearby bright stars which enable detailed atmospheric spectroscopy of the planets. Current and upcoming transit surveys include K2, TESS, and CHEOPS from space and ground-based surveys such as SuperWASP, NGTS, KELT, SPECULOOS, and MEARTH, followed by the PLATO mission on a longer term. In parallel, direct-imaging surveys with instruments such as GPI, SPHERE, and SCExAO aim to discover long-period exoplanets around young nearby stars. These surveys promise a large sample of targets for detailed comparative characterisation of exoplanetary atmospheres over the next decade. On the other hand, the prospects of various new observational facilities for atmospheric spectroscopy of exoplanets are equally exciting. In the imminent future, JWST will play a pivotal role in revolutionising the field. In the late 2020s space-based facilities such as ARIEL will enable atmospheric characterisation of large populations of exoplanets, and large ground-based telescopes such as E-ELT, GMT, and TMT, may enable detections of biosignatures in atmospheres of habitable-zone exoplanets. Here we discuss the future landscape of the field, focusing specifically on observational facilities at present and in the imminent future.

7.1. Exoplanetary Atmospheres with Current Facilities

As discussed in this work, current facilities are already capable of providing detailed insights into exoplanetary atmospheres. What can we expect from these facilities in the future? HST, which has been the workhorse of the field in recent years, will continue to be a powerful facility. Prior to JWST, which is currently expected to launch in 2021, HST is the only space-based facility for transit spectroscopy over a broad spectral range, from UV to near-IR. As discussed above, spectra over the broad spectral range from visible to NIR have been obtained with HST for over ten giant exoplanets, albeit with variable data quality. Similarly, spectra are becoming available for tens more transiting exoplanets obtained with one or more HST instruments albeit with generally limited data quality. These kinds of survey programs are beneficial to provide a general census of exoplanetary spectra over a large sample (244, 266, 86), but are of limited utility for obtaining stringent constraints on relevant atmospheric properties of any individual planet. As discussed in (162), H₂O abundances have been measured to better than 0.5 dex precisions in only a handful of exoplanets. Retrievals of high-precision chemical abundances and other atmospheric properties from transit spectra require uncertainties on data that are nearly 20 ppm (63, 166, 132, 157). While such precisions can be obtained in single transit/eclipse observations for planets orbiting bright host stars such as HD 209458b (63), fainter host stars require coadding spectra from multiple events, as demonstrated for WASP-43b (256, 132). This is the approach required with HST, i.e., dedicated efforts for high-precision (20 ppm) transit spectroscopy over the entire HST spectral range of a sizeable sample of exoplanets. Such a program has the potential to obtain high precision chemical abundances of H₂O, and other possible species (e.g. CH₄, HCN, NH₃, TiO/VO, Na, K), P-T profiles, constraints on clouds/hazes for a large sample of exoplanets to enable comparative atmospheric characterisation.

At the same time, as discussed earlier, ground-based facilities have started to provide high-precision spectra for both close-in planets as well as directly imaged planets on large orbital separations, as shown in Fig. 4. In particular, ground-based transit spectroscopy

at both low-resolution and high-resolution will continue to provide robust detections of several chemical species such as Na, K, TiO, and He (e.g., 232, 193). Such detections can be made using instruments on existing large ground-based telescopes (e.g. VLT and GTC) as well as high-resolution spectrographs on medium-size telescopes such as the HARPS spectrograph (106). In addition, high resolution Doppler spectroscopy in thermal emission with large ground-based telescopes promise high confidence detections of chemical species. As discussed earlier, this technique has been instrumental in strong detections of key species such as H₂O, CO, TiO, and HCN in several hot Jupiters using the CRIRES instrument on the VLT. The upcoming CRIRES+ spectrograph on VLT along with other high-resolution spectrographs on medium-size (4m class) telescopes promise new opportunities for the future (41). Ultimately, the combination of high-resolution Doppler spectroscopy along with low-resolution transit spectroscopy will provide the best constraints possible. Similarly, the combination of the cross-correlation technique with high-contrast imaging provides new promise for medium-high resolution spectroscopy at extreme flux contrasts(248, 106). These advancements will naturally be further enhanced with the next generation of large ground-based facilities such as the E-ELT, GMT, and TMT.

7.2. Exoplanetary Atmospheres with JWST

The James Webb Space Telescope (JWST) has the potential to revolutionise the study of exoplanetary atmospheres. The key advantages of JWST for exoplanet spectroscopy are apparent - its large aperture, and hence high sensitivity, and wide spectral range, particularly in the infrared. Several studies have investigated the science that can be pursued with JWST (94, 62, 18). Here, we discuss some key highlights and some strategic factors that need to be considered to maximise the potential of JWST for atmospheric characterisation of exoplanets.

JWST will clearly revolutionise our understanding of giant planets which will be the most conducive planets for atmospheric characterisation as already demonstrated with current facilities. This is most apparent when considering that the range of species that JWST will be able to observe in hot Jupiters may supersede what we know for Jupiter in our own solar system, which is currently the most studied giant planet. The wide spectral range of JWST spans the absorption features of a range of chemical species, as shown in Fig. 10. All the prominent molecular species containing the key volatile elements (e.g. O, C, and N) such as H₂O, CO, CH₄, CO₂, HCN, C₂H₂, and NH₃, have strong spectral features in the JWST spectral range. The mixing ratios of these species can provide unprecedented constraints on the corresponding elemental abundance ratios, e.g., C/H, O/H, N/H, C/O, N/O, etc. These molecular and elemental ratios have the potential to provide a wide range of constraints on numerous atmospheric processes and planetary formation mechanisms, as discussed in this work. Moreover, the spectral range of JWST, as seen in Fig. 10, also contains strong signatures of various molecules containing refractory elements (e.g. TiO, VO, AlO, TiH, etc) which provide important constraints on both the metal content in the atmospheres as well as the possibility of aerosols comprised of these species, depending on the temperatures. Most of these species are not measurable for giant planets in the solar system due to their low temperatures. On the other hand, JWST will be able to measure these for planets over a wide mass range, possibly from super-Earths to super-Jupiters.

While JWST will readily detect various chemical species in exoplanetary atmospheres, precise quantitative constraints on the atmospheric properties will require judicious plan-

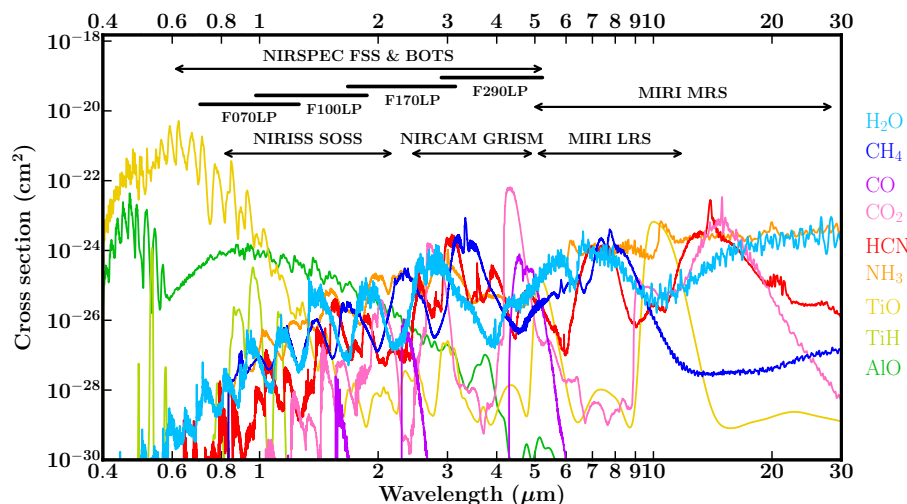


Figure 10: Cross-sections of various molecules across optical and infrared wavelengths. Spectral ranges covered by certain modes of JWST's four instruments (NIRSpec, NIRISS, NIRCам, and MIRI) are shown for comparison. For NIRSpec, the wavelength coverage of individual filters is also shown. JWST's extensive spectral coverage will enable detailed chemical characterisations of exoplanetary atmospheres.

ning. The atmospheric properties including the chemical abundances, temperature profiles, and other properties, are determined from spectra using atmospheric retrieval methods. It is conceivable that chemical abundances and ratios (e.g. H_2O , C/O ratio, etc) can be determined to precisions within 0.5 dex (94, 17), more so considering that retrievals on HST spectra are already providing best precisions on H_2O abundances of ~ 0.5 dex (166, 157, 277). However, the precision of the determined chemical abundances, depends both on the spectral range as well as the precision, while ensuring that the desired chemical species has strong signature in the observed range. Firstly, as shown in Fig. 11, the spectral ranges of the near-infrared instruments (NIRISS and NIRSPEC) are composed of multiple modes each of which covers a narrow range, typically 1-2 μm wide, and can be observed only one at a time. Consequently, obtaining the full spectral range of JWST would require a significant investment of JWST time on any one target. Therefore, judicious choices need to be made in choosing the observing modes which depend on a range of system properties including the stellar brightness, planetary bulk properties (e.g. size, gravity, temperature), expected atmospheric composition and spectral amplitude. Various studies have investigated the information content in JWST spectra as a function of these properties (e.g., 94, 17, 183, 218) using simulated JWST data. For example, (17) show that for a given amount of observing time with JWST NIRISS and NIRSpec the information content in an observed spectrum of a certain molecule in multiple modes is higher than that observed in a single mode at high precision. On the other hand, for certain host stars a broader coverage over 1-5 μm range can be achieved with the NIRSpec in GRISM mode. In principle, the MIRI instrument has significant larger spectral range in each of two models in the 5-28 μm but have lower

resolution and fewer relevant spectral features compared to the near-infrared.

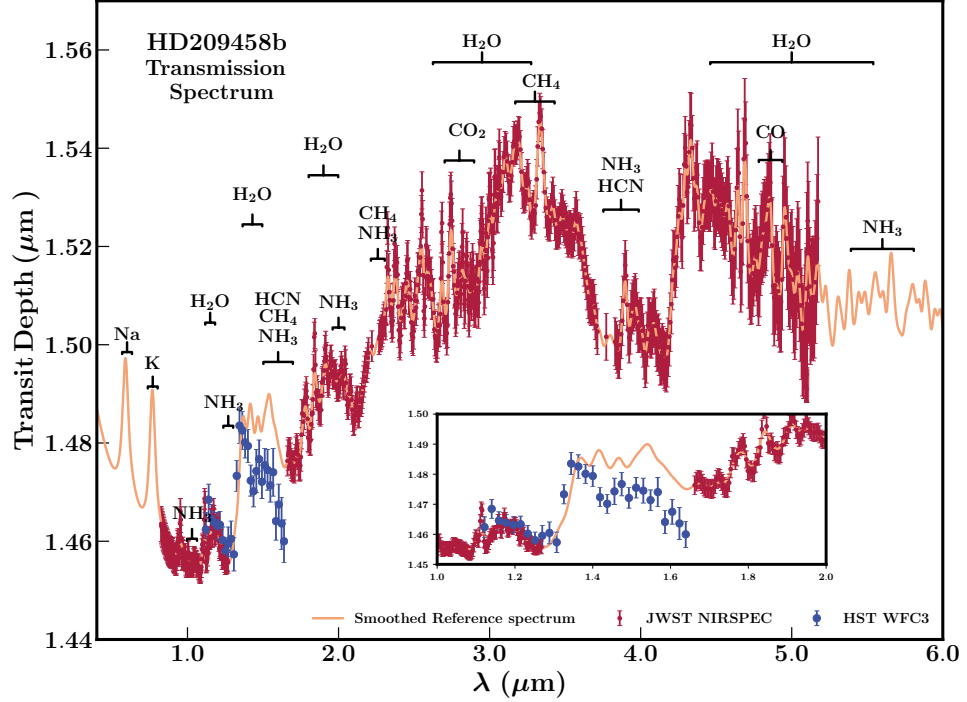


Figure 11: Simulated JWST/NIRSpec data based on the model spectrum of a planet resembling HD 209458b. Simulated data is shown by dark red points, while the model spectrum is shown in pink. Data is simulated for the G140H, G235H and G395H high-resolution gratings available with NIRSpec. The native-resolution simulated data points have been binned to a lower resolution for clarity. In the inset, real HST/WFC3 data for HD 209458b (blue points and error bars) is shown for reference. The chemical features probed in this spectral range are labelled with brackets; atmospheric observations with JWST will allow higher resolutions and smaller uncertainties than present capabilities, resulting in more robust and varied chemical detections.

Another challenge for transit spectroscopy with JWST lies in the possibility of cloudy atmospheres. As discussed in this work, transmission spectra have suggested the presence of clouds/hazes in transiting exoplanets over a range of temperatures and masses, revealed through low-amplitude H_2O features as well as non-Rayleigh spectral slopes in the optical (244, 86, 266). Current retrieval codes are able to retrieve the chemical abundances from such spectra in addition to constraining the cloud/haze properties (16, 157). However, such joint constraints require transmission spectra in visible wavelengths to resolve the degeneracies between the chemical abundances and clouds/hazes. While this has been possible with HST, using the STIS spectrograph, the same will be lacking for JWST which does not have significant spectral coverage in the optical. Therefore, complementary transmission spectra in the visible observed with HST and/or large ground-based telescopes will be

required to accurately retrieve chemical compositions of cloudy atmospheres using JWST transmission spectra. The recent successes of HST and high-precision ground-based transmission spectroscopy of giant exoplanets (232, 193, 53) provide promising prospects in this direction. On the other hand, for many of the irradiated giant exoplanets dayside thermal emission spectra may provide a more viable means to constrain their atmospheric compositions, rather than transmission spectra. The dayside spectra are less influenced by clouds owing to the higher irradiation/temperatures as well as the fact that an opaque cloud deck essentially acts as a photosphere and the compositions constrained are those above the cloud deck by default. Moreover, infrared spectra of several hot Jupiters with HST and Spitzer, as well as with high-resolution ground-based spectra have already revealed clear signatures of molecular features and temperature gradients suggesting the lack of strong interference due to clouds/hazes on the dayside spectra. Besides chemical compositions, JWST will provide unprecedented constraints on a host of other atmospheric properties of exoplanets. In addition, JWST will provide the first opportunity to characterise the atmospheres of super-Earths and terrestrial-size exoplanets in detail, especially for planets orbiting low-mass stars (252).

DISCLOSURE STATEMENT

The authors are not aware of any affiliations, memberships, funding, or financial holdings that might be perceived as affecting the objectivity of this review.

ACKNOWLEDGMENTS

At the outset I would like to thank the countless colleagues in the field who have contributed to this exciting frontier of exoplanetary science. I would like to thank the editors at ARAA for the opportunity to serve the field with this review, and Debra Fischer for her very helpful comments on the review. The volume of literature on this emerging area of exoplanetary atmospheres is both exciting and astounding at the same time, a testament to the exponential progress we are witnessing. As such, given the space and time available for this review, choices had to be made about which aspects to cover at what level. I therefore sincerely apologize to all those colleagues whose work may not have received coverage in this review. I would like to deeply thank my students Luis Welbanks and Anjali Piette for their invaluable contributions to the figures, tables, and sorting the references in this review, Arazi Pinhas for help with the tables, some figures and references, Richard Booth for help with Figs. 8 & 9, and Siddharth Gandhi for help with some of the references. I would also like to thank Adam Showman and David Ehrenreich for their very helpful comments and contributions to sections 4.4 and 4.5, respectively.

LITERATURE CITED

1. M. Ali-Dib. Disentangling hot Jupiters formation location from their chemical composition. *MNRAS*, 467:2845–2854, May 2017.
2. Mohamad Ali-Dib, Olivier Mousis, Jean-Marc Petit, and Jonathan I. Lunine. Carbon-rich Planet Formation in a Solar Composition Disk. *ApJ*, 785:125, April 2014.
3. Y. Alibert. Maximum mass of planetary embryos that formed in core-accretion models. *A&A*, 606:A69, October 2017.

4. R. Allart, V. Bourrier, C. Lovis, D. Ehrenreich, J. J. Spake, A. Wyttenbach, L. Pino, F. Pepe, D. K. Sing, and A. Lecavelier des Etangs. Spectrally resolved helium absorption from the extended atmosphere of a warm Neptune-mass exoplanet. *Science*, 362:1384–1387, December 2018.
5. G. Anglada-Escudé, P. J. Amado, J. Barnes, Z. M. Berdiñas, R. P. Butler, G. A. L. Coleman, I. de La Cueva, S. Dreizler, M. Endl, B. Giesers, S. V. Jeffers, J. S. Jenkins, H. R. A. Jones, M. Kiraga, M. Kürster, M. J. López-González, C. J. Marvin, N. Morales, J. Morin, R. P. Nelson, J. L. Ortiz, A. Ofir, S.-J. Paardekooper, A. Reiners, E. Rodríguez, C. Rodríguez-López, L. F. Sarmiento, J. P. Strachan, Y. Tsapras, M. Tuomi, and M. Zechmeister. A terrestrial planet candidate in a temperate orbit around Proxima Centauri. *Nature*, 536:437–440, August 2016.
6. J. Arcangeli, J.-M. Désert, M. R. Line, J. L. Bean, V. Parmentier, K. B. Stevenson, L. Kreidberg, J. J. Fortney, M. Mansfield, and A. P. Showman. H^- Opacity and Water Dissociation in the Dayside Atmosphere of the Very Hot Gas Giant WASP-18b. *ApJ*, 855:L30, March 2018.
7. M. Asplund, N. Grevesse, A. J. Sauval, and P. Scott. The Chemical Composition of the Sun. *ARA&A*, 47:481–522, September 2009.
8. N. Astudillo-Defru and P. Rojo. Ground-based detection of calcium and possibly scandium and hydrogen in the atmosphere of HD 209458b. *A&A*, 557:A56, September 2013.
9. S. K. Atreya, A. Crida, T. Guillot, J. I. Lunine, N. Madhusudhan, and O. Mousis. The Origin and Evolution of Saturn, with Exoplanet Perspective. *ArXiv e-prints*, June 2016.
10. R. J. Barber, J. Tennyson, G. J. Harris, and R. N. Tolchenov. A high-accuracy computed water line list. *MNRAS*, 368:1087–1094, May 2006.
11. R. J. Barber, J. K. Strange, C. Hill, O. L. Polyansky, G. C. Mellau, S. N. Yurchenko, and J. Tennyson. ExoMol line lists - III. An improved hot rotation-vibration line list for HCN and HNC. *MNRAS*, 437:1828–1835, January 2014.
12. T. Barman. Identification of Absorption Features in an Extrasolar Planet Atmosphere. *ApJ*, 661:L191–L194, June 2007.
13. T. S. Barman, F. Allard, I. Baraffe, G. Chabrier, and P. H. Hauschildt. Extrasolar planets: atmospheres, spectra, and evolution. In F. Favata, G. A. J. Hussain, and B. Battrick, editors, *13th Cambridge Workshop on Cool Stars, Stellar Systems and the Sun*, volume 560 of *ESA Special Publication*, page 437, March 2005.
14. T. S. Barman, Q. M. Konopacky, B. Macintosh, and C. Marois. Simultaneous Detection of Water, Methane, and Carbon Monoxide in the Atmosphere of Exoplanet HR8799b. *ApJ*, 804:61, May 2015.
15. T. S. Barman, B. Macintosh, Q. M. Konopacky, and C. Marois. Clouds and Chemistry in the Atmosphere of Extrasolar Planet HR8799b. *ApJ*, 733:65, May 2011.
16. J. K. Barstow, S. Aigrain, P. G. J. Irwin, and D. K. Sing. A Consistent Retrieval Analysis of 10 Hot Jupiters Observed in Transmission. *ApJ*, 834:50, January 2017.
17. N. E. Batalha, N. K. Lewis, M. R. Line, J. Valenti, and K. Stevenson. Strategies for Constraining the Atmospheres of Temperate Terrestrial Planets with JWST. *ApJ*, 856:L34, April 2018.
18. J. L. Bean, K. B. Stevenson, N. M. Batalha, Z. Berta-Thompson, L. Kreidberg, N. Crouzet, B. Benneke, M. R. Line, D. K. Sing, H. R. Wakeford, H. A. Knutson, E. M.-R. Kempton, J.-M. Désert, I. Crossfield, N. E. Batalha, J. de Wit, V. Parmentier, J. Harrington, J. I. Moses, M. Lopez-Morales, M. K. Alam, J. Blecic, G. Bruno, A. L. Carter, J. W. Chapman, L. Decin, D. Dragomir, T. M. Evans, J. J. Fortney, J. D. Fraine, P. Gao, A. García Muñoz, N. P. Gibson, J. M. Goyal, K. Heng, R. Hu, S. Kendrew, B. M. Kilpatrick, J. Krick, P.-O. Lagage, M. Lendl, T. Loudén, N. Madhusudhan, A. M. Mandell, M. Mansfield, E. M. May, G. Morello, C. V. Morley, N. Nikolov, S. Redfield, J. E. Roberts, E. Schlawin, J. J. Spake, K. O. Todorov, A. Tsaras, O. Venot, W. C. Waalkes, P. J. Wheatley, R. T. Zellem, D. Angerhausen, D. Barrado, L. Carone, S. L. Casewell, P. E. Cubillos, M. Damiano, M. de

- Val-Borro, B. Drummond, B. Edwards, M. Endl, N. Espinoza, K. France, J. E. Gizis, T. P. Greene, T. K. Henning, Y. Hong, J. G. Ingalls, N. Iro, P. G. J. Irwin, T. Kataria, F. Lahuis, J. Leconte, J. Lillo-Box, S. Lines, J. D. Lothringer, L. Mancini, F. Marchis, N. Mayne, E. Palle, E. Rauscher, G. Roudier, E. L. Shkolnik, J. Southworth, M. R. Swain, J. Taylor, J. Teske, G. Tinetti, P. Tremblin, G. S. Tucker, R. van Boekel, I. P. Waldmann, I. C. Weaver, and T. Zingales. The Transiting Exoplanet Community Early Release Science Program for JWST. *ArXiv e-prints*, March 2018.
19. T. G. Beatty, N. Madhusudhan, R. Pogge, S. M. Chung, A. Bierly, B. S. Gaudi, and D. W. Latham. The Broadband and Spectrally Resolved H-band Eclipse of KELT-1b and the Role of Surface Gravity in Stratospheric Inversions in Hot Jupiters. *AJ*, 154:242, December 2017.
 20. T. G. Beatty, N. Madhusudhan, A. Tsiaras, M. Zhao, R. L. Gilliland, H. A. Knutson, A. Shporer, and J. T. Wright. Evidence for Atmospheric Cold-trap Processes in the Noninverted Emission Spectrum of Kepler-13Ab Using HST/WFC3. *AJ*, 154:158, October 2017.
 21. C. A. Beichman and T. P. Greene. *Observing Exoplanets with the James Webb Space Telescope*, page 85. 2017.
 22. T. J. Bell and N. B. Cowan. Increased Heat Transport in Ultra-hot Jupiter Atmospheres through H₂ Dissociation and Recombination. *ApJ*, 857:L20, April 2018.
 23. B. Benneke and S. Seager. How to Distinguish between Cloudy Mini-Neptunes and Water/Volatile-dominated Super-Earths. *ApJ*, 778:153, December 2013.
 24. J. L. Birkby, R. J. de Kok, M. Brogi, E. J. W. de Mooij, H. Schwarz, S. Albrecht, and I. A. G. Snellen. Detection of water absorption in the day side atmosphere of HD 189733 b using ground-based high-resolution spectroscopy at 3.2 μ m. *MNRAS*, 436:L35–L39, November 2013.
 25. J. L. Birkby, R. J. de Kok, M. Brogi, H. Schwarz, and I. A. G. Snellen. Discovery of Water at High Spectral Resolution in the Atmosphere of 51 Peg b. *AJ*, 153:138, March 2017.
 26. J. L. Birkby. Exoplanet Atmospheres at High Spectral Resolution. *arXiv e-prints*, June 2018.
 27. J. Blečić, I. Dobbs-Dixon, and T. Greene. The Implications of 3D Thermal Structure on 1D Atmospheric Retrieval. *ApJ*, 848:127, October 2017.
 28. M. R. Bolcar, L. Feinberg, K. France, B. J. Rauscher, D. Redding, and D. Schiminovich. Initial technology assessment for the Large-Aperture UV-Optical-Infrared (LUVOIR) mission concept study. In *Space Telescopes and Instrumentation 2016: Optical, Infrared, and Millimeter Wave*, volume 9904 of *Proc. SPIE*, page 99040J, July 2016.
 29. M. Bonnefoy, A. Zurlo, J. L. Baudino, P. Lucas, D. Mesa, A.-L. Maire, A. Vigan, R. Galicher, D. Homeier, F. Marocco, R. Gratton, G. Chauvin, F. Allard, S. Desidera, M. Kasper, C. Moutou, A.-M. Lagrange, J. Antichi, A. Baruffolo, J. Baudrand, J.-L. Beuzit, A. Boccaletti, F. Cantalloube, M. Carillet, J. Charton, R. U. Claudi, A. Costille, K. Dohlen, C. Dominik, D. Fantinel, P. Feautrier, M. Feldt, T. Fusco, P. Gigan, J. H. Girard, L. Gluck, C. Gry, T. Henning, M. Janson, M. Langlois, F. Madec, Y. Magnard, D. Maurel, D. Mawet, M. R. Meyer, J. Milli, O. Moeller-Nilsson, D. Mouillet, A. Pavlov, D. Perret, P. Pujet, S. P. Quanz, S. Rochat, G. Rousset, A. Roux, B. Salasnich, G. Salter, J.-F. Sauvage, H. M. Schmid, A. Sevin, C. Soenke, E. Stadler, M. Turatto, S. Udry, F. Vakili, Z. Wahhaj, and F. Wildi. First light of the VLT planet finder SPHERE. IV. Physical and chemical properties of the planets around HR8799. *A&A*, 587:A58, March 2016.
 30. R. A. Booth and C. J. Clarke. Chemical enrichment of the planet-forming region as probed by accretion. *MNRAS*, 473:757–764, January 2018.
 31. R. A. Booth, C. J. Clarke, N. Madhusudhan, and J. D. Ilee. Chemical enrichment of giant planets and discs due to pebble drift. *MNRAS*, 469:3994–4011, August 2017.
 32. V. Bourrier, D. Ehrenreich, and A. Lecavelier des Etangs. Radiative braking in the extended exosphere of GJ 436 b. *A&A*, 582:A65, October 2015.
 33. V. Bourrier, A. Lecavelier des Etangs, H. Dupuy, D. Ehrenreich, A. Vidal-Madjar, G. Hébrard, G. E. Ballester, J.-M. Désert, R. Ferlet, D. K. Sing, and P. J. Wheatley. Atmospheric escape

- from HD 189733b observed in H I Lyman- α : detailed analysis of HST/STIS September 2011 observations. *A&A*, 551:A63, March 2013.
34. V. Bourrier, A. Lecavelier des Etangs, D. Ehrenreich, Y. A. Tanaka, and A. A. Vidotto. An evaporating planet in the wind: stellar wind interactions with the radiatively braked exosphere of GJ 436 b. *A&A*, 591:A121, June 2016.
 35. V. Bourrier, A. Lecavelier des Etangs, D. Ehrenreich, J. Sanz-Forcada, R. Allart, G. E. Ballester, L. A. Buchhave, O. Cohen, D. Deming, T. M. Evans, A. García Muñoz, G. W. Henry, T. Kataria, P. Lavvas, N. Lewis, M. López-Morales, M. Marley, D. K. Sing, and H. R. Wakeford. Hubble PanCET: an extended upper atmosphere of neutral hydrogen around the warm Neptune GJ 3470b. *A&A*, 620:A147, December 2018.
 36. I. A. Boutle, N. J. Mayne, B. Drummond, J. Manners, J. Goyal, F. Hugo Lambert, D. M. Acreman, and P. D. Earnshaw. Exploring the climate of Proxima B with the Met Office Unified Model. *A&A*, 601:A120, May 2017.
 37. M. Brogi, I. A. G. Snellen, R. J. de Kok, S. Albrecht, J. Birkby, and E. J. W. de Mooij. The signature of orbital motion from the dayside of the planet τ Boötis b. *Nature*, 486:502–504, June 2012.
 38. M. Brogi, I. A. G. Snellen, R. J. de Kok, S. Albrecht, J. L. Birkby, and E. J. W. de Mooij. Detection of Molecular Absorption in the Dayside of Exoplanet 51 Pegasi b? *ApJ*, 767:27, April 2013.
 39. M. Brogi, R. J. de Kok, J. L. Birkby, H. Schwarz, and I. A. G. Snellen. Carbon monoxide and water vapor in the atmosphere of the non-transiting exoplanet HD 179949 b. *A&A*, 565:A124, May 2014.
 40. M. Brogi, R. J. de Kok, S. Albrecht, I. A. G. Snellen, J. L. Birkby, and H. Schwarz. Rotation and Winds of Exoplanet HD 189733 b Measured with High-dispersion Transmission Spectroscopy. *ApJ*, 817:106, February 2016.
 41. M. Brogi, M. Line, J. Bean, J.-M. Désert, and H. Schwarz. A Framework to Combine Low- and High-resolution Spectroscopy for the Atmospheres of Transiting Exoplanets. *ApJ*, 839:L2, April 2017.
 42. B. Burningham, M. S. Marley, M. R. Line, R. Lupu, C. Visscher, C. V. Morley, D. Saumon, and R. Freedman. Retrieval of atmospheric properties of cloudy L dwarfs. *MNRAS*, 470:1177–1197, September 2017.
 43. A. Burrows, J. Budaj, and I. Hubeny. Theoretical Spectra and Light Curves of Close-in Extrasolar Giant Planets and Comparison with Data. *ApJ*, 678:1436–1457, May 2008.
 44. A. Burrows, I. Hubeny, J. Budaj, H. A. Knutson, and D. Charbonneau. Theoretical Spectral Models of the Planet HD 209458b with a Thermal Inversion and Water Emission Bands. *ApJ*, 668:L171–L174, October 2007.
 45. A. Burrows and G. Orton. Giant Planet Atmospheres and Spectra. *ArXiv e-prints*, October 2009.
 46. A. Burrows and C. M. Sharp. Chemical Equilibrium Abundances in Brown Dwarf and Extrasolar Giant Planet Atmospheres. *ApJ*, 512:843–863, February 1999.
 47. S. H. C. Cabot, N. Madhusudhan, G. A. Hawker, and S. Gandhi. On the robustness of analysis techniques for molecular detections using high-resolution exoplanet spectroscopy. *MNRAS*, 482:4422–4436, February 2019.
 48. N. Casasayas-Barris, E. Pallé, G. Nowak, F. Yan, L. Nortmann, and F. Murgas. Detection of sodium in the atmosphere of WASP-69b. *A&A*, 608:A135, December 2017.
 49. D. C. Catling, J. Krissansen-Totton, N. Y. Kiang, D. Crisp, T. D. Robinson, S. DasSarma, A. J. Rushby, A. Del Genio, W. Bains, and S. Domagal-Goldman. Exoplanet Biosignatures: A Framework for Their Assessment. *Astrobiology*, 18:709–738, June 2018.
 50. D. Charbonneau, T. M. Brown, R. W. Noyes, and R. L. Gilliland. Detection of an Extrasolar Planet Atmosphere. *ApJ*, 568:377–384, March 2002.
 51. D. Charbonneau, H. A. Knutson, T. Barman, L. E. Allen, M. Mayor, S. T. Megeath, D. Queloz,

- and S. Udry. The Broadband Infrared Emission Spectrum of the Exoplanet HD 189733b. *ApJ*, 686:1341–1348, October 2008.
52. G. Chen, E. Pallé, L. Nortmann, F. Murgas, H. Parviainen, and G. Nowak. The GTC exoplanet transit spectroscopy survey. VI. Detection of sodium in WASP-52b’s cloudy atmosphere. *A&A*, 600:L11, April 2017.
 53. G. Chen, E. Pallé, L. Welbanks, J. Prieto-Arranz, N. Madhusudhan, S. Gandhi, N. Casasayas-Barris, F. Murgas, L. Nortmann, N. Crouzet, H. Parviainen, and D. Gandolfi. The GTC exoplanet transit spectroscopy survey. IX. Detection of haze, Na, K, and Li in the super-Neptune WASP-127b. *A&A*, 616:A145, August 2018.
 54. J. Chilcote, L. Pueyo, R. J. De Rosa, J. Vargas, B. Macintosh, V. P. Bailey, T. Barman, B. Bauman, S. Bruzzzone, J. Bulger, A. S. Burrows, A. Cardwell, C. H. Chen, T. Cotten, D. Dillon, R. Doyon, Z. H. Draper, G. Duchêne, J. Dunn, D. Erikson, M. P. Fitzgerald, K. B. Follette, D. Gavel, S. J. Goodsell, J. R. Graham, A. Z. Greenbaum, M. Hartung, P. Hibon, L.-W. Hung, P. Ingraham, P. Kalas, Q. Konopacky, J. E. Larkin, J. Maire, F. Marchis, M. S. Marley, C. Marois, S. Metchev, M. A. Millar-Blanchaer, K. M. Morzinski, E. L. Nielsen, A. Norton, R. Oppenheimer, D. Palmer, J. Patience, M. Perrin, L. Poyneer, A. Rajan, J. Rameau, F. T. Rantakyrö, N. Sadakuni, L. Saddlemyer, D. Savransky, A. C. Schneider, A. Serio, A. Sivaramakrishnan, I. Song, R. Soummer, S. Thomas, J. K. Wallace, J. J. Wang, K. Ward-Duong, S. Wiktorowicz, and S. Wolff. 1-2.4 μ m Near-IR Spectrum of the Giant Planet β Pictoris b Obtained with the Gemini Planet Imager. *AJ*, 153:182, April 2017.
 55. K. D. Colón, E. B. Ford, S. Redfield, J. J. Fortney, M. Shabram, H. J. Deeg, and S. Mahadevan. Probing potassium in the atmosphere of HD 80606b with tunable filter transit spectrophotometry from the Gran Telescopio Canarias. *MNRAS*, 419:2233–2250, January 2012.
 56. A. J. Cridland, R. E. Pudritz, and M. Alessi. Composition of early planetary atmospheres - I. Connecting disc astrochemistry to the formation of planetary atmospheres. *MNRAS*, 461:3274–3295, September 2016.
 57. A. J. Cridland, Ralph E. Pudritz, Tilman Birnstiel, L. Ilse-dore Cleaves, and Edwin A. Bergin. Composition of early planetary atmospheres - II. Coupled Dust and chemical evolution in protoplanetary discs. *MNRAS*, 469:3910–3927, August 2017.
 58. I. J. M. Crossfield and L. Kreidberg. Trends in Atmospheric Properties of Neptune-size Exoplanets. *AJ*, 154:261, December 2017.
 59. N. Crouzet, P. R. McCullough, D. Deming, and N. Madhusudhan. Water Vapor in the Spectrum of the Extrasolar Planet HD 189733b. II. The Eclipse. *ApJ*, 795:166, November 2014.
 60. M. Damiano, G. Morello, A. Tsiaras, T. Zingales, and G. Tinetti. Near-IR Transmission Spectrum of HAT-P-32b using HST/WFC3. *AJ*, 154:39, July 2017.
 61. J. de Wit, M. Gillon, B.-O. Demory, and S. Seager. Towards consistent mapping of distant worlds: secondary-eclipse scanning of the exoplanet HD 189733b. *A&A*, 548:A128, December 2012.
 62. D. Deming, S. Seager, J. Winn, E. Miller-Ricci, M. Clampin, D. Lindler, T. Greene, D. Charbonneau, G. Laughlin, G. Ricker, D. Latham, and K. Ennico. Discovery and Characterization of Transiting Super Earths Using an All-Sky Transit Survey and Follow-up by the James Webb Space Telescope. *PASP*, 121:952, September 2009.
 63. D. Deming, A. Wilkins, P. McCullough, A. Burrows, J. J. Fortney, E. Agol, I. Dobbs-Dixon, N. Madhusudhan, N. Crouzet, J.-M. Desert, R. L. Gilliland, K. Haynes, H. A. Knutson, M. Line, Z. Magic, A. M. Mandell, S. Ranjan, D. Charbonneau, M. Clampin, S. Seager, and A. P. Showman. Infrared Transmission Spectroscopy of the Exoplanets HD 209458b and XO-1b Using the Wide Field Camera-3 on the Hubble Space Telescope. *ApJ*, 774:95, September 2013.
 64. B.-O. Demory, J. de Wit, N. Lewis, J. Fortney, A. Zsom, S. Seager, H. Knutson, K. Heng, N. Madhusudhan, M. Gillon, T. Barclay, J.-M. Desert, V. Parmentier, and N. B. Cowan. Inference of Inhomogeneous Clouds in an Exoplanet Atmosphere. *ApJ*, 776:L25, October

- 2013.
65. B.-O. Demory, M. Gillon, J. de Wit, N. Madhusudhan, E. Bolmont, K. Heng, T. Kataria, N. Lewis, R. Hu, J. Krick, V. Stamenković, B. Benneke, S. Kane, and D. Queloz. A map of the large day-night temperature gradient of a super-Earth exoplanet. *Nature*, 532:207–209, April 2016.
 66. I. Dobbs-Dixon and N. B. Cowan. Wavelength Does Not Equal Pressure: Vertical Contribution Functions and Their Implications for Mapping Hot Jupiters. *ApJ*, 851:L26, December 2017.
 67. B. Drummond, N. J. Mayne, I. Baraffe, P. Tremblin, J. Mannes, D. S. Amundsen, J. Goyal, and D. Acreman. The effect of metallicity on the atmospheres of exoplanets with fully coupled 3D hydrodynamics, equilibrium chemistry, and radiative transfer. *A&A*, 612:A105, May 2018.
 68. B. Drummond, P. Tremblin, I. Baraffe, D. S. Amundsen, N. J. Mayne, O. Venot, and J. Goyal. The effects of consistent chemical kinetics calculations on the pressure-temperature profiles and emission spectra of hot Jupiters. *A&A*, 594:A69, October 2016.
 69. D. Ehrenreich, X. Bonfils, C. Lovis, X. Delfosse, T. Forveille, M. Mayor, V. Neves, N. C. Santos, S. Udry, and D. Ségransan. Near-infrared transmission spectrum of the warm-Uranus GJ 3470b with the Wide Field Camera-3 on the Hubble Space Telescope. *A&A*, 570:A89, October 2014.
 70. D. Ehrenreich, V. Bourrier, X. Bonfils, A. Lecavelier des Etangs, G. Hébrard, D. K. Sing, P. J. Wheatley, A. Vidal-Madjar, X. Delfosse, S. Udry, T. Forveille, and C. Moutou. Hint of a transiting extended atmosphere on 55 Cancri b. *A&A*, 547:A18, November 2012.
 71. D. Ehrenreich, V. Bourrier, P. J. Wheatley, A. Lecavelier des Etangs, G. Hébrard, S. Udry, X. Bonfils, X. Delfosse, J.-M. Désert, D. K. Sing, and A. Vidal-Madjar. A giant comet-like cloud of hydrogen escaping the warm Neptune-mass exoplanet GJ 436b. *Nature*, 522:459–461, June 2015.
 72. C. Eistrup, C. Walsh, and E. F. van Dishoeck. Setting the volatile composition of (exo)planet-building material. Does chemical evolution in disk midplanes matter? *A&A*, 595:A83, November 2016.
 73. Christian Eistrup, Catherine Walsh, and Ewine F. van Dishoeck. Molecular abundances and C/O ratios in chemically evolving planet-forming disk midplanes. *A&A*, 613:A14, May 2018.
 74. Lisa J. Esteves, Ernst J. W. de Mooij, Ray Jayawardhana, Chris Watson, and Remco de Kok. A search for water in a super-earth atmosphere: High-resolution optical spectroscopy of 55canceri e. *AJ*, 153(6):268, may 2017.
 75. T. M. Evans, F. Pont, D. K. Sing, S. Aigrain, J. K. Barstow, J.-M. Désert, N. Gibson, K. Heng, H. A. Knutson, and A. Lecavelier des Etangs. The Deep Blue Color of HD 189733b: Albedo Measurements with Hubble Space Telescope/Space Telescope Imaging Spectrograph at Visible Wavelengths. *ApJ*, 772:L16, August 2013.
 76. T. M. Evans, D. K. Sing, T. Kataria, J. Goyal, N. Nikolov, H. R. Wakeford, D. Deming, M. S. Marley, D. S. Amundsen, G. E. Ballester, J. K. Barstow, L. Ben-Jaffel, V. Bourrier, L. A. Buchhave, O. Cohen, D. Ehrenreich, A. García Muñoz, G. W. Henry, H. Knutson, P. Lavvas, A. Lecavelier Des Etangs, N. K. Lewis, M. López-Morales, A. M. Mandell, J. Sanz-Forcada, P. Tremblin, and R. Lupu. An ultrahot gas-giant exoplanet with a stratosphere. *Nature*, 548:58–61, August 2017.
 77. T. M. Evans, D. K. Sing, H. R. Wakeford, N. Nikolov, G. E. Ballester, B. Drummond, T. Kataria, N. P. Gibson, D. S. Amundsen, and J. Spake. Detection of H₂O and Evidence for TiO/VO in an Ultra-hot Exoplanet Atmosphere. *ApJ*, 822:L4, May 2016.
 78. D. A. Fischer, A. W. Howard, G. P. Laughlin, B. Macintosh, S. Mahadevan, J. Sahlmann, and J. C. Yee. Exoplanet Detection Techniques. *Protostars and Planets VI*, pages 715–737, 2014.
 79. L. N. Fletcher, G. S. Orton, N. A. Teanby, P. G. J. Irwin, and G. L. Bjoraker. Methane and its isotopologues on Saturn from Cassini/CIRS observations. *Icarus*, 199:351–367, February 2009.
 80. J. J. Fortney. The effect of condensates on the characterization of transiting planet atmo-

- spheres with transmission spectroscopy. *MNRAS*, 364:649–653, December 2005.
81. J. J. Fortney, K. Lodders, M. S. Marley, and R. S. Freedman. A Unified Theory for the Atmospheres of the Hot and Very Hot Jupiters: Two Classes of Irradiated Atmospheres. *ApJ*, 678:1419–1435, May 2008.
 82. L. Fossati, C. A. Haswell, and C. S. Froning. A multi-wavelength analysis of the WASP-12 planetary system. In A. Sozzetti, M. G. Lattanzi, and A. P. Boss, editors, *The Astrophysics of Planetary Systems: Formation, Structure, and Dynamical Evolution*, volume 276 of *IAU Symposium*, pages 163–166, November 2011.
 83. L. Fossati, C. A. Haswell, C. S. Froning, L. Hebb, S. Holmes, U. Kolb, C. Helling, A. Carter, P. Wheatley, A. Collier Cameron, B. Loeillet, D. Pollacco, R. Street, H. C. Stempels, E. Simpson, S. Udry, Y. C. Joshi, R. G. West, I. Skillen, and D. Wilson. Metals in the Exosphere of the Highly Irradiated Planet WASP-12b. *ApJ*, 714:L222–L227, May 2010.
 84. J. Fraine, D. Deming, B. Benneke, H. Knutson, A. Jordán, N. Espinoza, N. Madhusudhan, A. Wilkins, and K. Todorov. Water vapour absorption in the clear atmosphere of a Neptune-sized exoplanet. *Nature*, 513:526–529, September 2014.
 85. J. D. Fraine, D. Deming, A. Jordan, and H. Knutson. Super-Earths, Warm Neptunes, and Hot Jupiters: Transmission Spectroscopy for Comparative Planetology. In *American Astronomical Society Meeting Abstracts #225*, volume 225 of *American Astronomical Society Meeting Abstracts*, page 124.01, January 2015.
 86. Guangwei Fu, Drake Deming, Heather Knutson, Nikku Madhusudhan, Avi Mandell, and Jonathan Fraine. Statistical Analysis of Hubble/WFC3 Transit Spectroscopy of Extrasolar Planets. *ApJ*, 847:L22, October 2017.
 87. Y. Fujii, D. Angerhausen, R. Deitrick, S. Domagal-Goldman, J. L. Grenfell, Y. Hori, S. R. Kane, E. Pallé, H. Rauer, N. Siegler, K. Stapelfeldt, and K. B. Stevenson. Exoplanet Biosignatures: Observational Prospects. *Astrobiology*, 18:739–778, June 2018.
 88. B. J. Fulton, E. A. Petigura, A. W. Howard, H. Isaacson, G. W. Marcy, P. A. Cargile, L. Hebb, L. M. Weiss, J. A. Johnson, T. D. Morton, E. Sinukoff, I. J. M. Crossfield, and L. A. Hirsch. The California-Kepler Survey. III. A Gap in the Radius Distribution of Small Planets. *AJ*, 154:109, September 2017.
 89. S. Gandhi and N. Madhusudhan. GENESIS: new self-consistent models of exoplanetary spectra. *MNRAS*, 472:2334–2355, December 2017.
 90. B. S. Gaudi, S. Seager, B. Mennesson, A. Kiessling, K. Warfield, G. Kuan, K. Cahoy, J. T. Clarke, S. Domagal-Goldman, L. Feinberg, O. Guyon, J. Kasdin, D. Mawet, T. Robinson, L. Rogers, P. Scowen, R. Somerville, K. Stapelfeldt, C. Stark, D. Stern, M. Turnbull, S. Martin, O. Alvarez-Salazar, R. Amini, W. Arnold, B. Balasubramanian, M. Baysinger, L. Blais, T. Brooks, R. Calvet, V. Cormarkovic, C. Cox, R. Danner, J. Davis, L. Dorsett, M. Effinger, R. Eng, J. Garcia, J. Gaskin, J. Harris, S. Howe, B. Knight, J. Krist, D. Levine, M. Li, D. Lisman, M. Mandic, L. Marchen, C. Marrese-Reading, J. McGowen, A. Miyaguchi, R. Morgan, B. Nemati, S. Nikzad, J. Nissen, M. Novicki, T. Perrine, D. Redding, M. Richards, M. Rud, D. Scharf, G. Serabyn, S. Shaklan, S. Smith, M. Stahl, P. Stahl, H. Tang, D. Van Buren, J. Villalvazo, S. Warwick, D. Webb, R. Wofford, J. Woo, M. Wood, J. Ziemer, E. Douglas, V. Faramaz, S. Hildebrandt, T. Meshkat, P. Plavchan, G. Ruane, and N. Turner. The Habitable Exoplanet Observatory (HabEx) Mission Concept Study Interim Report. *arXiv e-prints*, September 2018.
 91. A. Garcia Munoz and K. G. Isaak. Probing exoplanet clouds with optical phase curves. *Proceedings of the National Academy of Science*, 112:13461–13466, November 2015.
 92. M. Gillon, E. Jehin, S. M. Lederer, L. Delrez, J. de Wit, A. Burdanov, V. Van Grootel, A. J. Burgasser, A. H. M. J. Triaud, C. Opitom, B.-O. Demory, D. K. Sahu, D. Bardalez Gagliuffi, P. Magain, and D. Queloz. Temperate Earth-sized planets transiting a nearby ultracool dwarf star. *Nature*, 533:221–224, May 2016.
 93. A. Z. Greenbaum, L. Pueyo, J.-B. Ruffio, J. J. Wang, R. J. De Rosa, J. Aguilar, J. Rameau,

- T. Barman, C. Marois, M. S. Marley, Q. Konopacky, A. Rajan, B. Macintosh, M. Ansdell, P. Arriaga, V. P. Bailey, J. Bulger, A. S. Burrows, J. Chilcote, T. Cotten, R. Doyon, G. Duchêne, M. P. Fitzgerald, K. B. Follette, B. Gerard, S. J. Goodsell, J. R. Graham, P. Hibon, L.-W. Hung, P. Ingraham, P. Kalas, J. E. Larkin, J. Maire, F. Marchis, S. Metchev, M. A. Millar-Blanchaer, E. L. Nielsen, A. Norton, R. Oppenheimer, D. Palmer, J. Patience, M. D. Perrin, L. Poyneer, F. T. Rantakyö, D. Savransky, A. C. Schneider, A. Sivaramakrishnan, I. Song, R. Soummer, S. Thomas, J. K. Wallace, K. Ward-Duong, S. Wiktorowicz, and S. Wolff. GPI Spectra of HR 8799 c, d, and e from 1.5 to 2.4 μm with KLIP Forward Modeling. *AJ*, 155:226, June 2018.
94. T. P. Greene, M. R. Line, C. Montero, J. J. Fortney, J. Lustig-Yaeger, and K. Luther. Characterizing Transiting Exoplanet Atmospheres with JWST. *ApJ*, 817:17, January 2016.
95. J. L. Grenfell, B. Stracke, P. von Paris, B. Patzer, R. Titz, A. Segura, and H. Rauer. The response of atmospheric chemistry on earthlike planets around F, G and K Stars to small variations in orbital distance. *Planet. Space Sci.*, 55:661–671, April 2007.
96. C. J. Grillmair, A. Burrows, D. Charbonneau, L. Armus, J. Stauffer, V. Meadows, J. van Cleve, K. von Braun, and D. Levine. Strong water absorption in the dayside emission spectrum of the planet HD189733b. *Nature*, 456:767–769, December 2008.
97. M. Güdel, R. Dvorak, N. Erkaev, J. Kasting, M. Khodachenko, H. Lammer, E. Pilat-Lohinger, H. Rauer, I. Ribas, and B. E. Wood. Astrophysical Conditions for Planetary Habitability. *Protostars and Planets VI*, pages 883–906, 2014.
98. T. Guillot. The composition of transiting giant extrasolar planets. *Physica Scripta Volume T*, 130(1):014023, August 2008.
99. N. Haghighipour and S. N. Raymond. Habitable Planet Formation in Binary Planetary Systems. *ApJ*, 666:436–446, September 2007.
100. G. J. Harris, J. Tennyson, B. M. Kaminsky, Y. V. Pavlenko, and H. R. A. Jones. Improved HCN/HNC linelist, model atmospheres and synthetic spectra for WZ Cas. *MNRAS*, 367:400–406, March 2006.
101. G. A. Hawker, N. Madhusudhan, S. H. C. Cabot, and S. Gandhi. Evidence for Multiple Molecular Species in the Hot Jupiter HD 209458b. *ApJ*, 863:L11, August 2018.
102. K. Haynes, A. M. Mandell, N. Madhusudhan, D. Deming, and H. Knutson. Spectroscopic Evidence for a Temperature Inversion in the Dayside Atmosphere of Hot Jupiter WASP-33b. *ApJ*, 806:146, June 2015.
103. C. Helling, G. Lee, I. Dobbs-Dixon, N. Mayne, D. S. Amundsen, J. Khaimova, A. A. Unger, J. Manners, D. Acreman, and C. Smith. The mineral clouds on HD 209458b and HD 189733b. *MNRAS*, 460:855–883, July 2016.
104. K. Heng. A Cloudiness Index for Transiting Exoplanets Based on the Sodium and Potassium Lines: Tentative Evidence for Hotter Atmospheres Being Less Cloudy at Visible Wavelengths. *ApJ*, 826:L16, July 2016.
105. K. Heng and D. Kitzmann. Analytical Models of Exoplanetary Atmospheres. IV. Improved Two-stream Radiative Transfer for the Treatment of Aerosols. *ApJS*, 232:20, October 2017.
106. H. J. Hoeijmakers, D. Ehrenreich, K. Heng, D. Kitzmann, S. L. Grimm, R. Allart, R. Deitrick, A. Wyttenbach, M. Oreshenko, L. Pino, P. B. Rimmer, E. Molinari, and L. Di Fabrizio. Atomic iron and titanium in the atmosphere of the exoplanet KELT-9b. *Nature*, 560:453–455, August 2018.
107. H. J. Hoeijmakers, H. Schwarz, I. A. G. Snellen, R. J. de Kok, M. Bonnefoy, G. Chauvin, A. M. Lagrange, and J. H. Girard. Medium-resolution integral-field spectroscopy for high-contrast exoplanet imaging. Molecule maps of the β Pictoris system with SINFONI. *A&A*, 617:A144, October 2018.
108. X. Huang, R. S. Freedman, S. A. Tashkun, D. W. Schwenke, and T. J. Lee. Semi-empirical $^{12}\text{C}^{16}\text{O}_2$ IR line lists for simulations up to 1500 K and 20,000 cm^{-1} . *J. Quant. Spec. Radiat. Transf.*, 130:134–146, November 2013.

109. Xinchuan Huang, David W. Schwenke, Richard S. Freedman, and Timothy J. Lee. Ames-2016 line lists for 13 isotopologues of CO_2 : Updates, consistency, and remaining issues. *J. Quant. Spec. Radiat. Transf.*, 203:224 – 241, 2017. HITRAN2016 Special Issue.
110. I. Hubeny. Model atmospheres of sub-stellar mass objects. *MNRAS*, 469:841–869, July 2017.
111. I. Hubeny, A. Burrows, and D. Sudarsky. A Possible Bifurcation in Atmospheres of Strongly Irradiated Stars and Planets. *ApJ*, 594:1011–1018, September 2003.
112. C. M. Huitson, D. K. Sing, F. Pont, J. J. Fortney, A. S. Burrows, P. A. Wilson, G. E. Ballester, N. Nikolov, N. P. Gibson, D. Deming, S. Aigrain, T. M. Evans, G. W. Henry, A. Lecavelier des Etangs, A. P. Showman, A. Vidal-Madjar, and K. Zahnle. An HST optical-to-near-IR transmission spectrum of the hot Jupiter WASP-19b: detection of atmospheric water and likely absence of TiO . *MNRAS*, 434:3252–3274, October 2013.
113. J. D. Ilee, D. H. Forgan, M. G. Evans, C. Hall, R. Booth, C. J. Clarke, W. K. M. Rice, A. C. Boley, P. Caselli, T. W. Hartquist, and J. M. C. Rawlings. The chemistry of protoplanetary fragments formed via gravitational instabilities. *MNRAS*, 472:189–204, November 2017.
114. M. Janson, T. D. Brandt, M. Kuzuhara, D. S. Spiegel, C. Thalmann, T. Currie, M. Bonnefoy, N. Zimmerman, S. Sorahana, T. Kotani, J. Schlieder, J. Hashimoto, T. Kudo, N. Kusakabe, L. Abe, W. Brandner, J. C. Carson, S. Egner, M. Feldt, M. Goto, C. A. Grady, O. Guyon, Y. Hayano, M. Hayashi, S. Hayashi, T. Henning, K. W. Hodapp, M. Ishii, M. Iye, R. Kandori, G. R. Knapp, J. Kwon, T. Matsuo, M. W. McElwain, K. Mede, S. Miyama, J.-I. Morino, A. Moro-Martín, T. Nakagawa, T. Nishimura, T.-S. Pyo, E. Serabyn, T. Suenaga, H. Suto, R. Suzuki, Y. Takahashi, M. Takami, N. Takato, H. Terada, D. Tomono, E. L. Turner, M. Watanabe, J. Wisniewski, T. Yamada, H. Takami, T. Usuda, and M. Tamura. Direct Imaging Detection of Methane in the Atmosphere of GJ 504 b. *ApJ*, 778:L4, November 2013.
115. M. Janson, J. Carson, C. Thalmann, M. W. McElwain, M. Goto, J. Crepp, J. Wisniewski, L. Abe, W. Brandner, A. Burrows, S. Egner, M. Feldt, C. A. Grady, T. Golota, O. Guyon, J. Hashimoto, Y. Hayano, M. Hayashi, S. Hayashi, T. Henning, K. W. Hodapp, M. Ishii, M. Iye, R. Kandori, G. R. Knapp, T. Kudo, N. Kusakabe, M. Kuzuhara, T. Matsuo, S. Mayama, S. Miyama, J.-I. Morino, A. Moro-Martín, T. Nishimura, T.-S. Pyo, E. Serabyn, H. Suto, R. Suzuki, M. Takami, N. Takato, H. Terada, B. Tofflemire, D. Tomono, E. L. Turner, M. Watanabe, T. Yamada, H. Takami, T. Usuda, and M. Tamura. Near-infrared Multi-band Photometry of the Substellar Companion GJ 758 B. *ApJ*, 728:85, February 2011.
116. A. G. Jensen, S. Redfield, M. Endl, W. D. Cochran, L. Koesterke, and T. Barman. A Detection of $\text{H}\alpha$ in an Exoplanetary Exosphere. *ApJ*, 751:86, June 2012.
117. N. Jovanovic, F. Martinache, O. Guyon, C. Clergeon, G. Singh, T. Kudo, V. Garrel, K. Newmann, D. Doughty, J. Lozi, J. Males, Y. Minowa, Y. Hayano, N. Takato, J. Morino, J. Kuhn, E. Serabyn, B. Norris, P. Tuthill, G. Schworer, P. Stewart, L. Close, E. Huby, G. Perrin, S. Lacour, L. Gauchet, S. Vievard, N. Murakami, F. Oshiyama, N. Baba, T. Matsuo, J. Nishikawa, M. Tamura, O. Lai, F. Marchis, G. Duchene, T. Kotani, and J. Woillez. The Subaru Coronagraphic Extreme Adaptive Optics System: Enabling High-Contrast Imaging on Solar-System Scales. *PASP*, 127:890, September 2015.
118. P. Kalas, J. R. Graham, E. Chiang, M. P. Fitzgerald, M. Clampin, E. S. Kite, K. Stapelfeldt, C. Marois, and J. Krist. Optical Images of an Exosolar Planet 25 Light-Years from Earth. *Science*, 322:1345, November 2008.
119. L. Kaltenegger. How to Characterize Habitable Worlds and Signs of Life. *ARA&A*, 55:433–485, August 2017.
120. L. Kaltenegger, F. Selsis, M. Fridlund, H. Lammer, C. Beichman, W. Danchi, C. Eiroa, T. Henning, T. Herbst, A. Léger, R. Liseau, J. Lunine, F. Paresce, A. Penny, A. Quirrenbach, H. Röttgering, J. Schneider, D. Stam, G. Tinetti, and G. J. White. Deciphering Spectral Fingerprints of Habitable Exoplanets. *Astrobiology*, 10:89–102, January 2010.
121. E. Karkoschka and M. G. Tomasko. The haze and methane distributions on Neptune from HST-STIS spectroscopy. *Icarus*, 211:780–797, January 2011.

122. T. Kataria, D. K. Sing, N. K. Lewis, C. Visscher, A. P. Showman, J. J. Fortney, and M. S. Marley. The Atmospheric Circulation of a Nine-hot-Jupiter Sample: Probing Circulation and Chemistry over a Wide Phase Space. *ApJ*, 821:9, April 2016.
123. B. M. Kilpatrick, P. E. Cubillos, K. B. Stevenson, N. K. Lewis, H. R. Wakeford, R. J. MacDonald, N. Madhusudhan, J. Blecic, G. Bruno, A. Burrows, D. Deming, K. Heng, M. R. Line, C. V. Morley, V. Parmentier, G. S. Tucker, J. A. Valenti, I. P. Waldmann, J. L. Bean, C. Beichman, J. Fraine, J. E. Krick, J. D. Lothringer, and A. M. Mandell. Community Targets of JWST’s Early Release Science Program: Evaluation of WASP-63b. *AJ*, 156:103, September 2018.
124. H. A. Knutson, B. Benneke, D. Deming, and D. Homeier. A featureless transmission spectrum for the Neptune-mass exoplanet GJ436b. *Nature*, 505:66–68, January 2014.
125. H. A. Knutson, D. Charbonneau, L. E. Allen, A. Burrows, and S. T. Megeath. The 3.6–8.0 μm Broadband Emission Spectrum of HD 209458b: Evidence for an Atmospheric Temperature Inversion. *ApJ*, 673:526–531, January 2008.
126. H. A. Knutson, D. Charbonneau, L. E. Allen, J. J. Fortney, E. Agol, N. B. Cowan, A. P. Showman, C. S. Cooper, and S. T. Megeath. A map of the day-night contrast of the extrasolar planet HD 189733b. *Nature*, 447:183–186, May 2007.
127. H. A. Knutson, D. Charbonneau, A. Burrows, F. T. O’Donovan, and G. Mandushev. Detection of A Temperature Inversion in the Broadband Infrared Emission Spectrum of TrES-4. *ApJ*, 691:866–874, January 2009.
128. T. D. Komacek, A. P. Showman, and X. Tan. Atmospheric Circulation of Hot Jupiters: Dayside-Nightside Temperature Differences. II. Comparison with Observations. *ApJ*, 835:198, February 2017.
129. Q. M. Konopacky, T. S. Barman, B. A. Macintosh, and C. Marois. Detection of Carbon Monoxide and Water Absorption Lines in an Exoplanet Atmosphere. *Science*, 339:1398–1401, March 2013.
130. R. k. Kopparapu, E. T. Wolf, G. Arney, N. E. Batalha, J. Haqq-Misra, S. L. Grimm, and K. Heng. Habitable Moist Atmospheres on Terrestrial Planets near the Inner Edge of the Habitable Zone around M Dwarfs. *ApJ*, 845:5, August 2017.
131. L. Kreidberg, J. L. Bean, J.-M. Désert, B. Benneke, D. Deming, K. B. Stevenson, S. Seager, Z. Berta-Thompson, A. Seifahrt, and D. Homeier. Clouds in the atmosphere of the super-Earth exoplanet GJ1214b. *Nature*, 505:69–72, January 2014.
132. L. Kreidberg, J. L. Bean, J.-M. Désert, M. R. Line, J. J. Fortney, N. Madhusudhan, K. B. Stevenson, A. P. Showman, D. Charbonneau, P. R. McCullough, S. Seager, A. Burrows, G. W. Henry, M. Williamson, T. Kataria, and D. Homeier. A Precise Water Abundance Measurement for the Hot Jupiter WASP-43b. *ApJ*, 793:L27, October 2014.
133. L. Kreidberg, M. R. Line, J. L. Bean, K. B. Stevenson, J.-M. Désert, N. Madhusudhan, J. J. Fortney, J. K. Barstow, G. W. Henry, M. H. Williamson, and A. P. Showman. A Detection of Water in the Transmission Spectrum of the Hot Jupiter WASP-12b and Implications for Its Atmospheric Composition. *ApJ*, 814:66, November 2015.
134. L. Kreidberg, M. R. Line, V. Parmentier, K. B. Stevenson, T. Louden, M. Bonnefoy, J. K. Faherty, G. W. Henry, M. H. Williamson, K. Stassun, T. G. Beatty, J. L. Bean, J. J. Fortney, A. P. Showman, J.-M. Désert, and J. Arcangeli. Global Climate and Atmospheric Composition of the Ultra-hot Jupiter WASP-103b from HST and Spitzer Phase Curve Observations. *AJ*, 156:17, July 2018.
135. L. Kreidberg. *Exoplanet Atmosphere Measurements from Transmission Spectroscopy and Other Planet Star Combined Light Observations*, page 100. 2018.
136. J. R. Kulow, K. France, J. Linsky, and R. O. P. Loyd. Ly α Transit Spectroscopy and the Neutral Hydrogen Tail of the Hot Neptune GJ 436b. *ApJ*, 786:132, May 2014.
137. R. L. Kurucz. Atomic and Molecular Data for Opacity Calculations. *Rev. Mex. Astron. Astrofis.*, 23, March 1992.

138. Planetary Habitability Laboratory. Hec: Data of potentially habitable worlds, 2018.
139. M. Lambrechts and A. Johansen. Rapid growth of gas-giant cores by pebble accretion. *A&A*, 544:A32, August 2012.
140. H. Lammer and M. Blanc. From Disks to Planets: The Making of Planets and Their Early Atmospheres. An Introduction. *Space Sci. Rev.*, 214:60, March 2018.
141. B. LAVIE. HELIOS-R: An Ultrafast, Open-Source Retrieval Code For Exoplanetary Atmosphere Characterization. In *AAS/Division for Extreme Solar Systems Abstracts*, volume 3 of *AAS/Division for Extreme Solar Systems Abstracts*, page 104.20, December 2015.
142. B. Lavie, D. Ehrenreich, V. Bourrier, A. Lecavelier des Etangs, A. Vidal-Madjar, X. Delfosse, A. Gracia Berna, K. Heng, N. Thomas, S. Udry, and P. J. Wheatley. The long egress of GJ 436b's giant exosphere. *A&A*, 605:L7, September 2017.
143. B. Lavie, J. M. Mendonça, C. Mordasini, M. Malik, M. Bonnefoy, B.-O. Demory, M. Oreshenko, S. L. Grimm, D. Ehrenreich, and K. Heng. HELIOS-RETRIEVAL: An Open-source, Nested Sampling Atmospheric Retrieval Code; Application to the HR 8799 Exoplanets and Inferred Constraints for Planet Formation. *AJ*, 154:91, September 2017.
144. J.-M. Lee, K. Heng, and P. G. J. Irwin. Atmospheric Retrieval Analysis of the Directly Imaged Exoplanet HR 8799b. *ApJ*, 778:97, December 2013.
145. N. K. Lewis, V. Parmentier, T. Kataria, J. de Wit, A. P. Showman, J. J. Fortney, and M. S. Marley. Atmospheric Circulation and Cloud Evolution on the Highly Eccentric Extrasolar Planet HD 80606b. *ArXiv e-prints*, June 2017.
146. N. K. Lewis, A. P. Showman, J. J. Fortney, M. S. Marley, R. S. Freedman, and K. Lodders. Atmospheric Circulation of Eccentric Hot Neptune GJ436b. *ApJ*, 720:344–356, September 2010.
147. G. Li, I. E. Gordon, L. S. Rothman, Y. Tan, S.-M. Hu, S. Kassi, A. Campargue, and E. S. Medvedev. Rovibrational Line Lists for Nine Isotopologues of the CO Molecule in the X $^1\Sigma^+$ Ground Electronic State. *ApJS*, 216:15, January 2015.
148. M. R. Line, H. Knutson, A. S. Wolf, and Y. L. Yung. A Systematic Retrieval Analysis of Secondary Eclipse Spectra. II. A Uniform Analysis of Nine Planets and their C to O Ratios. *ApJ*, 783:70, March 2014.
149. M. R. Line, M. S. Marley, M. C. Liu, B. Burningham, C. V. Morley, N. R. Hinkel, J. Teske, J. J. Fortney, R. Freedman, and R. Lupu. Uniform Atmospheric Retrieval Analysis of Ultracool Dwarfs. II. Properties of 11 T dwarfs. *ApJ*, 848:83, October 2017.
150. M. R. Line and V. Parmentier. The Influence of Nonuniform Cloud Cover on Transit Transmission Spectra. *ApJ*, 820:78, March 2016.
151. M. R. Line, K. B. Stevenson, J. Bean, J.-M. Desert, J. J. Fortney, L. Kreidberg, N. Madhusudhan, A. P. Showman, and H. Diamond-Lowe. No Thermal Inversion and a Solar Water Abundance for the Hot Jupiter HD 209458b from HST/WFC3 Spectroscopy. *AJ*, 152:203, December 2016.
152. M. R. Line, J. Teske, B. Burningham, J. Fortney, and M. Marley. Uniform Atmospheric Retrieval Analysis of Ultracool Dwarfs I: Characterizing Benchmarks, Gl570D and HD3651B. *ArXiv e-prints*, April 2015.
153. S. Lines, N. J. Mayne, I. A. Boutle, J. Manners, G. K. H. Lee, C. Helling, B. Drummond, D. S. Amundsen, J. Goyal, D. M. Acreman, P. Tremblin, and M. Kerslake. Simulating the cloudy atmospheres of HD 209458 b and HD 189733 b with the 3D Met Office Unified Model. *A&A*, 615:A97, July 2018.
154. J. D. Lothringer, T. Barman, and T. Koskinen. Extremely Irradiated Hot Jupiters: Non-Oxide Inversions, H- Opacity, and Thermal Dissociation of Molecules. *ArXiv e-prints*, April 2018.
155. T. Loudon and P. J. Wheatley. Spatially Resolved Eastward Winds and Rotation of HD 189733b. *ApJ*, 814:L24, December 2015.
156. The LUVOIR Team. The LUVOIR Mission Concept Study Interim Report. *arXiv e-prints*, September 2018.

157. R. J. MacDonald and N. Madhusudhan. HD 209458b in new light: evidence of nitrogen chemistry, patchy clouds and sub-solar water. *MNRAS*, 469:1979–1996, August 2017.
158. R. J. MacDonald and N. Madhusudhan. Signatures of Nitrogen Chemistry in Hot Jupiter Atmospheres. *ApJ*, 850:L15, November 2017.
159. B. Macintosh, J. R. Graham, T. Barman, R. J. De Rosa, Q. Konopacky, M. S. Marley, C. Marois, E. L. Nielsen, L. Pueyo, A. Rajan, J. Rameau, D. Saumon, J. J. Wang, J. Patience, M. Ammons, P. Arriaga, E. Artigau, S. Beckwith, J. Brewster, S. Bruzzone, J. Bulger, B. Burningham, A. S. Burrows, C. Chen, E. Chiang, J. K. Chilcote, R. I. Dawson, R. Dong, R. Doyon, Z. H. Draper, G. Duchêne, T. M. Esposito, D. Fabrycky, M. P. Fitzgerald, K. B. Follette, J. J. Fortney, B. Gerard, S. Goodsell, A. Z. Greenbaum, P. Higon, S. Hinkley, T. H. Cotten, L.-W. Hung, P. Ingraham, M. Johnson-Groh, P. Kalas, D. Lafreniere, J. E. Larkin, J. Lee, M. Line, D. Long, J. Maire, F. Marchis, B. C. Matthews, C. E. Max, S. Metchev, M. A. Millar-Blanchaer, T. Mittal, C. V. Morley, K. M. Morzinski, R. Murray-Clay, R. Oppenheimer, D. W. Palmer, R. Patel, M. D. Perrin, L. A. Poyneer, R. R. Rafikov, F. T. Rantakyro, E. L. Rice, P. Rojo, A. R. Rudy, J.-B. Ruffio, M. T. Ruiz, N. Sadakuni, L. Saddlemyer, M. Salama, D. Savransky, A. C. Schneider, A. Sivaramakrishnan, I. Song, R. Soummer, S. Thomas, G. Vasisht, J. K. Wallace, K. Ward-Duong, S. J. Wiktorowicz, S. G. Wolff, and B. Zuckerman. Discovery and spectroscopy of the young jovian planet 51 Eri b with the Gemini Planet Imager. *Science*, 350:64–67, October 2015.
160. B. Macintosh and Gemini Planet Imager Exoplanet Survey. The Gemini Planet Imager Exoplanet Survey and the discovery of the young Jupiter analog 51 Eridani b. In *American Astronomical Society Meeting Abstracts #227*, volume 227 of *American Astronomical Society Meeting Abstracts*, page 321.04, January 2016.
161. N. Madhusudhan. C/O Ratio as a Dimension for Characterizing Exoplanetary Atmospheres. *ApJ*, 758:36, October 2012.
162. N. Madhusudhan. Atmospheric Retrieval of Exoplanets. page 104, 2018.
163. N. Madhusudhan, M. Agúndez, J. I. Moses, and Y. Hu. Exoplanetary Atmospheres-Chemistry, Formation Conditions, and Habitability. *Space Sci. Rev.*, 205:285–348, December 2016.
164. N. Madhusudhan, M. A. Amin, and G. M. Kennedy. Toward Chemical Constraints on Hot Jupiter Migration. *ApJ*, 794:L12, October 2014.
165. N. Madhusudhan, B. Bitsch, A. Johansen, and L. Eriksson. Atmospheric signatures of giant exoplanet formation by pebble accretion. *MNRAS*, 469:4102–4115, August 2017.
166. N. Madhusudhan, N. Crouzet, P. R. McCullough, D. Deming, and C. Hedges. H₂O Abundances in the Atmospheres of Three Hot Jupiters. *ApJ*, 791:L9, August 2014.
167. N. Madhusudhan, H. Knutson, J. J. Fortney, and T. Barman. Exoplanetary Atmospheres. *Protostars and Planets VI*, pages 739–762, 2014.
168. N. Madhusudhan and S. Seager. A Temperature and Abundance Retrieval Method for Exoplanet Atmospheres. *ApJ*, 707:24–39, December 2009.
169. N. Madhusudhan and S. Seager. High Metallicity and Non-equilibrium Chemistry in the Dayside Atmosphere of hot-Neptune GJ 436b. *ApJ*, 729:41, March 2011.
170. M. Malik, L. Grosheintz, J. M. Mendonça, S. L. Grimm, B. Lavie, D. Kitzmann, S.-M. Tsai, A. Burrows, L. Kreidberg, M. Bedell, J. L. Bean, K. B. Stevenson, and K. Heng. HELIOS: An Open-source, GPU-accelerated Radiative Transfer Code for Self-consistent Exoplanetary Atmospheres. *AJ*, 153:56, February 2017.
171. A. M. Mandell, K. Haynes, E. Sinukoff, N. Madhusudhan, A. Burrows, and D. Deming. Exoplanet Transit Spectroscopy Using WFC3: WASP-12 b, WASP-17 b, and WASP-19 b. *ApJ*, 779:128, December 2013.
172. M. S. Marley, A. S. Ackerman, J. N. Cuzzi, and D. Kitzmann. *Clouds and Hazes in Exoplanet Atmospheres*, pages 367–391. 2013.
173. M. S. Marley and T. D. Robinson. On the Cool Side: Modeling the Atmospheres of Brown Dwarfs and Giant Planets. *ARA&A*, 53:279–323, August 2015.

174. C. Marois, B. Macintosh, T. Barman, B. Zuckerman, I. Song, J. Patience, D. Lafrenière, and R. Doyon. Direct Imaging of Multiple Planets Orbiting the Star HR 8799. *Science*, 322:1348, November 2008.
175. J. H. C. Martins, N. C. Santos, P. Figueira, J. P. Faria, M. Montalto, I. Boisse, D. Ehrenreich, C. Lovis, M. Mayor, C. Melo, F. Pepe, S. G. Sousa, S. Udry, and D. Cunha. Evidence for a spectroscopic direct detection of reflected light from 51 Pegasi b. *A&A*, 576:A134, April 2015.
176. R. Mbarek and E. M.-R. Kempton. Clouds in Super-Earth Atmospheres: Chemical Equilibrium Calculations. *ApJ*, 827:121, August 2016.
177. P. McCullough and J. MacKenty. Considerations for using Spatial Scans with WFC3. Technical report, May 2012.
178. P. R. McCullough, N. Crouzet, D. Deming, and N. Madhusudhan. Water Vapor in the Spectrum of the Extrasolar Planet HD 189733b. I. The Transit. *ApJ*, 791:55, August 2014.
179. V. S. Meadows, C. T. Reinhard, G. N. Arney, M. N. Parenteau, E. W. Schwieterman, S. D. Domagal-Goldman, A. P. Lincowski, K. R. Stapelfeldt, H. Rauer, S. DasSarma, S. Hegde, N. Narita, R. Deitrick, J. Lustig-Yaeger, T. W. Lyons, N. Siegler, and J. L. Grenfell. Exoplanet Biosignatures: Understanding Oxygen as a Biosignature in the Context of Its Environment. *Astrobiology*, 18:630–662, June 2018.
180. J. M. Mendonça, S. L. Grimm, L. Grosheintz, and K. Heng. THOR: A New and Flexible Global Circulation Model to Explore Planetary Atmospheres. *ApJ*, 829:115, October 2016.
181. B. Mennesson, S. Gaudi, S. Seager, K. Cahoy, S. Domagal-Goldman, L. Feinberg, O. Guyon, J. Kasdin, C. Marois, D. Mawet, M. Tamura, D. Mouillet, T. Prusti, A. Quirrenbach, T. Robinson, L. Rogers, P. Scowen, R. Somerville, K. Stapelfeldt, D. Stern, M. Still, M. Turnbull, J. Booth, A. Kiessling, G. Kuan, and K. Warfield. The Habitable Exoplanet (HabEx) Imaging Mission: preliminary science drivers and technical requirements. In *Space Telescopes and Instrumentation 2016: Optical, Infrared, and Millimeter Wave*, volume 9904 of *Proc. SPIE*, page 99040L, July 2016.
182. P. Mollière, R. van Boekel, C. Dullemond, T. Henning, and C. Mordasini. Model Atmospheres of Irradiated Exoplanets: The Influence of Stellar Parameters, Metallicity, and the C/O Ratio. *ApJ*, 813:47, November 2015.
183. P. Mollière, R. van Boekel, J. Bouwman, T. Henning, P.-O. Lagage, and M. Min. Observing transiting planets with JWST. Prime targets and their synthetic spectral observations. *A&A*, 600:A10, April 2017.
184. C. Mordasini, R. van Boekel, P. Mollière, T. Henning, and B. Benneke. The Imprint of Exoplanet Formation History on Observable Present-day Spectra of Hot Jupiters. *ApJ*, 832:41, November 2016.
185. C. V. Morley, L. Kreidberg, Z. Rustamkulov, T. Robinson, and J. J. Fortney. Observing the Atmospheres of Known Temperate Earth-sized Planets with JWST. *ApJ*, 850:121, December 2017.
186. J. I. Moses. Chemical kinetics on extrasolar planets. *Philosophical Transactions of the Royal Society of London Series A*, 372:20130073–20130073, March 2014.
187. J. I. Moses, M. R. Line, C. Visscher, M. R. Richardson, N. Nettelmann, J. J. Fortney, T. S. Barman, K. B. Stevenson, and N. Madhusudhan. Compositional Diversity in the Atmospheres of Hot Neptunes, with Application to GJ 436b. *ApJ*, 777:34, November 2013.
188. J. I. Moses, N. Madhusudhan, C. Visscher, and R. S. Freedman. Chemical Consequences of the C/O Ratio on Hot Jupiters: Examples from WASP-12b, CoRoT-2b, XO-1b, and HD 189733b. *ApJ*, 763:25, January 2013.
189. J. I. Moses, C. Visscher, J. J. Fortney, A. P. Showman, N. K. Lewis, C. A. Griffith, S. J. Klippenstein, M. Shabram, A. J. Friedson, M. S. Marley, and R. S. Freedman. Disequilibrium Carbon, Oxygen, and Nitrogen Chemistry in the Atmospheres of HD 189733b and HD 209458b. *ApJ*, 737:15, August 2011.
190. O. Mousis, J. I. Lunine, J.-M. Petit, K. Zahnle, L. Biennier, S. Picaud, T. V. Johnson, J. B. A.

- Mitchell, V. Boudon, D. Cordier, M. Devel, R. Georges, C. Griffith, N. Iro, M. S. Marley, and U. Marboeuf. On the Volatile Enrichments and Heavy Element Content in HD189733b. *ApJ*, 727:77, February 2011.
191. O. Mousis, U. Marboeuf, J. I. Lunine, Y. Alibert, L. N. Fletcher, G. S. Orton, F. Pauzat, and Y. Ellinger. Determination of the Minimum Masses of Heavy Elements in the Envelopes of Jupiter and Saturn. *ApJ*, 696:1348–1354, May 2009.
 192. N. Nikolov, D. K. Sing, A. S. Burrows, J. J. Fortney, G. W. Henry, F. Pont, G. E. Ballester, S. Aigrain, P. A. Wilson, C. M. Huitson, N. P. Gibson, J.-M. Désert, A. L. d. Etangs, A. P. Showman, A. Vidal-Madjar, H. R. Wakeford, and K. Zahnle. HST hot-Jupiter transmission spectral survey: haze in the atmosphere of WASP-6b. *MNRAS*, 447:463–478, February 2015.
 193. N. Nikolov, D. K. Sing, J. J. Fortney, J. M. Goyal, B. Drummond, T. M. Evans, N. P. Gibson, E. J. W. De Mooij, Z. Rustamkulov, H. R. Wakeford, B. Smalley, A. J. Burgasser, C. Hellier, C. Helling, N. J. Mayne, N. Madhusudhan, T. Kataria, J. Baines, A. L. Carter, G. E. Ballester, J. K. Barstow, J. McCleery, and J. J. Spake. An absolute sodium abundance for a cloud-free ‘hot Saturn’ exoplanet. *Nature*, 557:526–529, May 2018.
 194. N. Nikolov, D. K. Sing, N. P. Gibson, J. J. Fortney, T. M. Evans, J. K. Barstow, T. Kataria, and P. A. Wilson. VLT FORS2 Comparative Transmission Spectroscopy: Detection of Na in the Atmosphere of WASP-39b from the Ground. *ApJ*, 832:191, December 2016.
 195. N. Nikolov, D. K. Sing, F. Pont, A. S. Burrows, J. J. Fortney, G. E. Ballester, T. M. Evans, C. M. Huitson, H. R. Wakeford, P. A. Wilson, S. Aigrain, D. Deming, N. P. Gibson, G. W. Henry, H. Knutson, A. Lecavelier des Etangs, A. P. Showman, A. Vidal-Madjar, and K. Zahnle. Hubble Space Telescope hot Jupiter transmission spectral survey: a detection of Na and strong optical absorption in HAT-P-1b. *MNRAS*, 437:46–66, January 2014.
 196. S. K. Nugroho, H. Kawahara, K. Masuda, T. Hirano, T. Kotani, and A. Tajitsu. High-resolution Spectroscopic Detection of TiO and a Stratosphere in the Day-side of WASP-33b. *AJ*, 154:221, December 2017.
 197. K. I. Öberg, R. Murray-Clay, and E. A. Bergin. The Effects of Snowlines on C/O in Planetary Atmospheres. *ApJ*, 743:L16, December 2011.
 198. M. Oshagh, N. C. Santos, D. Ehrenreich, N. Haghighipour, P. Figueira, A. Santerne, and M. Montalto. Impact of occultations of stellar active regions on transmission spectra. Can occultation of a plage mimic the signature of a blue sky? *A&A*, 568:A99, August 2014.
 199. J. E. Owen. Atmospheric Escape and the Evolution of Close-in Exoplanets. *arXiv e-prints*, July 2018.
 200. V. Parmentier, J. J. Fortney, A. P. Showman, C. Morley, and M. S. Marley. Transitions in the Cloud Composition of Hot Jupiters. *ApJ*, 828:22, September 2016.
 201. V. Parmentier, M. R. Line, J. L. Bean, M. Mansfield, L. Kreidberg, R. Lupu, C. Visscher, J.-M. Desert, J. J. Fortney, M. Deleuil, J. Arcangeli, A. P. Showman, and M. S. Marley. From thermal dissociation to condensation in the atmospheres of ultra hot Jupiters: WASP-121b in context. *ArXiv e-prints*, April 2018.
 202. V. Parmentier, A. P. Showman, and Y. Lian. 3D mixing in hot Jupiters atmospheres. I. Application to the day/night cold trap in HD 209458b. *A&A*, 558:A91, October 2013.
 203. Andrei T. Patrascu, Sergei N. Yurchenko, and Jonathan Tennyson. ExoMol molecular line lists - IX. The spectrum of AlO. *MNRAS*, 449:3613–3619, Jun 2015.
 204. D. J. M. Petit dit de la Roche, H. J. Hoeijmakers, and I. A. G. Snellen. Molecule mapping of HR8799b using OSIRIS on Keck. Strong detection of water and carbon monoxide, but no methane. *A&A*, 616:A146, August 2018.
 205. A. Pinhas and N. Madhusudhan. On signatures of clouds in exoplanetary transit spectra. *MNRAS*, 471:4355–4373, November 2017.
 206. A. Pinhas, N. Madhusudhan, S. Gandhi, and R. MacDonald. H₂O abundances and cloud properties in ten hot giant exoplanets. *MNRAS*, 482:1485–1498, January 2019.
 207. Ana-Maria A. Piso, Karin I. Öberg, Tilman Birnstiel, and Ruth A. Murray-Clay. C/O and

- Snowline Locations in Protoplanetary Disks: The Effect of Radial Drift and Viscous Gas Accretion. *ApJ*, 815:109, December 2015.
208. Ana-Maria A. Piso, Jamila Pegues, and Karin I. Öberg. The Role of Ice Compositions for Snowlines and the C/N/O Ratios in Active Disks. *ApJ*, 833:203, December 2016.
 209. F. Pont, D. K. Sing, N. P. Gibson, S. Aigrain, G. Henry, and N. Husnoo. The prevalence of dust on the exoplanet HD 189733b from Hubble and Spitzer observations. *MNRAS*, 432:2917–2944, July 2013.
 210. R. E. Pudritz, A. J. Cridland, and M. Alessi. Connecting Planetary Composition with Formation. *ArXiv e-prints*, April 2018.
 211. B. V. Rackham, D. Apai, and M. S. Giampapa. The Transit Light Source Effect: False Spectral Features and Incorrect Densities for M-dwarf Transiting Planets. *ApJ*, 853:122, February 2018.
 212. E. Rauscher. Models of Warm Jupiter Atmospheres: Observable Signatures of Obliquity. *ApJ*, 846:69, September 2017.
 213. E. Rauscher and K. Menou. Three-dimensional Modeling of Hot Jupiter Atmospheric Flows. *ApJ*, 714:1334–1342, May 2010.
 214. S. Redfield, M. Endl, W. D. Cochran, and L. Koesterke. Sodium Absorption from the Exoplanetary Atmosphere of HD 189733b Detected in the Optical Transmission Spectrum. *ApJ*, 673:L87–L90, January 2008.
 215. C. Richard, I.E. Gordon, L.S. Rothman, M. Abel, L. Frommhold, M. Gustafsson, J.-M. Hartmann, C. Hermans, W.J. Lafferty, G.S. Orton, K.M. Smith, and H. Tran. New section of the hitran database: Collision-induced absorption (cia). *Journal of Quantitative Spectroscopy and Radiative Transfer*, 113(11):1276 – 1285, 2012. Three Leaders in Spectroscopy.
 216. P. B. Rimmer, J. Xu, S. J. Thompson, E. Gillen, J. D. Sutherland, and D. Queloz. Prebiotic Chemistry on Exoplanets Within the Liquid Water Habitable Zone. In *Habitable Worlds 2017: A System Science Workshop*, volume 2042 of *LPI Contributions*, page 4094, November 2017.
 217. P. B. Rimmer, J. Xu, S. J. Thompson, E. Gillen, J. D. Sutherland, and D. Queloz. The origin of RNA precursors on exoplanets. *Science Advances*, 4:eaar3302, August 2018.
 218. M. Rocchetto, I. P. Waldmann, O. Venot, P.-O. Lagage, and G. Tinetti. Exploring Biases of Atmospheric Retrievals in Simulated JWST Transmission Spectra of Hot Jupiters. *ApJ*, 833:120, December 2016.
 219. F. Rodler, M. Kürster, and J. R. Barnes. Detection of CO absorption in the atmosphere of the hot Jupiter HD 189733b. *MNRAS*, 432:1980–1988, July 2013.
 220. F. Rodler and M. López-Morales. Feasibility Studies for the Detection of O₂ in an Earth-like Exoplanet. *ApJ*, 781:54, January 2014.
 221. L. S. Rothman, I. E. Gordon, R. J. Barber, H. Dothe, R. R. Gamache, A. Goldman, V. I. Perevalov, S. A. Tashkun, and J. Tennyson. HITEMP, the high-temperature molecular spectroscopic database. *J. Quant. Spec. Radiat. Transf.*, 111:2139–2150, October 2010.
 222. M. Samland, P. Mollière, M. Bonnefoy, A.-L. Maire, F. Cantalloube, A. C. Cheetham, D. Mesa, R. Gratton, B. A. Biller, Z. Wahhaj, J. Bouwman, W. Brandner, D. Melnick, J. Carson, M. Janson, T. Henning, D. Homeier, C. Mordasini, M. Langlois, S. P. Quanz, R. van Boekel, A. Zurlo, J. E. Schlieder, H. Avenhaus, J.-L. Beuzit, A. Boccaletti, M. Bonavita, G. Chauvin, R. Claudi, M. Cudel, S. Desidera, M. Feldt, T. Fusco, R. Galicher, T. G. Kopytova, A.-M. Lagrange, H. Le Coroller, P. Martinez, O. Moeller-Nilsson, D. Mouillet, L. M. Mugnier, C. Perrot, A. Sevin, E. Sissa, A. Vigan, and L. Weber. Spectral and atmospheric characterization of 51 Eridani b using VLT/SPHERE. *A&A*, 603:A57, July 2017.
 223. E. Schlawin, E. Agol, L. M. Walkowicz, K. Covey, and J. P. Lloyd. Exoplanetary Transits of Limb-brightened Lines: Tentative Si IV Absorption by HD 209458b. *ApJ*, 722:L75–L79, October 2010.
 224. J. C. Schwartz, Z. Kashner, D. Jovmir, and N. B. Cowan. Phase Offsets and the Energy Budgets of Hot Jupiters. *ApJ*, 850:154, December 2017.
 225. David W. Schwenke. Opacity of tio from a coupled electronic state calculation parametrized

- by abinitio and experimental data. *Faraday Discuss.*, 109:321–334, 1998.
226. E. W. Schwieterman, N. Y. Kiang, M. N. Parenteau, C. E. Harman, S. DasSarma, T. M. Fisher, G. N. Arney, H. E. Hartnett, C. T. Reinhard, S. L. Olson, V. S. Meadows, C. S. Cockell, S. I. Walker, J. L. Grenfell, S. Hegde, S. Rugheimer, R. Hu, and T. W. Lyons. Exoplanet Biosignatures: A Review of Remotely Detectable Signs of Life. *Astrobiology*, 18:663–708, June 2018.
 227. S. Seager. *Exoplanets*. December 2010.
 228. S. Seager. The search for habitable planets with biosignature gases framed by a ‘Biosignature Drake Equation’. *International Journal of Astrobiology*, 17:294–302, October 2018.
 229. S. Seager, W. Bains, and R. Hu. Biosignature Gases in H₂-dominated Atmospheres on Rocky Exoplanets. *ApJ*, 777:95, November 2013.
 230. S. Seager, W. Bains, and J. J. Petkowski. Toward a List of Molecules as Potential Biosignature Gases for the Search for Life on Exoplanets and Applications to Terrestrial Biochemistry. *Astrobiology*, 16:465–485, June 2016.
 231. S. Seager and D. D. Sasselov. Extrasolar Giant Planets under Strong Stellar Irradiation. *ApJ*, 502:L157–L161, August 1998.
 232. E. Sedaghati, H. M. J. Boffin, R. J. MacDonald, S. Gandhi, N. Madhusudhan, N. P. Gibson, M. Oshagh, A. Claret, and H. Rauer. Detection of titanium oxide in the atmosphere of a hot Jupiter. *Nature*, 549:238–241, September 2017.
 233. S. Seager and D. D. Sasselov. Theoretical Transmission Spectra during Extrasolar Giant Planet Transits. *ApJ*, 537:916–921, July 2000.
 234. A. Segura, L. M. Walkowicz, V. Meadows, J. Kasting, and S. Hawley. The Effect of a Strong Stellar Flare on the Atmospheric Chemistry of an Earth-like Planet Orbiting an M Dwarf. *Astrobiology*, 10:751–771, September 2010.
 235. F. Selsis, L. Kaltenegger, and J. Paillet. Terrestrial exoplanets: diversity, habitability and characterization. *Physica Scripta Volume T*, 130(1):014032, August 2008.
 236. K. B. Sheppard, A. M. Mandell, P. Tamburo, S. Gandhi, A. Pinhas, N. Madhusudhan, and D. Deming. Evidence for a Dayside Thermal Inversion and High Metallicity for the Hot Jupiter WASP-18b. *ApJ*, 850:L32, December 2017.
 237. A. P. Showman, C. S. Cooper, J. J. Fortney, and M. S. Marley. Atmospheric Circulation of Hot Jupiters: Three-dimensional Circulation Models of HD 209458b and HD 189733b with Simplified Forcing. *ApJ*, 682:559–576, July 2008.
 238. A. P. Showman, J. J. Fortney, N. K. Lewis, and M. Shabram. Doppler Signatures of the Atmospheric Circulation on Hot Jupiters. *ApJ*, 762:24, January 2013.
 239. A. P. Showman, J. J. Fortney, Y. Lian, M. S. Marley, R. S. Freedman, H. A. Knutson, and D. Charbonneau. Atmospheric Circulation of Hot Jupiters: Coupled Radiative-Dynamical General Circulation Model Simulations of HD 189733b and HD 209458b. *ApJ*, 699:564–584, July 2009.
 240. A. P. Showman and T. Guillot. Atmospheric circulation and tides of “51 Pegasus b-like” planets. *A&A*, 385:166–180, April 2002.
 241. A. P. Showman and L. M. Polvani. Equatorial Superrotation on Tidally Locked Exoplanets. *ApJ*, 738:71, September 2011.
 242. A. Shporer and R. Hu. Studying Atmosphere-dominated Hot Jupiter Kepler Phase Curves: Evidence that Inhomogeneous Atmospheric Reflection Is Common. *AJ*, 150:112, October 2015.
 243. D. K. Sing, J.-M. Désert, J. J. Fortney, A. Lecavelier Des Etangs, G. E. Ballester, J. Cepa, D. Ehrenreich, M. López-Morales, F. Pont, M. Shabram, and A. Vidal-Madjar. Gran Telescopio Canarias OSIRIS transiting exoplanet atmospheric survey: detection of potassium in XO-2b from narrowband spectrophotometry. *A&A*, 527:A73, March 2011.
 244. D. K. Sing, J. J. Fortney, N. Nikolov, H. R. Wakeford, T. Kataria, T. M. Evans, S. Aigrain, G. E. Ballester, A. S. Burrows, D. Deming, J.-M. Désert, N. P. Gibson, G. W. Henry, C. M. Huitson, H. A. Knutson, A. Lecavelier Des Etangs, F. Pont, A. P. Showman, A. Vidal-Madjar,

- M. H. Williamson, and P. A. Wilson. A continuum from clear to cloudy hot-Jupiter exoplanets without primordial water depletion. *Nature*, 529:59–62, January 2016.
245. D. K. Sing, C. M. Huitson, M. Lopez-Morales, F. Pont, J.-M. Désert, D. Ehrenreich, P. A. Wilson, G. E. Ballester, J. J. Fortney, A. Lecavelier des Etangs, and A. Vidal-Madjar. GTC OSIRIS transiting exoplanet atmospheric survey: detection of sodium in XO-2b from differential long-slit spectroscopy. *MNRAS*, 426:1663–1670, October 2012.
 246. D. K. Sing and M. López-Morales. Ground-based secondary eclipse detection of the very-hot Jupiter OGLE-TR-56b. *A&A*, 493:L31–L34, January 2009.
 247. D. K. Sing, H. R. Wakeford, A. P. Showman, N. Nikolov, J. J. Fortney, A. S. Burrows, G. E. Ballester, D. Deming, S. Aigrain, J.-M. Désert, N. P. Gibson, G. W. Henry, H. Knutson, A. Lecavelier des Etangs, F. Pont, A. Vidal-Madjar, M. W. Williamson, and P. A. Wilson. HST hot-Jupiter transmission spectral survey: detection of potassium in WASP-31b along with a cloud deck and Rayleigh scattering. *MNRAS*, 446:2428–2443, January 2015.
 248. I. Snellen, R. de Kok, J. L. Birkby, B. Brandl, M. Brogi, C. Keller, M. Kenworthy, H. Schwarz, and R. Stuik. Combining high-dispersion spectroscopy with high contrast imaging: Probing rocky planets around our nearest neighbors. *A&A*, 576:A59, April 2015.
 249. I. A. G. Snellen, S. Albrecht, E. J. W. de Mooij, and R. S. Le Poole. Ground-based detection of sodium in the transmission spectrum of exoplanet HD 209458b. *A&A*, 487:357–362, August 2008.
 250. I. A. G. Snellen, B. R. Brandl, R. J. de Kok, M. Brogi, J. Birkby, and H. Schwarz. Fast spin of the young extrasolar planet β Pictoris b. *Nature*, 509:63–65, May 2014.
 251. I. A. G. Snellen, R. J. de Kok, E. J. W. de Mooij, and S. Albrecht. The orbital motion, absolute mass and high-altitude winds of exoplanet HD209458b. *Nature*, 465:1049–1051, June 2010.
 252. I. A. G. Snellen, J.-M. Désert, L. B. F. M. Waters, T. Robinson, V. Meadows, E. F. van Dishoeck, B. R. Brandl, T. Henning, J. Bouwman, F. Lahuis, M. Min, C. Lovis, C. Dominik, V. Van Eylen, D. Sing, G. Anglada-Escudé, J. L. Birkby, and M. Brogi. Detecting Proxima b’s Atmosphere with JWST Targeting CO₂ at 15 μ m Using a High-pass Spectral Filtering Technique. *AJ*, 154:77, August 2017.
 253. J. J. Spake, D. K. Sing, T. M. Evans, A. Oklopčić, V. Bourrier, L. Kreidberg, B. V. Rackham, J. Irwin, D. Ehrenreich, A. Wyttenbach, H. R. Wakeford, Y. Zhou, K. L. Chubb, N. Nikolov, J. M. Goyal, G. W. Henry, M. H. Williamson, S. Blumenthal, D. R. Anderson, C. Hellier, D. Charbonneau, S. Udry, and N. Madhusudhan. Helium in the eroding atmosphere of an exoplanet. *Nature*, 557:68–70, May 2018.
 254. L. A. Sromovsky, P. M. Fry, and J. H. Kim. Methane on Uranus: The case for a compact CH₄ cloud layer at low latitudes and a severe CH₄ depletion at high-latitudes based on re-analysis of Voyager occultation measurements and STIS spectroscopy. *Icarus*, 215:292–312, September 2011.
 255. K. B. Stevenson. Quantifying and Predicting the Presence of Clouds in Exoplanet Atmospheres. *ApJ*, 817:L16, February 2016.
 256. K. B. Stevenson, J.-M. Désert, M. R. Line, J. L. Bean, J. J. Fortney, A. P. Showman, T. Kataria, L. Kreidberg, P. R. McCullough, G. W. Henry, D. Charbonneau, A. Burrows, S. Seager, N. Madhusudhan, M. H. Williamson, and D. Homeier. Thermal structure of an exoplanet atmosphere from phase-resolved emission spectroscopy. *Science*, 346:838–841, November 2014.
 257. D. Sudarsky, A. Burrows, and I. Hubeny. Theoretical Spectra and Atmospheres of Extrasolar Giant Planets. *ApJ*, 588:1121–1148, May 2003.
 258. M. R. Swain, G. Vasisht, and G. Tinetti. The presence of methane in the atmosphere of an extrasolar planet. *Nature*, 452:329–331, March 2008.
 259. X. Tan and A. P. Showman. Effects of Latent Heating on Atmospheres of Brown Dwarfs and Directly Imaged Planets. *ApJ*, 835:186, February 2017.

260. J. Tennyson and S. Yurchenko. The ExoMol Atlas of Molecular Opacities. *Atoms*, 6:26, May 2018.
261. G. Tinetti, A. Vidal-Madjar, M.-C. Liang, J.-P. Beaulieu, Y. Yung, S. Carey, R. J. Barber, J. Tennyson, I. Ribas, N. Allard, G. E. Ballester, D. K. Sing, and F. Selsis. Water vapour in the atmosphere of a transiting extrasolar planet. *Nature*, 448:169–171, July 2007.
262. K. O. Todorov, M. R. Line, J. E. Pineda, M. R. Meyer, S. P. Quanz, S. Hinkley, and J. J. Fortney. The Water Abundance of the Directly Imaged Substellar Companion κ And b Retrieved from a Near Infrared Spectrum. *ApJ*, 823:14, May 2016.
263. S.-M. Tsai, J. R. Lyons, L. Grosheintz, P. B. Rimmer, D. Kitzmann, and K. Heng. VULCAN: An Open-source, Validated Chemical Kinetics Python Code for Exoplanetary Atmospheres. *ApJS*, 228:20, February 2017.
264. A. Tsiaras, I. P. Waldmann, M. Rocchetto, R. Varley, G. Morello, M. Damiano, and G. Tinetti. A New Approach to Analyzing HST Spatial Scans: The Transmission Spectrum of HD 209458 b. *ApJ*, 832:202, December 2016.
265. A. Tsiaras, M. Rocchetto, I. P. Waldmann, O. Venot, R. Varley, G. Morello, M. Damiano, G. Tinetti, E. J. Barton, S. N. Yurchenko, and J. Tennyson. Detection of an atmosphere around the super-Earth 55 Cancri e. *ApJ*, 820(2):99, mar 2016.
266. A. Tsiaras, I. P. Waldmann, T. Zingales, M. Rocchetto, G. Morello, M. Damiano, K. Karpouzas, G. Tinetti, L. K. McKemmish, J. Tennyson, and S. N. Yurchenko. A Population Study of Gaseous Exoplanets. *AJ*, 155:156, April 2018.
267. O. Venot, E. Hébrard, R. Bounaceur, and L. Decin. A new chemical scheme to study exoplanets atmospheres. *European Planetary Science Congress*, 9:EPSC2014–341, April 2014.
268. O. Venot, E. Hébrard, M. Agúndez, L. Decin, and R. Bounaceur. New chemical scheme for studying carbon-rich exoplanet atmospheres. *A&A*, 577:A33, May 2015.
269. J. Venturini, Y. Alibert, and W. Benz. Planet formation with envelope enrichment: new insights on planetary diversity. *A&A*, 596:A90, December 2016.
270. A. Vidal-Madjar, J.-M. Désert, A. Lecavelier des Etangs, G. Hébrard, G. E. Ballester, D. Ehrenreich, R. Ferlet, J. C. McConnell, M. Mayor, and C. D. Parkinson. Detection of Oxygen and Carbon in the Hydrodynamically Escaping Atmosphere of the Extrasolar Planet HD 209458b. *ApJ*, 604:L69–L72, March 2004.
271. A. Vidal-Madjar, C. M. Huitson, V. Bourrier, J.-M. Désert, G. Ballester, A. Lecavelier des Etangs, D. K. Sing, D. Ehrenreich, R. Ferlet, G. Hébrard, and J. C. McConnell. Magnesium in the atmosphere of the planet HD 209458 b: observations of the thermosphere-exosphere transition region. *A&A*, 560:A54, December 2013.
272. A. Vidal-Madjar, A. Lecavelier des Etangs, J.-M. Désert, G. E. Ballester, R. Ferlet, G. Hébrard, and M. Mayor. An extended upper atmosphere around the extrasolar planet HD209458b. *Nature*, 422:143–146, March 2003.
273. C. von Essen, M. Mallonn, L. Welbanks, N. Madhusudhan, A. Pinhas, H. Bouy, and P. Weis Hansen. An optical transmission spectrum of the ultra-hot Jupiter WASP-33 b. First indication of aluminum oxide in an exoplanet. *A&A*, 622:A71, February 2019.
274. H. R. Wakeford and D. K. Sing. Transmission spectral properties of clouds for hot Jupiter exoplanets. *A&A*, 573:A122, January 2015.
275. H. R. Wakeford, D. K. Sing, D. Deming, N. P. Gibson, J. J. Fortney, A. S. Burrows, G. Ballester, N. Nikolov, S. Aigrain, G. Henry, H. Knutson, A. Lecavelier des Etangs, F. Pont, A. P. Showman, A. Vidal-Madjar, and K. Zahnle. HST hot Jupiter transmission spectral survey: detection of water in HAT-P-1b from WFC3 near-IR spatial scan observations. *MNRAS*, 435:3481–3493, November 2013.
276. H. R. Wakeford, D. K. Sing, D. Deming, N. K. Lewis, J. Goyal, T. J. Wilson, J. Barstow, T. Kataria, B. Drummond, T. M. Evans, A. L. Carter, N. Nikolov, H. A. Knutson, G. E. Ballester, and A. M. Mandell. The Complete Transmission Spectrum of WASP-39b with a Precise Water Constraint. *AJ*, 155:29, January 2018.

277. H. R. Wakeford, D. K. Sing, T. Kataria, D. Deming, N. Nikolov, E. D. Lopez, P. Tremblin, D. S. Amundsen, N. K. Lewis, A. M. Mandell, J. J. Fortney, H. Knutson, B. Benneke, and T. M. Evans. HAT-P-26b: A Neptune-mass exoplanet with a well-constrained heavy element abundance. *Science*, 356:628–631, May 2017.
278. I. P. Waldmann, M. Rocchetto, G. Tinetti, E. J. Barton, S. N. Yurchenko, and J. Tennyson. Tau-REx II: Retrieval of Emission Spectra. *ApJ*, 813:13, November 2015.
279. I. P. Waldmann. Dreaming of Atmospheres. *ApJ*, 820:107, April 2016.
280. J. Wang, D. Mawet, R. Hu, G. Ruane, J.-R. Delorme, and N. Klimovic. Baseline Requirements For Detecting Biosignatures with the HabEx and LUVOIR Mission Concepts. *ArXiv e-prints*, June 2018.
281. M. H. Wong, P. R. Mahaffy, S. K. Atreya, H. B. Niemann, and T. C. Owen. Updated Galileo probe mass spectrometer measurements of carbon, oxygen, nitrogen, and sulfur on Jupiter. *Icarus*, 171:153–170, September 2004.
282. A. Wyttenbach, D. Ehrenreich, C. Lovis, S. Udry, and F. Pepe. Spectrally resolved detection of sodium in the atmosphere of HD 189733b with the HARPS spectrograph. *A&A*, 577:A62, May 2015.
283. S. N. Yurchenko, R. J. Barber, and J. Tennyson. A variationally computed line list for hot NH_3 . *MNRAS*, 413:1828–1834, May 2011.
284. S. N. Yurchenko, J. Tennyson, R. J. Barber, and W. Thiel. Vibrational transition moments of CH_4 from first principles. *Journal of Molecular Spectroscopy*, 291:69–76, September 2013.
285. S. N. Yurchenko and J. Tennyson. ExoMol line lists - IV. The rotation-vibration spectrum of methane up to 1500 K. *MNRAS*, 440:1649–1661, May 2014.
286. M. Zhang, H. A. Knutson, T. Kataria, J. C. Schwartz, N. B. Cowan, A. P. Showman, A. Burrows, J. J. Fortney, K. Todorov, J.-M. Desert, E. Agol, and D. Deming. Phase Curves of WASP-33b and HD 149026b and a New Correlation between Phase Curve Offset and Irradiation Temperature. *AJ*, 155:83, February 2018.
287. X. Zhang and A. P. Showman. Effects of Bulk Composition on the Atmospheric Dynamics on Close-in Exoplanets. *ApJ*, 836:73, February 2017.